POLITECNICO
MILANO 1863

SCUOLA DI INGEGNERIA INDUSTRIALE
E DELL'INFORMAZIONE

Onboard autonomous conjunction analysis with optical sensor

Tesi di Laurea Magistrale in
Space Engineering - Ingegneria Spaziale

Author: **Luca Capocchiano**

Student ID: 976231
Advisor: Prof. Pierluigi Di Lizia
Co-advisors: Prof. Mauro Massari, Michele Maestrini
Academic Year: 2021-22

Abstract

In recent years, the growing number of satellite launches increased the risk of in-orbit collision. Mitigation approaches, as Collision Avoidance Manoeuvre, require accurate prediction of the conjunction event to avoid the occurrence of catastrophic fragmentations such as the Iridium-33/Cosmos-2251 event, where no action was taken due to outdated information. The possibility to perform these operations directly onboard would allow a substantial reduction of the burden on ground infrastructure, improving the sustainability of the space environment.

In this thesis, a Low Earth Orbit satellite, based on the real COSMO-SkyMed 4, is equipped with an optical sensor and a statistical analysis is carried out to evaluate the camera performance in terms of visibility, with respect to a catalogue of potentially hazardous targets, in a realistic scenario simulated with SOPAC (Space Object PAss Calculator). Conjunction events are then identified and measurements generated for the relative Orbit Determination (OD) process. The filter is based on the analytical Least Squares, providing results directly at the nominal Time of Closest Approach, without the need to further propagate the solution. The reference trajectory is computed with SGP4 to achieve higher accuracy with lower computational time, suitable for a space-based solution. A classic Unscented Kalman Filter is then used to validate the results, with observations coming from a set of three ground stations part of the EU SST (EU Space Surveillance and Tracking) sensor network.

Overall, the proposed method allows for accurate conjunction analysis directly onboard, in a fraction of the time typically required for refined OD algorithms. In future, it could provide fully autonomous threat detection and initial orbit determination, greatly improving safety and efficiency of space activities.

Keywords: Relative orbit determination, Optical sensor, Batch filter, Space Surveillance and Tracking, Conjunction analysis, B-plane, SGP4

Sommario

Negli ultimi anni, il crescente numero di lanci di satelliti ha aumentato il rischio di collisioni in orbita. Metodi di mitigazione, come le manovre anti-collisione, richiedono un'accurata previsione della congiunzione per evitare il ripetersi di frammentazioni catastrofiche come l'evento Iridium-33/Cosmo-2251, in cui non è stata intrapresa alcuna azione a causa di informazioni non aggiornate. La possibilità di effettuare queste operazioni direttamente a bordo permetterebbe di ridurre notevolmente l'onere delle infrastrutture di terra, migliorando la sostenibilità dell'ambiente spaziale.

In questa tesi, un satellite in orbita bassa, basato su COSMO-SkyMed 4, è equipaggiato con un sensore ottico e un'analisi statistica viene realizzata per determinare le prestazioni della camera di bordo in termini di visibilità, rispetto a un catalogo di bersagli potenzialmente pericolosi, in uno scenario realistico simulato con SOPAC (Space Object PAss Calculator). Vengono quindi identificate le congiunzioni e generate le misure per il processo di determinazione orbitale relativa. Il filtro è basato sul metodo dei minimi quadrati analitico, che fornisce risultati direttamente al tempo di minima distanza nominale, senza la necessità di propagare ulteriormente la soluzione. La traiettoria di riferimento è calcolata con SGP4 per ottenere una maggiore accuratezza con un tempo computazionale inferiore, adatto a un sistema satellitare. Per validare i risultati è stato quindi utilizzato un classico filtro di Kalman Unscented, con osservazioni ottenute da una serie di tre stazioni di terra parte della rete di sensori EU SST (EU Space Surveillance and Tracking).

Complessivamente, il metodo proposto consente un'accurata analisi delle congiunzioni direttamente a bordo in una frazione del tempo tipicamente richiesto da algoritmi di OD di tipo refined. In futuro, potrebbe garantire il rilevamento delle minacce e la determinazione orbitale iniziale in modo completamente autonomo, miglirando notevolmente la sicurezza e l'efficienza delle attività spaziali.

Parole chiave: Determinazione orbitale relativa, Sensore ottico, Filtro batch, Sorveglianza e Tracciamento Spaziale, Analisi della congiunzione, B-plane, SGP4

Contents

1 | Introduction

Since the beginning of space race in 1957, human-made satellites and debris, generally called Resident Space Objects (RSOs), have accumulated in Earth orbit and now pose a potential threat to any space activity. Today the sector is dominated by scientific and commercial mission operated directly by an increasing number of private companies. All the activities left traces not only in the form of active or decommissioned satellites, but also spent upper stages, fragments generated by lost of mechanical integrity due to the space environment or anti-satellite tests, alone responsible for thousands of debris. According to the latest Space Environment Report published by the European Space Agency in 2022, there are more than 30000 orbiting objects bigger than 10 cm, the majority of which lying in Low Earth Orbit (LEO) and Geosynchronous Equatorial Orbit (GEO) [8]. Debris ranging from 1 mm to 1 cm are estimated in hundreds of millions. Due to the high relative velocities, even smaller objects can cause critical damages to operational satellites, leading to premature mission ending, or pose actual hazards to human spaceflight missions. Even worse, bigger debris collisions can be catastrophic events generating clouds of thousands of smaller objects; one example is the collision between Iridium-33 and Cosmos 2251 that produced more than 2300 tracked objects in 2009. The evolution of space objects in all orbits is highlighted in Figure 1.1, where the consequences of these events are clearly visible. Debris distribution is higher in LEO and GEO orbits, where the majority of Earth observation and telecommunication satellites typically operate.

In the last 20 years, an average of 11.7 non-deliberate fragmentations occurred every year, which is reduced to 2.6 if the lifetime of the generated fragments is considered a relevant factor. Still, the increase in satellite launches poses a significant conjunction risk and, in absence of serious mitigation approaches, the number of collisions will rise leading in the long term, to the “Kessler Syndrome” [19]. The number of RSOs would become so high that any collision would result in a cascade effect further increasing the likelihood of fragmentations and leading to completely unavailable orbit regions; on this regard, Figure 1.2 is quite emblematic.

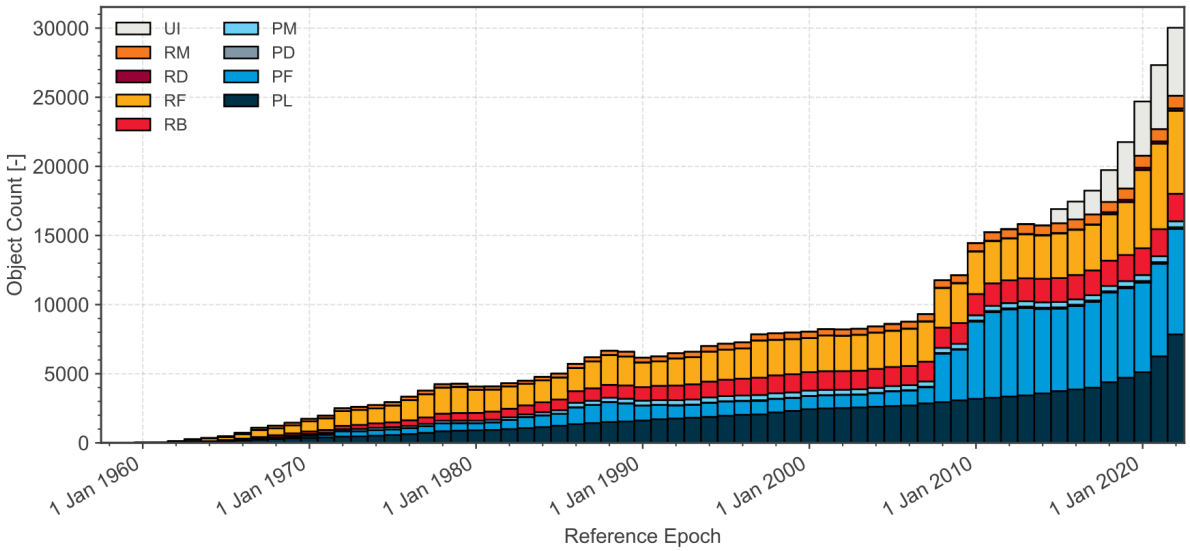

Figure 1.1: Evolution of number of RSOs in geocentric orbit by object class: UI (Unidentified), RM (Rocket Mission Related Object), RD (Rocket Debris), RF (Rocket Fragmentation Debris), RB (Rocket Body), PM (Payload Mission Related Object), PD (Payload Debris), PF (Payload Fragmentation Debris), PL (Payload) [8]

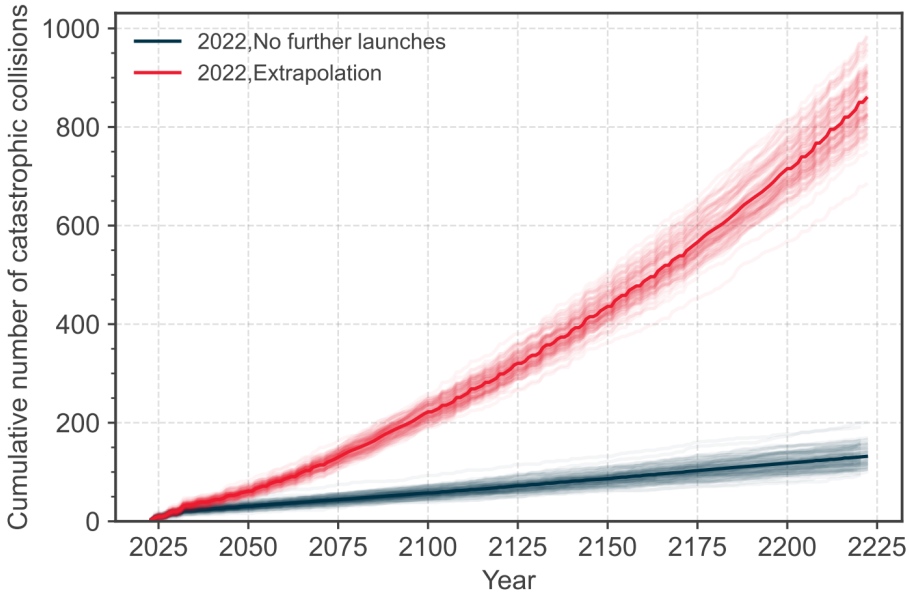

Figure 1.2: Number of cumulative collisions in LEO for long-term environment evolution [8]

Therefore, to mitigate the growth of space objects three solutions have been identified, involving active debris removal, post mission disposal and Collision Avoidance Manoeuvre (CAM). While the former is only at study level, the last two are both effective methods

becoming more and more necessary with the increase of satellite launches. In particular, CAMs require accurate information about the motion of the potentially hazardous debris and this is nowadays done thanks to ground stations tracking and observation.

1.1. Motivation and goals

Considering that even impacts from smaller objects can cause serious damage to an operational satellite, it is of the utmost importance to prevent fragmentation events occurring from bigger debris collisions. To avoid potentially catastrophic close encounters the orbital motion of these objects is frequently updated through Two-Line Element sets (TLE). A TLE provides a list of orbital elements at a given epoch which can be used to propagate the object state typically using the simplified perturbation models, *SGP4* or *SDP4*. The former is the preferred method for LEO trajectories, with orbital period lower than 225 minutes, thanks to a more accurate drag effect implementation.

The probability of collision is the main parameter used to describe a conjunction event and decide whether a CAM is required. Thus, the value must be estimated with the highest possible accuracy to avoid a recurrence of events such as the Iridium-Cosmos collision described before, where the minimum distance predicted by *CeleStrak* was more than 500 meters and a manoeuvre was deemed unnecessary. This kind of conjunctions occur numerous times every day and accurate orbit determination processes are more and more required. With the increasingly high number of satellites in orbit, the burden on ground infrastructure may lead to slower update rate for the estimated motion and higher risk of collision. For this reason, in the last years efforts have focused on autonomous satellite navigation, capable of performing observations and computing the probability of collision directly onboard. Ground infrastructure would still be responsible of the asset motion determination, while the satellite could receive the TLEs, detect potential threat and more accurately analyze the conjunctions.

The goal of this research is thus to understand the performance of an onboard optical sensor in terms of target visibility in a given region of space. The expected outcome is a statistical analysis covering various parameters to identify the advantages and the limitations of space-based observations with respect to typical ground stations. Once the nominal close encounters are identified, measurements are simulated and the proposed algorithm is used to perform refined orbit determination (ROD) and conjunction analysis; the objective is to accurately estimate target state and probability of collision, comparable to the results provided by a typical ground-based network in a fraction of the computational time.

1.2. State of the art

The assessment of a sensor suite performance are not always evaluated from real data and, in case of new design solutions, the possibility to accurately simulate the space environment along with measuring instruments is extremely valuable. At European level, three different tools have been developed to provide data for Space Surveillance and Tracking (SST) services: *BAS3E* (Banc d'Analyse et de Simulation d'un Systeme de Surveillance de l'Espace - Simulation and Analysis Bench for Space Surveillance System), *S3TOC* (Spanish Space Surveillance and Tracking Operations Center) and *SENSIT* (Space Surveillance Sensor Network Simulation Tool). The first one is a complete SST framework developed by CNES (Centre Nationale d'études spatiales) implementing both ground and space-based sensors with object detection, tracking, orbit determination and maintenance of debris catalogue [23]. Similarly, S3TOC provides objects catalogue maintenance from SST observations obtained through the Spanish Space Surveillance and Tracking Sensor Network S3TSN with sensor planning and fragmentation messages [12]. Finally, SENSIT is an Italian software developed by Politecnico di Milano in collaboration with the Italian Space Agency and SpaceDyS company, providing similar functionalities for the modeling of sensor networks and catalogue build-up and maintenance; G. Purpura et al. provided an overview of the three software with a focus on SENSIT [26].

The knowledge of debris motion requires the implementation of filtering algorithms, which process measurements to obtain position and velocity estimates. Various methods have been developed in the last two centuries, with the Least Squares being one of the oldest and most famous technique. The first exposition was published by Legendre in 1805, while the application for calculating celestial bodies orbits was done by Gauss in 1809 (though he claimed to have already developed it in 1795) [14]. The other big family of filters is called *sequential*, allowing to process observations in real-time. The first mathematical description was done by R.E. Kalman in 1960 and was soon adopted in space missions as the Apollo program, with different variants developed in the following years, the most famous being the Extended Kalman Filter (EKF) [33]. Tapley et al. made a quite comprehensive research on the argument, along with typical reference systems and orbital motion modeling [27]. If a satellite is equipped with one or more navigation sensors it can directly take measurements and solve the orbit determination problem onboard, as done by J.S. Ardaens and G. Gaias as part of the AVANTI experiment (Autonomous Vision Approach Navigation and Target Identification). A technological demonstrator was conducted in 2016 successfully showing the validity of the proposed algorithm implemented on the Earth observation satellite BIROS. AVANTI adopted a Least Square method for

the filtering of angles-only measurements provided by the onboard camera [17].

Eventually, the analysis of a close encounter between two objects is done through a bi-dimension reference frame, defined only by two positional coordinates and typically referred to as *b-plane*; the mathematical description is provided by Valsecchi et al. for asteroids or comets, though it is perfectly valid also for non-massive objects, like satellites and debris [31]. The computation of the probability of collision is extremely complex if an exact value is required, taking into account the two objects shapes and appendages. Chan provided an elegant solution approximating the satellite as spheres, greatly simplifying the probability calculations with sufficiently accurate results for most preliminary analysis [3].

In this thesis, the space-based optical sensor is realistically simulated with SOPAC (Space Object PAss Calculator), a Python library developed as a core the SENSIT software for the computation of target passages over a given sensor network. A statistical analysis is then carried out to evaluate the performance of the onboard camera with respect to a catalogue of hazardous objects; this would provide an important insight on the observational opportunities and target visibility of space-based systems. A batch filter, similar to the one adopted for the AVANTI experiment, is thus implemented to perform relative OD and conjunction analysis, computing the probability of collision directly onto the B-plane at the TCA.

1.3. Thesis outline

The research is divided in four main parts. In *Chapter 2* the fundamental concepts and the main formulas needed for the addressed problem are described. The first section is devoted to the orbit determination problem, where the typical measurement systems and reference frames are presented, along with the filtering methods used in this thesis; Section 2 provides a mathematical description of conjunction analysis and collision probability. The first part of the simulation is shown in *Chapter 3*, where the scenario is defined and the optical sensor performance are evaluated in the subsequent sensitivity analysis, allowing to determine any possible correlation with respect to the considered object catalogue. The results of the statistics can be used to identify closer conjunction events, for which it is deemed necessary to perform onboard orbit determination. The adopted methodology is fully described in *Chapter 4* with the required assumption and mathematical models, while in *Chapter 5* the results of the relative orbit determination and conjunction analysis are shown and discussed; a similar ground-based scenario is also defined to validate the onboard simulation and compare the two solutions in terms of computational time and

estimation accuracy. Eventually, work conclusions and possible future outcomes and developments are drawn in *Chapter 6*. In *Appendix* A the Unscented Transform is briefly presented to deepen the UKF concepts, while in *Appendix* B a more detailed description of orbital motion modeling is presented, to gain further insight on the main perturbations, how they can be modeled and affect the performance of an estimation algorithm.

2 | Fundamentals

Here are presented the fundamentals of orbit determination and conjunction analysis, needed for the specific methodology developed in this thesis and described in *Chapter 4*. The orbit determination (also referred as OD) is the problem of estimating the state of an object by means of measurements acquired from one or more sensors. However, the mathematical model adopted for the reference trajectory propagation does not represent exactly the true motion, mainly due to unmodeled forces and approximated physical constants. Moreover, also measurements are affected by random and systematic errors. The result is a statistical optimization problem, which aims at estimating the state of a spacecraft at a given epoch with a non-zero covariance matrix. The typical measurements are nonlinear functions of the state and are generally classified according to the sensor type. Radars can measure two angles, azimuth and elevation, in addition to the range and range-rate. On the contrary, optical sensors provide angles-only measurements, namely right ascension and declination; the description and mathematical models are detailed in *Section 2.1.1*. The ability to more accurately determine the motion of an orbiting objects is fundamental when dealing with satellite conjunctions, where the probability of collision becomes non-negligible. It is thus necessary to perform OD to achieve a more accurate knowledge of the relative position and determine if a collision avoidance manoeuvre (CAM) is actually needed. In a conjunction analysis, the two spacecrafts are represented in a specific bi-dimensional frame, defined B-plane, which allows to describe the event with only two positional coordinates. This method is widely used thanks to the lower computational cost required for CAM design when dealing with a reduced object state.

2.1. Orbit determination

If the state $\boldsymbol{X}_0$ of a spacecraft orbiting the Earth is known at a certain epoch t_0, the equations of motion can be integrated to determine the state at an arbitrary time t. However, as mentioned above, both the initial state, the physical constants and the forces specification of the differential equation system, are never exactly known. The resulting predicted

trajectory will diverge from the actual motion, as shown in Figure 2.1. Therefore, the spacecraft is tracked and observed to gather enough measurements and compute a more accurate estimation of the state. Considering the nonlinearities described above, a typical approach is based on linearization and consequent estimation of the displacement with respect to the reference state.

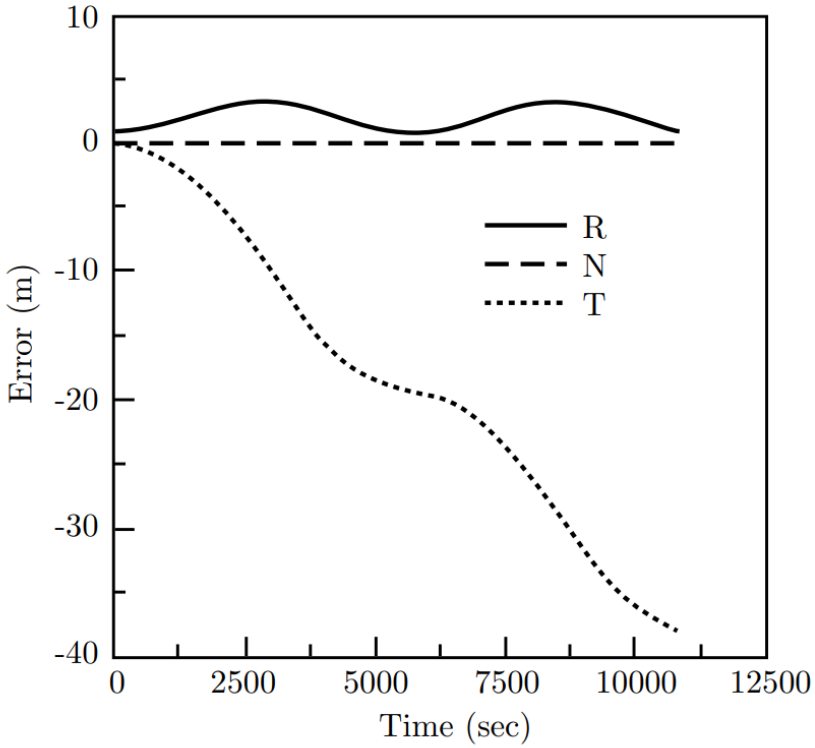

Figure 2.1: Error evolution with respect to the unperturbed orbit due to a 1 meter radial perturbation at $t = 0$. The three components are radial (R), tangential (T) and normal to the orbit plane (N) [27].

2.1.1. Measurements

The most common tracking stations available to date are based on radar or optical sensors. They differ mainly on the type of measurements and the specific reference frames used for their description, briefly outlined below.

Optical sensors

Optical telescopes measure the angular position of a spacecraft in an inertial frame, typically the Earth Centered Inertial, or simply ECI. The ECI is a fixed frame with respect to the stars, with zero acceleration of its origin, located in the center of the Earth. A com-

mon coordinate system for Earth orbiting objects is the *J2000*, also known as *EME2000* or *ICRF* (International Celestial Reference Frame)[1] [25]. The $x-y$ plane lies on the equator, with the x axis directed towards the intersection between the equator and the ecliptic plane, called *Vernal equinox*. The z axis is normal to the mean equator at epoch J2000 TDB (Barycentric Dynamical Time)[2]. This is approximately coincident with the Earth's spin axis orientation at that specific epoch. Eventually, the y axis complete the right-handed frame as the cross product between z and x.

Given the celestial sphere, the celestial equator and the projection of the spacecraft on the sphere, two angles can be defined to describe the position vector in the inertial J2000 frame, Right Ascension and Declination (also referred to *RADEC*):

- Right Ascension, α: Angle measured from the Vernal point to the hour circle, along the equator, defined from 0 to 360 degrees.
- Declination, δ: Angle measured along the hour circle, positive towards the z axis, defined from -90 to 90 degrees.

Figure 2.2 shows the adopted convention for the definition of the RADEC.

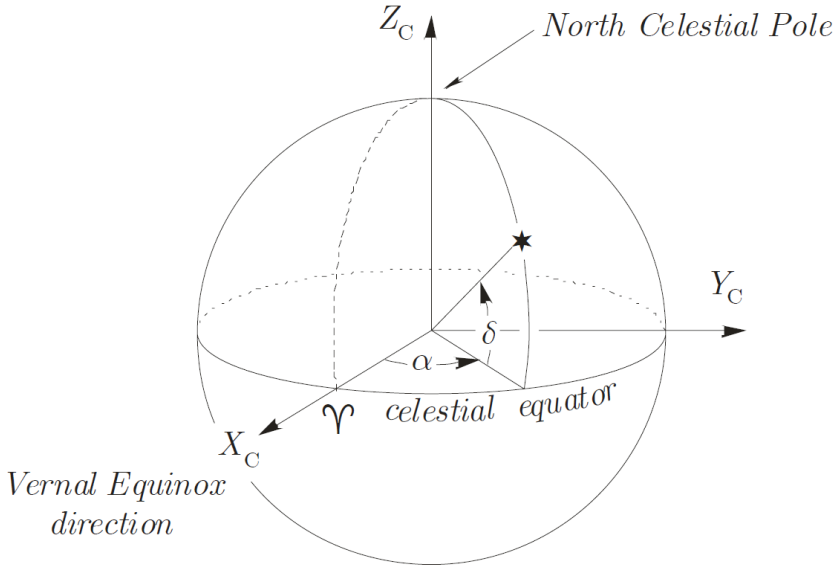

Figure 2.2: Right Ascension and Declination definition [5]

[1] Actually the ICRF is defined by the adopted locations of 295 radio source and it is therefore slightly different from the J2000 by a very small rotation of less than 0.1 arc-seconds. This variation is often considered negligible, and the two systems are in fact regarded as identical.

[2] The TDB is related to the International Atomic Time (TAI), a time scale based on cesium atomic clocks. Coordinated Universal Time (UTC) is derived from TAI with the main difference being the introduction of *leap seconds* to maintain synchronization. For further details on time definitions, cross-reference to [27]

Optical sensors can operate in two possible modes:

- Staring, where the telescope compensate for the rotation of the Earth. As a result, stars are seen as fixed dots, while spacecrafts as small segments, called tracklets.
- Tracking, where the telescope follows the orbiting object, which is now seen as a dot.

The angular information is gathered by comparing the image with the RADEC of known stars taken from a catalogue (astrometric reduction). Since the camera image has not infinite resolution there is uncertainty regarding the exact values of the angles associated to a certain star. Moreover, measurements are provided at specific epochs, but the size of the tracklet is linked to the camera exposure time, which leads to uncertainty on the exact epoch to be assigned. Overall, typical errors for optical sensors are still extremely low, in the range of few arcseconds. Their high accuracy, coupled with the low power consumption and high detection range, makes them widely used both for ground and space-based navigation.

Radar sensors

Radar sensors are based on the transmission of a highly directional signal towards the spacecraft and its reception with a sufficiently high power, or SNR (Signal to Noise Ratio), to be effectively detected. Once the signal is correctly received, the object is assigned with the pointing angles of the radar. However, it is not possible to distinguish the direction inside the Field of View (FoV) which, albeit small, is always greater than zero. This leads to an important source of error in the angular measurement, in the order of 0.1 degrees or more.

Due to the peculiar working principle, radar measurements are often described in local, non inertial frames, also called topocentric. A topocentric reference frame is a coordinate system attached to a point on the surface of the Earth and it is thus useful in the description of satellite motion from a ground-based observer. A typical, earth fixed, non-inertial topocentric frame is shown in Figure 2.3 and defined as follows:

- z_t along the local vertical direction, positive outwards
- x_t positive eastwards
- y_t positive northwards

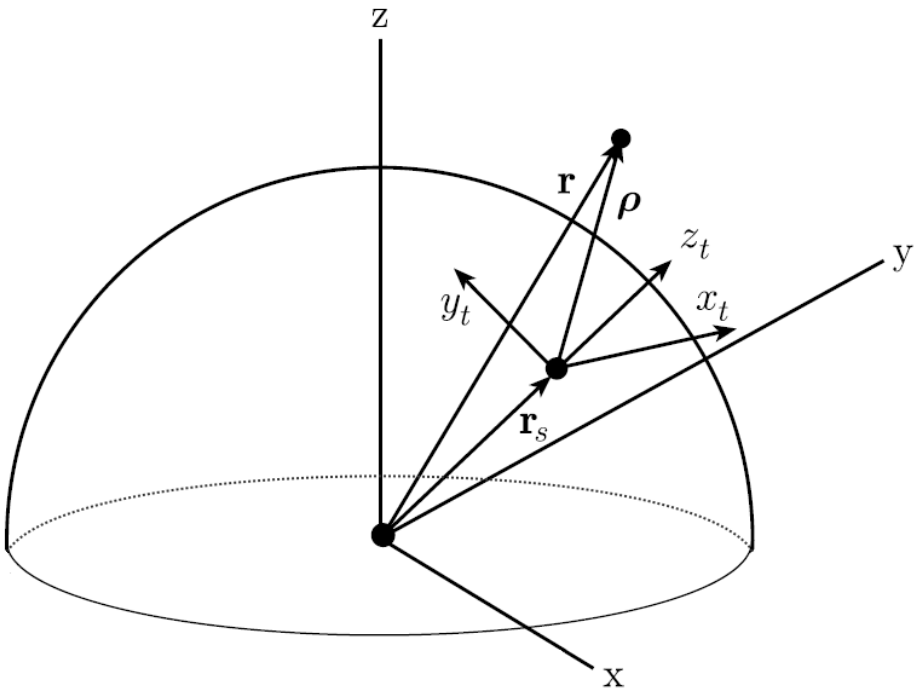

Figure 2.3: Topocentric coordinates x_t, y_t, z_t. $\boldsymbol{r}_s$ is the vector identifying the origin of the coordinate system [27]

The position of a satellite expressed in this topocentric system as $(x, y, z)_t$ can be related to two angular measurements, the most common being *Azimuth* and *Elevation*, as expressed in Equation (2.1).

$$\begin{cases} \sin(El) = \dfrac{z_t}{r_t}, & -90^\circ \leqslant El \leqslant 90^\circ \\ \sin(Az) = \dfrac{x_t}{r_{xy}}, & 0^\circ \leqslant Az \leqslant 360^\circ \\ \cos(Az) = \dfrac{y_t}{r_{xy}}. \end{cases} \tag{2.1}$$

where $r_{xy} = \sqrt{x_t^2 + y_t^2}$. Azimuth is measured from North in a eastward direction, while Elevation is measured from the local horizon, $(x, y)_t$, plane. Despite their lower accuracy, radars can provide two additional measurements, range and range-rate. The former is simply the distance between the station and the spacecraft at a given epoch, while the second if given by the first derivative of range. Hence, they are both scalar functions of the state and are generally computed as in Equation (2.2), where subscript I refers to instrument position and velocity.

$$\begin{cases} \rho = ((\boldsymbol{r} - \boldsymbol{r}_I) \cdot (\boldsymbol{r} - \boldsymbol{r}_I))^{1/2} \\ \dot{\rho} = \dfrac{(\boldsymbol{v} - \boldsymbol{v}_I) \cdot (\boldsymbol{r} - \boldsymbol{r}_I)}{\rho}. \end{cases} \tag{2.2}$$

Accuracy on these quantities is generally much higher, respectively less than 50 m and about 1 m/s, partly offsetting the lower angular resolution. Still, radars have limited range capabilities and high power consumption, which makes them less suitable for a space-based platform. The relation above refers to the particular case of *one-way range*, such that the ground stations operates as transmitter while the spacecraft is equipped with a receiver (or vice versa). For the more general *two-way range* the radar can be defined as mono-static or bi-static. In the former, both transmitter and receiver (TX and RX) locations are coincident, and the measured range is twice the effective distance. On the other hand, for a bi-static radar, TX and RX have different locations and the measured range is given by the summation of the distance transmitter-spacecraft and spacecraft-receiver.

2.1.2. The linear navigation problem

As shown in the previous section, the nature of the measurements and the spacecraft dynamics inevitably introduce nonlinear relationships, written in general form in Equation (2.3).

$$\begin{cases} \dot{\boldsymbol{X}} = F(\boldsymbol{X}, t), \quad \boldsymbol{X}(t_k) = \boldsymbol{X}_k \\ \boldsymbol{Y}_i = G(\boldsymbol{X}_i, t_i) + \boldsymbol{\epsilon}_i, \quad \text{with} \quad i = 1, ..., l \end{cases} \tag{2.3}$$

where $\boldsymbol{X}_k$ is the unknown state vector at epoch t_k of dimension n, while $\boldsymbol{Y}_i$ for $i = 1, ..., l$, is a p-dimensional vector of observations and $\boldsymbol{\epsilon}$ represent the observational error. The total number of measurements is thus $m = p \times l >> n$ and they are used to compute the best estimate of $\boldsymbol{X}_k$. Note that in general, at each observation time, there are fewer measurements than the state unknown dimension. The solution to the OD problem under these considerations is often referred to *nonlinear navigation problem*.

However, if the relation between the state and the observation vectors can be linearized, then the estimation process is greatly simplified and become more suited for a low computational cost algorithm. Given a reference trajectory $\boldsymbol{X}^*(t)$ sufficiently close to the real trajectory $\boldsymbol{X}(t)$, it is possible to expand the actual motion through a Taylor series about the reference. Truncating to the first order, the state deviation from the nominal

can be described by a set of linear Ordinary Differential Equations (ODEs) with time-dependent coefficients. Similarly, expanding the observational equation, it is possible to obtain a linear relation also between measurement and the state deviations. As a result, the navigation problem becomes linear and its solution is given by the deviation between the desired true state and the known reference one.

The resulting procedure is described hereafter, defining the state and observation deviations as:

$$\begin{cases} \delta \boldsymbol{x} = \boldsymbol{X} - \boldsymbol{X}^*, \\ \delta \boldsymbol{y}_i = \boldsymbol{Y}_i - \boldsymbol{Y}_i^* \end{cases} \tag{2.4}$$

Expanding both Equations (2.3) in Taylor series and truncating to the first order, one gets:

$$\begin{cases} \dot{\boldsymbol{X}}(t) = F(\boldsymbol{X}, t) \approx F(\boldsymbol{X}^*, t) + \left[\dfrac{\partial F(t)}{\partial \boldsymbol{X}(t)}\right]^* (\boldsymbol{X}(t) - \boldsymbol{X}^*(t)) \\ \boldsymbol{Y}_i = G(\boldsymbol{X}_i, t_i) + \boldsymbol{\epsilon}_i \approx G(\boldsymbol{X}_i^*, t_i) + \left[\dfrac{\partial G)}{\partial \boldsymbol{X}}\right]_i^* (\boldsymbol{X}(t_i) - \boldsymbol{X}^*(t_i)) \end{cases} \tag{2.5}$$

The term $\left[\dfrac{\partial F(t)}{\partial \boldsymbol{X}(t)}\right]^*$ represent the jacobian evaluated along the nominal trajectory. Considering the reference dynamics as $\dot{\boldsymbol{X}}^* = F(\boldsymbol{X}^*, t)$ it is possible to write the first equation in the form of deviations. The same procedure is applied to the second relation to obtain the final linear expression of the navigation problem, as shown in Equation (2.6).

$$\begin{cases} \delta \dot{\boldsymbol{x}}(t) = A(t)\delta \boldsymbol{x}(t) \\ \delta \boldsymbol{y}_i = \tilde{H}_i \delta \boldsymbol{x}_i + \boldsymbol{\epsilon}_i, \quad i = 1, ..., l \end{cases} \tag{2.6}$$

where $A(t) = \left[\dfrac{\partial F(t)}{\partial \boldsymbol{X}(t)}\right]^*$ and $\tilde{H}_i = \left[\dfrac{\partial G}{\partial \boldsymbol{X}}\right]_i^*$.

The general solution to the first equation is typically expressed as:

$$\delta \boldsymbol{x}(t) = \Phi(t, t_k)\delta \boldsymbol{x}_k, \quad \text{with} \quad \delta \boldsymbol{x}_k = \delta \boldsymbol{x}(t_k) \tag{2.7}$$

The matrix $\Phi(t, t_k)$ is called State Transition Matrix, or *STM* and it will be treated separately in the next section.

2.1.3. The State Transition Matrix

The general spacecraft dynamics shown in Equation (2.3) allows to compute the state at any given epoch with its knowledge at a time t_k. However, the initial condition may be affected by uncertainties and perturbations, which are then propagated through the integration process. In this scenario, the solution at time t is given by the flow of the ODE, generally expressed as Equation (2.8).

$$\boldsymbol{X}(t) = \phi(\boldsymbol{X}_0, t_0; t) \tag{2.8}$$

However, the analytical solution to the spacecraft equations of motion exist only for keplerian orbits in implicit form. In general, the computation of the flow is particularly difficult and the ODEs are integrated numerically. When dealing with perturbed motion, this solution is highly inefficient as dynamics is integrated for all the perturbed initial conditions.

A possible alternative is represented by linearization about the unperturbed motion and can be applied if the displaced trajectory is "close enough" to the reference, which translates to:

- Avoiding highly nonlinear dynamics
- Small initial displacements
- Short term propagations.

Let's consider the flow of the perturbed motion as:

$$\boldsymbol{X}(t) + \delta\boldsymbol{x}(t) = \phi(\boldsymbol{X}_0 + \delta\boldsymbol{x}_0, t_0; t) \tag{2.9}$$

Expanding to the first order with respect to $\delta\boldsymbol{x}_0$:

$$\phi(\boldsymbol{X}_0 + \delta\boldsymbol{x}_0, t_0; t) \approx \phi(\boldsymbol{X}_0, t_0; t) + \frac{\partial\phi}{\partial\boldsymbol{x}_0}(\boldsymbol{X}_0, t_0; t)\delta\boldsymbol{x}_0 \tag{2.10}$$

Equation (2.10) is then substituted in (2.9), to obtain:

$$\boldsymbol{X}(t) + \delta\boldsymbol{x} \approx \phi(\boldsymbol{X}_0, t_0; t) + \frac{\partial\phi}{\partial\boldsymbol{x}_0}(\boldsymbol{X}_0, t_0; t)\delta\boldsymbol{x}_0 \tag{2.11}$$

By definition $\boldsymbol{X}(t) = \phi(\boldsymbol{X}_0, t_0; t)$ and the first terms of the left and right hand side of

Equation (2.11) cancel out, leading the final expression shown in Equation (2.12).

$$\delta \boldsymbol{x} = \frac{\partial \phi}{\partial \boldsymbol{x}_0}(\boldsymbol{X}_0, t_0; t)\delta \boldsymbol{x}_0 \tag{2.12}$$

The term $\frac{\partial \phi}{\partial \boldsymbol{x}_0}(\boldsymbol{X}_0, t_0; t)$ is the jacobian of the flow and it is simply called State Transition Matrix, expressed as $\Phi(\boldsymbol{X}_0, t_0; t)$ or simply $\Phi(t_0, t)$. Although it is only an approximated solution, the STM is a linear analytical map between small displacements at two given epochs. Therefore, it allows to easily compute the final displacement from a reference trajectory, given an initial perturbation, without the need to fully integrate the nonlinear dynamic ODEs. Given an initial state $\tilde{\boldsymbol{X}}_0$ displaced with respect to the nominal solution, the process is easily exemplified:

- Compute $\delta \boldsymbol{x}_0 = \tilde{\boldsymbol{X}}_0 - \boldsymbol{X}_0$
- Use the linear map of the STM $\delta \boldsymbol{x} = \Phi(t_0, t)\delta \boldsymbol{x}_0$
- Get the displaced solution as $\tilde{\boldsymbol{X}} = \boldsymbol{X} + \delta \boldsymbol{x}$

Finally, applying the map at $t = t_0$ it is possible to find the value of $\Phi(t_0, t_0)$, which is simply equal to a 6×6 identity matrix.

Computation of the STM

The State Transition Matrix can be computed according to two different method: finite differences and variational approach. The latter is here presented.

Given the linearized dynamics expression shown in the first Equation (2.6), the general solution will have the form:

$$\delta \boldsymbol{x}(t) = \Phi(t_0, t)\delta \boldsymbol{x}_0 \tag{2.13}$$

Computing the first derivative of Equation (2.13) and rearranging:

$$\dot{\Phi}(t_0, t)\delta \boldsymbol{x}_0 = \delta \dot{\boldsymbol{x}}(t) \tag{2.14}$$

Substituting $\delta \dot{\boldsymbol{x}}(t)$ from the linearized equation of motion and recalling the general solution shown in Equation (2.13), it is possible to write:

$$\dot{\Phi}(t_0, t)\delta \boldsymbol{x}_0 = A(t)\Phi(t_0, t)\delta \boldsymbol{x}_0 \tag{2.15}$$

Since this must held true for any initial displacement $\delta \boldsymbol{x}_0$, the final expression of the STM

dynamics becomes:

$$\dot{\Phi}(t_0, t) = A(t)\Phi(t_0, t) \tag{2.16}$$

with initial condition $\Phi(t_0, t_0) = I_{6\times6}$, leading to a system of 36 ODEs.

However, to integrate the above system, the jacobian $A(t)$ must be computed along the reference trajectory. Therefore, the complete system requires the integration of the spacecraft nominal motion, as shown in Equation (2.17).

$$\begin{cases} \dot{\boldsymbol{X}}(t) = F(\boldsymbol{X}, t) \\ \dot{\Phi}(t_0, t) = A(t)\Phi(t_0, t) \\ \text{with initial conditions:} \\ \boldsymbol{X}(t_0) = \boldsymbol{X}_0^* \\ \Phi(t_0, t_0) = I_{6x6} \end{cases} \tag{2.17}$$

The result is thus a system of 42 scalar ODEs.

Although the variational approach provides the exact STM, it needs the computation of the jacobian (performed through symbolic manipulators) and it can't be applied with a discontinuous dynamics with respect to the state.

Properties of the STM

The most useful properties of the State Transition Matrix are stated below and derived directly from Equation (2.13) and (2.14).

- $\Phi(t_k, t_k) = I_{6\times6}$
- $\Phi(t_i, t_k) = \Phi(t_i, t_j)\Phi(t_j, t_k)$
- $\Phi(t_i, t_k) = \Phi^{-1}(t_k, t_i)$

If the matrix $A(t)$ can be written in partitioned form as shown in Equation (2.18), then the following properties hold true for the submatrices: $A_1^T = -A_4$, $A_2^T = A_2$ and $A_3^T = A_3$.

$$A(t) = \begin{bmatrix} A_1 & A_2 \\ A_3 & A_4 \end{bmatrix} \tag{2.18}$$

Then also the STM can be similarly partitioned and its inverse can be written as:

$$\Phi^{-1}(t_k, t) = \begin{bmatrix} \Phi_4^T & -\Phi_2^T \\ -\Phi_3^T & \Phi_1^T \end{bmatrix} \tag{2.19}$$

Application of the STM to the linear navigation problem

From Equation (2.6) it is clear that for each observation correspond an unknown state deviation $\delta\boldsymbol{x}$ at time t_i. It is thus desirable to relate each measurement to the state at a single epoch by means of the STM. This allows to reduce the number of unknowns form $l \times n$ to just n. Therefore, remembering the linear map of Equation (2.13), it is possible to substitute $\delta\boldsymbol{x}_i = \Phi(t_k, t_i)\delta\boldsymbol{x}_k$ into the measurement equation. The result, for each observation, takes the form:

$$\begin{cases} \delta\boldsymbol{y}_1 = \tilde{H}_1\Phi(t_k, t_1)\delta\boldsymbol{x}_k + \boldsymbol{\epsilon}_1 \\ \delta\boldsymbol{y}_2 = \tilde{H}_2\Phi(t_k, t_2)\delta\boldsymbol{x}_k + \boldsymbol{\epsilon}_2 \\ \vdots \\ \delta\boldsymbol{y}_l = \tilde{H}_l\Phi(t_k, t_l)\delta\boldsymbol{x}_k + \boldsymbol{\epsilon}_l \end{cases} \tag{2.20}$$

Overall, there are $m = p \times l$ measurements and only $\delta\boldsymbol{x}_k$ as unknown, with dimension n.

Equation (2.20) can be written in a more convenient form defining:

$$\delta\boldsymbol{y} = \begin{pmatrix} \delta\boldsymbol{y}_1 \\ \vdots \\ \delta\boldsymbol{y}_l \end{pmatrix}; \qquad H = \begin{bmatrix} \tilde{H}_1\Phi(t_k, t_1) \\ \vdots \\ \tilde{H}_l\Phi(t_k, t_l) \end{bmatrix}; \qquad \boldsymbol{\epsilon} = \begin{pmatrix} \boldsymbol{\epsilon}_1 \\ \vdots \\ \boldsymbol{\epsilon}_l \end{pmatrix} \tag{2.21}$$

Equation (2.22) is a system of m equations in $n + m$ unknowns, due to the presence of the error vector $\boldsymbol{\epsilon}$. Indeed, $\delta\boldsymbol{y}$ is a $m \times 1$ vector, $\delta\boldsymbol{x}_k$ $n \times 1$ and H $m \times n$. Remembering that $m = p \times l$ the total number of unknowns is actually n state components plus m observation errors. The Least Squares method presented in Section 2.1.4 provides the condition on this last unknown to find a solution for state deviation at time t_k.

$$\delta\boldsymbol{y} = H\delta\boldsymbol{x}_k + \boldsymbol{\epsilon} \tag{2.22}$$

2.1.4. The Least Squares solution

The Least Square method is part of the family of OD filters that process an entire measurement batch to find the spacecraft state at a specific epoch. They are opposed to the well-known *sequential filters* that process observations sequentially, providing the estimated state at each step; they will be described in more details in the next section.

The Least Square solution aims at finding the value of the state $\hat{\boldsymbol{x}}_k$ that minimizes the sum of the squares of the observation residuals, as shown in Equation (2.23). Mathematically, the problem can be expressed with the following statement:

$$\text{find} \quad \hat{\boldsymbol{x}}_k \quad \text{that minimize} \quad J = \frac{1}{2}\boldsymbol{\epsilon}^T\boldsymbol{\epsilon} \tag{2.23}$$

The choice of the sum of the squares allows to have an always positive J unless each observation error is equal to zero.

Substituting $\boldsymbol{\epsilon}$ from Equation (2.22), the performance index becomes:

$$J(\boldsymbol{x}) = \frac{1}{2}(\delta\boldsymbol{y} - H\delta\boldsymbol{x}_k)^T(\delta\boldsymbol{y} - H\delta\boldsymbol{x}_k) \tag{2.24}$$

J is now a quadratic function of $\boldsymbol{x}$ and a unique minima exists only if:

$$\frac{\partial J}{\partial \boldsymbol{x}_k} = 0, \quad \text{and} \quad \delta\boldsymbol{x}_k^T\frac{\partial^2 J}{\partial \boldsymbol{x}_k^2}\delta\boldsymbol{x}_k > 0 \ \text{ for all } \ \delta\boldsymbol{x}_k \neq 0 \tag{2.25}$$

Imposing the first derivative equal to zero allows to find the value of the best estimate of the state deviation, written as $\delta\hat{\boldsymbol{x}}_k$:

$$(H^TH)\delta\hat{\boldsymbol{x}}_k = H^T\delta\boldsymbol{y} \tag{2.26}$$

The Least Square solution to the navigation problem can be written by inverting the matrix H^TH, called *normal matrix*, as shown in Equation (2.27). The invertibility condition is found imposing the second requirement of Equation (2.25), which implies that the second derivative of J with respect to the unknown state is symmetric and positive definite. In particular, it can be found that $\frac{\partial^2 J}{\partial \boldsymbol{x}_k^2} = H^TH$. Matrix H^TH is a $n \times n$ symmetric matrix and it satisfies the requirement only if it is full rank, thus at least n independent observations are needed.

$$\delta\hat{\boldsymbol{x}}_k = (H^TH)^{-1}H^T\delta\boldsymbol{y} \tag{2.27}$$

Finally, it can be noted that the matrix $(H^TH)^{-1}H^T$ is actually the pseudo-inverse of H.

The above solution lacks any statistical information regarding the measurements errors. The minimum variance estimate here presented allows to overcome this limitation and compute the covariance associated to the state estimate.

Minimum variance estimate

The minimum variance estimate is based on the main assumption that the observation error $\boldsymbol{\epsilon}$ is a random vector with zero mean and assigned covariance.

$$E[\boldsymbol{\epsilon}] = \begin{pmatrix} E[\boldsymbol{\epsilon}_1] \\ \vdots \\ E[\boldsymbol{\epsilon}_l] \end{pmatrix} = \mathbf{0}, \quad E[\boldsymbol{\epsilon}\boldsymbol{\epsilon}^T] = \begin{bmatrix} R_{11} & R_{12} & \dots & R_{1l} \\ R_{12}^T & R_{22} & \dots & R_{2l} \\ \vdots & & \ddots & \vdots \\ R_{1l}^T & & \dots & R_{ll} \end{bmatrix} = R \tag{2.28}$$

In general diagonal terms of R are coincident, while off-diagonal terms are set to to zero, though this is not a necessary condition, as $R_{ij} \neq 0$ $(i \neq j)$ may be associated to time-correlated observation errors (measurement at t_i is affected by measurement at t_j).

Given the measurement equation (2.22), the problem statement requires finding the linear, minimum variance estimate $\delta\hat{\boldsymbol{x}}_k$ of $\delta\boldsymbol{x}_k$.

From the first requirement, the solution must be a linear combination of the observation vector:

$$\delta\hat{\boldsymbol{x}}_k = M\delta\boldsymbol{y} \tag{2.29}$$

Moreover, the solution must be valid also for the ideal case of perfect measurements, $\boldsymbol{\epsilon} = \mathbf{0}$, and perfect knowledge of $\delta\boldsymbol{x}_k$. Under this consideration, the system can be written as:

$$\begin{cases} \delta\boldsymbol{y} = H\delta\boldsymbol{x}_k \\ \\ \delta\boldsymbol{x}_k = M\delta\boldsymbol{y} \end{cases} \tag{2.30}$$

Substituting $\delta\boldsymbol{y}$ in the second equation leads to the constraint shown in Equation (2.31).

$$MH = I \tag{2.31}$$

Therefore, the problem now requires to find M that minimize the variance of the spacecraft state $\boldsymbol{x}_k$.

$$P_k = E[(\delta\boldsymbol{x}_k - \delta\hat{\boldsymbol{x}}_k)(\delta\boldsymbol{x}_k - \delta\hat{\boldsymbol{x}}_k)^T] \tag{2.32}$$

The resulting performance index is expressed in Equation (2.33), with the constraint $MH = I$ enforced through the matrix of Lagrange multiplier Λ.

$$J = \frac{1}{2}E[(\delta \boldsymbol{x}_k) - \delta\hat{\boldsymbol{x}}_k)(\delta \boldsymbol{x}_k) - \delta\hat{\boldsymbol{x}}_k)^T] + \Lambda(I - MH) \tag{2.33}$$

The previous equation is generally written as a scalar function by imposing the minimization of the variance trace.

From the general Equation (2.22) substituted in (2.29), one gets:

$$\delta\hat{\boldsymbol{x}}_k = MH\delta\boldsymbol{x}_k + M\boldsymbol{\epsilon} \tag{2.34}$$

which is then replaced in the expression of P_k shown in Equation (2.32) to obtain the relation for the variance matrix:

$$P_k = MRM^T \tag{2.35}$$

Therefore, the final expression of the index J is given by Equation (2.36).

$$J = \frac{1}{2}tr[MRM^T] + tr[\Lambda(I - MH)] \tag{2.36}$$

with the necessary condition for the minimization of J being:

- $\dfrac{\partial J}{\partial M} = 0$
- $\dfrac{\partial J}{\partial \Lambda} = 0$

Which leads to the set of Equations (2.37), applying simple matricial algebra.

$$\begin{cases} MR - \Lambda^T H^T = 0 \\ I - MH = 0 \end{cases} \tag{2.37}$$

Substituting the first in the second and rearranging conveniently, the final expression of M is shown in Equation (2.38).

$$M = (H^T R^{-1} H)^{-1} H^T R^{-1} \tag{2.38}$$

Reminding Equation (2.29), the minimum variance solution and the estimated state co-

variance are expressed as:

$$\begin{cases} \delta\hat{\boldsymbol{x}}_k = (H^T R^{-1} H)^{-1} H^T R^{-1} \delta\boldsymbol{y} \\ P_k = (H^T R^{-1} H)^{-1} \end{cases} \tag{2.39}$$

It may happen that an estimate of the spacecraft state and covariance are available at a previous time t_j and they can be used to improve the Least Square solution. The problem of *a priori information* is reduced to the already analyzed minimum variance considering the previous state as an observation of $\delta\boldsymbol{x}_k$ with noise $R_k = P_k^-$. The augmented variables are shown in Equation (2.40).

$$\delta\boldsymbol{y}_e = \begin{pmatrix} \delta\boldsymbol{y} \\ \delta\hat{\boldsymbol{x}}_k^- \end{pmatrix}, \quad \boldsymbol{\epsilon}_e = \begin{pmatrix} \boldsymbol{\epsilon} \\ \boldsymbol{\eta}_k \end{pmatrix}, \quad H_e = \begin{bmatrix} H \\ I \end{bmatrix}, \quad R_e = \begin{bmatrix} R & 0 \\ 0 & P_k^- \end{bmatrix} \tag{2.40}$$

where $\delta\hat{\boldsymbol{x}}_k^-$ is the a priori state deviation, $\boldsymbol{\eta}_k$ the unknown error vector and P_k^- the a priori covariance.

Therefore, the problem can be written in the classic form as shown by Equation (2.41):

$$\delta\boldsymbol{y}_e = H_e \delta\boldsymbol{x}_k + \boldsymbol{\epsilon}_e \tag{2.41}$$

Recalling the minimum variance estimate, the a posteriori state deviation and covariance matrix is expressed in Equation (2.42).

$$\begin{cases} \delta\hat{\boldsymbol{x}}_k^+ = (H^T R^{-1} H + (P_k^-)^{-1})^{-1} (H^T R^{-1} \delta\boldsymbol{y} + (P_k^-)^{-1} \delta\hat{\boldsymbol{x}}_k^-) \\ P_k^+ = (H^T R^{-1} H + (P_k^-)^{-1})^{-1} \end{cases} \tag{2.42}$$

It is interesting to notice that there are two limiting cases to this solution:

- Very poor a priori information, leading to $P_k^- \to \infty$
- Very poor measurements, leading to $R \to \infty$

In the first case $(P_k^-)^{-1}$ will tend to zero and the solution will be the one shown in Equation (2.39). On the contrary, if the measurements are affected by large errors, with $R^{-1} \to 0$, the solution becomes equal to the a priori estimate.

2.1.5. Sequential filters

In sequential filters measurements are processed as soon as they are received. For a generic step t_{k-1} to t_k, two passages are performed:

- prediction: uncertainty propagation from $k-1$ to k. The covariance enlarges
- update: computation of covariance P_k^+, smaller than P_k^-.

The more measurements are available, the closer to zero the covariance gets, as shown in Figure 2.4.

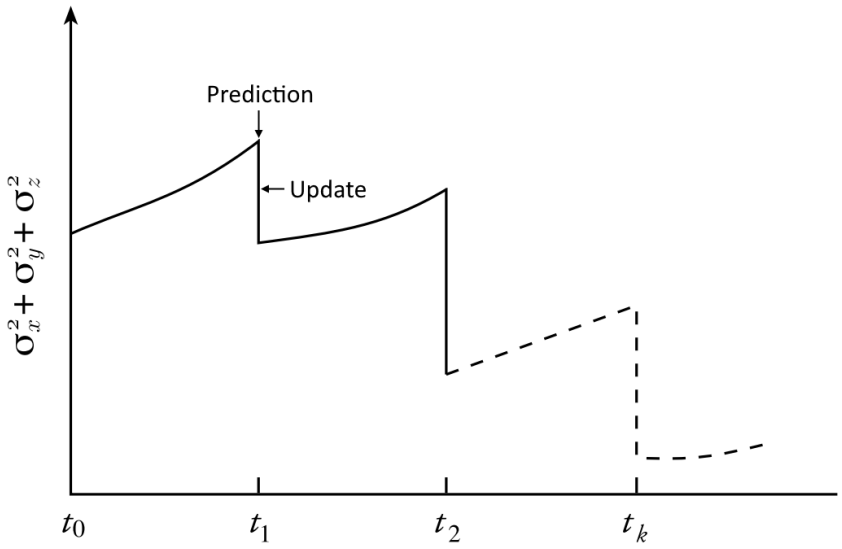

Figure 2.4: Typical covariance trace trend in a sequential filter.

The most famous sequential filter is the Kalman filter, first developed in 1960. Since then, many variations were provided to offer improved performance and accuracy. The Unscented Kalman Filter (UKF) here presented, compared to the popular Extended Kalman Filter (EKF), provides greater accuracy in estimating the mean and covariance and better convergence performance. Nevertheless, the UKF is more computationally expensive and is therefore used for the orbit determination process performed by ground stations.

Unscented Kalman Filter

The UKF is based on the Unscented Transform (again, UT for simplicity) to predict mean and covariance of the state and of the measurements. The UT allows to abandon the linear method in order to achieve a greater prediction accuracy, without resorting to a highly expensive Monte Carlo simulation. An important difference with respect to a classic Kalman filter lies in the computation of the measurements mean and covariance,

as they can't be derived from the nonlinear relation (2.43) and are rather computed from the propagated *sigma points*.

$$\hat{\boldsymbol{y}}_k = G(\hat{\boldsymbol{x}}_k, t_k) \tag{2.43}$$

A more detailed description of the Unscented Transform is presented in Appendix A. For a generic step $t_{k-1} \rightarrow t_k$, the UKF is summarized in Algorithm 2.1, given a priori information $\hat{\boldsymbol{x}}^+_{k-1}$, P^+_{k-1}, measurements $\boldsymbol{y}_k$ and matrix R_k.

Algorithm 2.1 Unscented Kalman Filter

1: Compute sigma points $\boldsymbol{\chi}_{i,k-1}$ and the associated weights $W_i^{(m)}$ and $W_i^{(c)}$
2: Prediction steps: $\downarrow$
3: **for** *each sigma point* **do**
4: Propagate the sigma point to time t_k: $\dot{\boldsymbol{\chi}}_{i,k} = F(\boldsymbol{\chi}_{i,k}, t_k)$
5: Compute the sigma points of the predicted measurements: $\boldsymbol{Y}_{i,k} = G(\boldsymbol{\chi}_{i,k})$
6: **end for**
7: Compute the a priori mean state: $\hat{\boldsymbol{x}}^-_k = \sum_{i=0}^{2n} W_i^{(m)} \boldsymbol{\chi}_{i,k}$ with n the state dimension
8: Compute the a priori state covariance: $P^-_k = \sum_{i=0}^{2n} W_i^{(c)} [\boldsymbol{\chi}_{i,k} - \hat{\boldsymbol{x}}^-_k][\boldsymbol{\chi}_{i,k} - \hat{\boldsymbol{x}}^-_k]^T + Q_k$
9: Compute the a priori measurements mean: $\hat{\boldsymbol{y}}^-_k = \sum_{i=0}^{2n} W_i^{(m)} \boldsymbol{Y}_{i,k}$
10: Update step: $\downarrow$
11: Compute measurement covariance: $P_{yy,k} = \sum_{i=0}^{2n} W_i^{(c)} [\boldsymbol{Y}_{i,k} - \hat{\boldsymbol{y}}^-_k][\boldsymbol{Y}_{i,k} - \hat{\boldsymbol{y}}^-_k]^T + R_k$
12: Compute cross-covariance: $P_{xy,k} = \sum_{i=0}^{2n} W_i^{(c)} [\boldsymbol{\chi}_{i,k} - \hat{\boldsymbol{x}}^-_k][\boldsymbol{Y}_{i,k} - \hat{\boldsymbol{y}}^-_k]^T$
13: Compute Kalman gain: $K_k = P_{xy,k} P^{-1}_{yy,k}$
14: Compute a posteriori mean and covariance:
$\hat{\boldsymbol{x}}^+_k = \hat{\boldsymbol{x}}^-_k + K_k(\boldsymbol{y}_k - \hat{\boldsymbol{y}}^-_k)$
$P^+_k = P^-_k - K_k P_{yy,k} K_k^T$

Q_k is the process noise and is implemented to take into account the difference between the adopted dynamical model and the real motion. Indeed, the more observations are available, the closer to zero the covariance gets (as in Figure 2.4); in the limiting case, the kalman gain tends to zero and the estimation becomes insensitive to any new measurement. If the process noise is considered as a white Gaussian noise then it is possible to directly sum it to the compute covariance P^-_k [11].

As mentioned at the beginning of this chapter, the orbit determination problem is never solved exactly, due to the mathematical model, observation errors, numerical accuracy and so on. Therefore, it may be advantageous to simply neglect unknown (or poorly known) model parameters to reduce the computational cost and avoid observability problems when trying to estimate their value. In this thesis, the primary spacecraft motion cannot

be estimated with the linearized model proposed in *Chapter* 4, and it is thus considered to be fully known. This is a strong assumption that must be considered in the post-processing of the results. A possible technique to deal with this problem is thus presented in the next section.

2.1.6. The Consider Covariance Analysis

The Consider Covariance Analysis (CCA) aims at assessing the impact of non-estimated parameters, neglected during the filtering process. The state vector is thus estimated without considering those parameters and their uncertainty is then included in the covariance matrix [27].

Let's consider a generalized state vector $\boldsymbol{z}$ and resulting mapping matrix H:

$$\delta \boldsymbol{z} = \begin{pmatrix} \delta \boldsymbol{x} \\ \boldsymbol{c} \end{pmatrix}, \quad H = [H_x | H_c] \tag{2.44}$$

$\delta \boldsymbol{x}$ is the $n \times 1$ vector of the secondary spacecraft state deviations, while $\boldsymbol{c}$ if the vector of uncertain parameters that will not be estimated. For the case at study, $\boldsymbol{c}$ is the primary spacecraft state deviation from the reference.

The measurement model can thus be written as:

$$\boldsymbol{y} = H_x \delta \boldsymbol{x} + H_c \boldsymbol{c} + \boldsymbol{\epsilon} \tag{2.45}$$

Assuming that a priori estimates $\delta \bar{\boldsymbol{x}}$ and $\bar{\boldsymbol{c}}$ are available, it follows:

$$\delta \bar{\boldsymbol{x}} = \delta \boldsymbol{x} + \boldsymbol{\eta}, \quad \bar{\boldsymbol{c}} = \boldsymbol{c} + \boldsymbol{\beta} \tag{2.46}$$

The statistical properties of the errors $\boldsymbol{\eta}$ and $\boldsymbol{\beta}$ are presented in Equation (2.47).

$$\begin{cases} E[\boldsymbol{\eta}] = E[\boldsymbol{\beta}] = 0, & \text{(2.47a)} \\ E[\boldsymbol{\eta}\boldsymbol{\eta}^T] = \bar{P}_x, & \text{(2.47b)} \\ E[\boldsymbol{\beta}\boldsymbol{\beta}^T] = \bar{P}_{cc}, & \text{(2.47c)} \\ E[\boldsymbol{\eta}\boldsymbol{\epsilon}^T] = E[\boldsymbol{\beta}\boldsymbol{\epsilon}^T] = 0, & \text{(2.47d)} \\ E[\boldsymbol{\eta}\boldsymbol{\beta}^T] = \bar{P}_{xc}. & \text{(2.47e)} \end{cases}$$

where $\bar{P}_x$ and $\bar{P}_{cc}$ are the a priori covariances of the state and the parameter, while $\bar{P}_{xc}$ is the a priori cross-correlation covariance.

The observation error now includes both $\boldsymbol{\beta}$ and $\boldsymbol{\eta}$, while the augmented measurements vector $\tilde{\boldsymbol{y}}$ contains the a priori estimates of $\delta\boldsymbol{x}$ and $\boldsymbol{c}$. It is therefore possible to find $\boldsymbol{z}$ with a classic Least Squares method, as shown in Equation (2.48).

$$\boldsymbol{z} = (H_z^T \tilde{R}^{-1} H_z)^{-1} H_z^T \tilde{R}^{-1} \tilde{\boldsymbol{y}} \tag{2.48}$$

where:

$$\tilde{R}^{-1} = \begin{bmatrix} R^{-1} & 0 & 0 \\ 0 & \bar{M}_{xx} & \bar{M}_{xc} \\ 0 & \bar{M}_{cx} & \bar{M}_{cc} \end{bmatrix} \tag{2.49}$$

The submatrices are then computed as in Equation (2.50).

$$\begin{cases} \bar{M}_{xx} = (\bar{P}_x - \bar{P}_{xc}\bar{P}_{cc}^{-1}\bar{P}_{xc}^T)^{-1}, & \text{(2.50a)} \\ \bar{M}_{cc} = (\bar{P}_{cc} - \bar{P}_{xc}^T\bar{P}_x^{-1}\bar{P}_{xc})^{-1}, & \text{(2.50b)} \\ \bar{M}_{xc} = -\bar{M}_{xx}\bar{P}_{xc}\bar{P}_{cc}^{-1}. & \text{(2.50c)} \end{cases}$$

The solution provided by Equation (2.48) allows to compute both $\hat{\boldsymbol{c}}$ and P_{cc}. The consider estimate is obtained by fixing them to their a priori values $\bar{\boldsymbol{c}}$ and $\bar{P}_{cc}$. The Algorithm 2.2 shows the required passages for the implementation of the Consider Covariance Analysis with the Least Squares filter described before.

Algorithm 2.2 Consider Covariance

1: $M_{xx} = H_x^T W H_x + \bar{M}_{xx}$
2: $M_{xc} = H_x^T W H_c + \bar{M}_{xc}$
3: $M_{cc} = H_c^T W H_c + \bar{M}_{cc}$
4: $P_x = M_{xx}^{-1}$
5: $S_{xc} = -P_x M_{xc}$
6: $\boldsymbol{N}_x = H_x^T W \delta\boldsymbol{y} + \bar{P}_x \delta\bar{\boldsymbol{x}}$
7: $\delta\hat{\boldsymbol{x}} = M_{xx}^{-1}\boldsymbol{N}_x - M_{xx}^{-1} M_{xc}\bar{\boldsymbol{c}}$
8: $P_{xx} = P_x + S_{xc}\bar{P}_{cc}S_{xc}^T$

Defining:

- W diagonal weight matrix for the Least Square filter, given by the inverse of the sensor accuracy squared
- P_x covariance matrix resulting from the Least Squares filter

- $\delta\bar{\boldsymbol{x}}$ a priori spacecraft state estimate
- $\bar{\boldsymbol{c}}$ a priori consider estimate
- $\delta\hat{\boldsymbol{x}}$ the estimate including the consider parameter
- $M_{xx}^{-1}\boldsymbol{N}_x$ the solution of the Least Squares, not including $\bar{\boldsymbol{c}}$

Generally, the a priori cross-covariance $\bar{P}_{xc}$ can be set to zero, allowing to slightly simplify the analysis. P_{xx} is the augmented target covariance and, by definition of S_{xc}, is always greater than P_x.

2.2. Conjunction Analysis

A conjunction is a close encounter event between two orbiting objects, in general an operative spacecraft called *primary* and an uncooperative one called *secondary*. As described in the previous sections, the state of a spacecraft is never exactly known and this leads to uncertainty in the true relative position. Therefore it is necessary to analyze each conjunction event and determine the possible hazard in terms of probability of collision. If the computed value is higher than a given threshold, a collision avoidance manoeuvre is performed.

2.2.1. B-plane definition

This thesis focus on Low Earth Orbit spacecrafts, where the relative velocities are sufficiently high to consider the encounter as *short-term*. The duration is expressed as:

$$t_c = \frac{2\sigma_\eta}{\|\boldsymbol{v}_p - \boldsymbol{v}_s\|} \tag{2.51}$$

where σ_η is the covariance along the relative velocity vector, $\boldsymbol{v}_p$ and $\boldsymbol{v}_s$ the primary and secondary velocity vectors in ECI coordinates. A conjunction is defined as short-term if the encounter duration is much smaller than the primary orbit period T_p, as shown in Equation (2.52).

$$\varepsilon = \frac{t_c}{T_p} \ll 1 \approx 10^{-3} \tag{2.52}$$

Under this assumption, the two spacecrafts motion can be approximated as uniform rectilinear, allowing to simplify the expression of the collision probability.

To further streamline the computation, a different conjunction coordinate system can be defined, embedding both satellites at the Time of Closest Approach (TCA) and centered

on the secondary, as shown in Equation (2.53) and Figure 2.5.

$$\boldsymbol{u}_\xi = \frac{\boldsymbol{v}_s \times \boldsymbol{v}_p}{\|\boldsymbol{v}_s \times \boldsymbol{v}_p\|}, \quad \boldsymbol{u}_\eta = \frac{\boldsymbol{v}_p - \boldsymbol{v}_s}{\|\boldsymbol{v}_p - \boldsymbol{v}_s\|}, \quad \boldsymbol{u}_\zeta = \boldsymbol{u}_\xi \times \boldsymbol{u}_\eta. \tag{2.53}$$

The (ξ, ζ) plane is typically referred to as *B-plane*, with rotation matrix from ECI defined as:

$$R_{b,2D} = [\boldsymbol{u}_\xi,\ \boldsymbol{u}_\zeta]^T \tag{2.54}$$

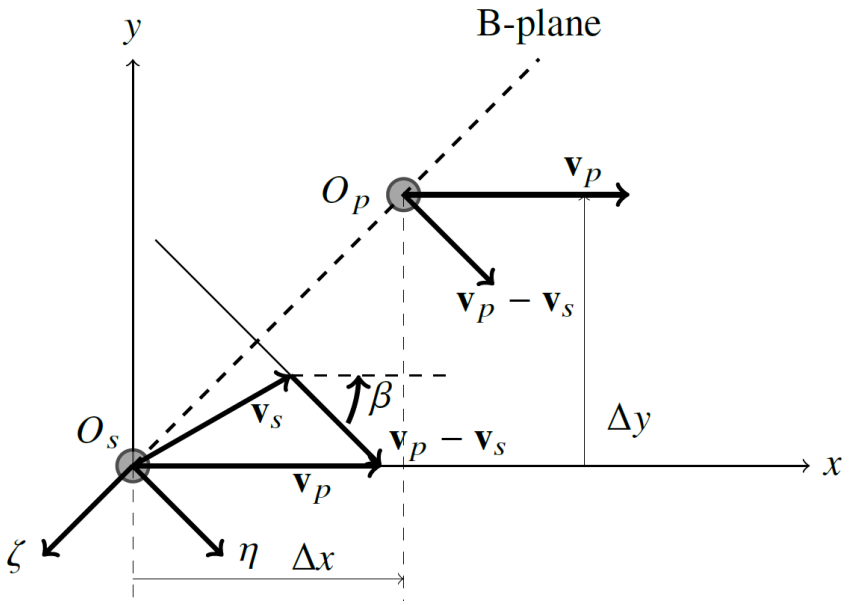

Figure 2.5: B-plane definition and encounter geometry at TCA [4]

The position of the primary spacecraft is then described by the position vector in B-plane coordinates as $\boldsymbol{b} = [\xi,\ \zeta]^T$ [4].

2.2.2. Collision probability

The approach analyzed in [3] allows to obtain an approximated analytical expression of the bi-dimensional collision probability. The two objects are assumed to be spherical, with a *hard-body radius* given by the sum of the two. The collision occurs when the distance between the two spacecrafts is smaller than $r_A = r_p + r_s$.

The probability density function (simply called *pdf*) of the relative position vector is expressed as a three-dimensional Gaussian distribution function of the combined covariance C as shown in Equation (2.55). C is simply computed as the summation of the primary

and secondary covariances defined at the TCA in the B-plane reference frame.

$$f_3(\xi,\eta,\zeta) = \frac{1}{\sqrt{(2\pi)^3\|C\|}} e^{-1/2\boldsymbol{r}^T C\boldsymbol{r}} \tag{2.55}$$

with $\boldsymbol{r}$ the relative position, again, in B-plane coordinates.

The probability of collision of then given by integral of the pdf in the volume swept by the sphere of radius r_A centered at the primary. With the short-term encounter hypothesis, the motion can be assumed to be uniform rectilinear for several standard deviations along the relative velocity direction. The volume swept is then considered as a cylinder extending from $-\infty$ to $+\infty$ and the probability of collision can be computed as the double integral of the bi-dimensional pdf over the cross-sectional area of radius r_A (expressed in Equation (2.56)).

$$f_2(\xi,\zeta) = \frac{1}{2\pi\sigma_\xi\sigma_\zeta\sqrt{1-\rho_{\xi\zeta}^2}} e^{-\frac{\left[\left(\frac{\xi}{\sigma_\xi}\right)^2 - 2\rho_{\xi\zeta}\left(\frac{\xi}{\sigma_\xi}\right)\left(\frac{\zeta}{\sigma_\zeta}\right) + \left(\frac{\zeta}{\sigma_\zeta}\right)^2\right]}{2\left(1-\rho_{\xi\zeta}^2\right)}} \tag{2.56}$$

Being the combined covariance matrix written as:

$$C = \begin{bmatrix} \sigma_\xi^2 & \rho_{\xi\zeta}\sigma_\zeta\sigma_\xi \\ \rho_{\xi\zeta}\sigma_\zeta\sigma_\xi & \sigma_\zeta^2 \end{bmatrix} \tag{2.57}$$

Choosing a new reference frame aligned with the major and minor axis of the error ellipse allows to write the covariance matrix C as diagonal and simplify the expression of f_2.

$$C' = \begin{bmatrix} \sigma_{x'}^2 & 0 \\ 0 & \sigma_{y'}^2 \end{bmatrix} \tag{2.58}$$

From the invariance of the matrix determinant:

$$\sigma_{x'}\sigma_{y'} = \sqrt{1-\rho_{\xi\zeta}^2}\sigma_\xi\sigma_\zeta \tag{2.59}$$

A second change of coordinates is shown in Equation (2.60) to transform the pdf into an isotropic function mapping the ellipses of constant pdf into circles.

$$\begin{cases} x" = \dfrac{\sigma_{z'}}{\sigma_{x'}} x' \\ z" = z' \end{cases} \tag{2.60}$$

Finally, the elliptical cross section can be approximated to a circular one, allowing to write the bi-dimensional isotropic Gaussian pdf into a one-dimensional Rician integral computed with the following convergent series:

$$P_c(u,v) = e^{-v/2} \sum_{m=0}^{\infty} \frac{v^m}{2^m m!} \left[1 - e^{-u/2} \sum_{k=0}^{m} \frac{u^k}{2^k k!} \right] \tag{2.61}$$

where u is the ratio of the impact cross-sectional area to the area of the 1σ covariance ellipse in B-plane coordinates.

$$u = \frac{r_A^2}{\sigma_\zeta \sigma_\xi \sqrt{1 - \rho_{\xi\zeta}^2}} \tag{2.62}$$

v is the squared Mahalanobis distance, computed as $v = \boldsymbol{b}^T C^{-1} \boldsymbol{b}$, with $\boldsymbol{b}$ the B-plane relative position vector and its norm defined as the miss distance [4]. In this thesis, the probability of collision is computed truncating Equation (2.61) to third order, with $m = 3$.

3 | Simulation design

In this chapter the simulation scenario is described. In the first section, an overview of the main parameters and adopted design tools is presented, while Section 3.2 contains the statistical analysis necessary to infer the onboard optical sensor performance. This chapter covers the first 8 days of simulation and the results are then used in *Chapter* 5 to perform relative orbit determination and conjunction analysis for the identified targets.

Figure 3.1: COSMO-SkyMed 4 satellite. *Credit: Telespazio*

3.1. Scenario definition

The simulated scenario consists of an asset and a certain number of objects identified as potentially dangerous. The primary spacecraft is based on the real *COSMO-SkyMed 4*, a dual purpose, civil-military satellite operated since 2010 by the Italian Space Agency (ASI) [1] and depicted in Figure 3.1. It is located in a sun-synchronous orbit at approximately 600 km of altitude, as shown in Table 3.1.

a [km]	e [-]	i [deg]	Ω [deg]	ω [deg]
6990.5	0.0026	98.01	69.18	72.95

Table 3.1: Cosmo-Skymed 4 keplerian parameters

To select only the threatening targets orbiting in the same region of space, the *Advanced CAT Tool* of AGI's STK (System Tool Kit) has been exploited. Setting the desired time window, ellipsoid distance threshold of 20 km and a apogee-perigee filter of 30 km allowed to select 425 different satellites/debris/rocket bodies, each with the expected minimum distance and TCA. Given the NORAD ID, the Two-Line Element sets are retrieved using the *ELSET Search* available from Space Track[1].

The high number of objects orbiting in this region of space allows to have a significant statistical analysis and a sufficient number of conjunction events. In particular, the scenario here presented is simulated from midnight 1st to the midnight 8th September 2022. The spacecraft is equipped with an optical sensor with a limiting magnitude of 15, capable of seeing objects as small as 10 cm up to 6000 km, according to the formulae presented in Equation (3.1) and the resulting Figure 3.2, showing the apparent magnitude as function of the range for spherical object of different radii[2] [24]. In general, even though a radar can provide accurate relative range measurements, it is characterized by a higher power consumption, limited range capabilities and low angular resolution. Therefore, the choice of an optical sensor is preferable for a versatile space-based solution and the onboard camera is the only instrument adopted for the statistical analysis and the subsequent measurement simulation.

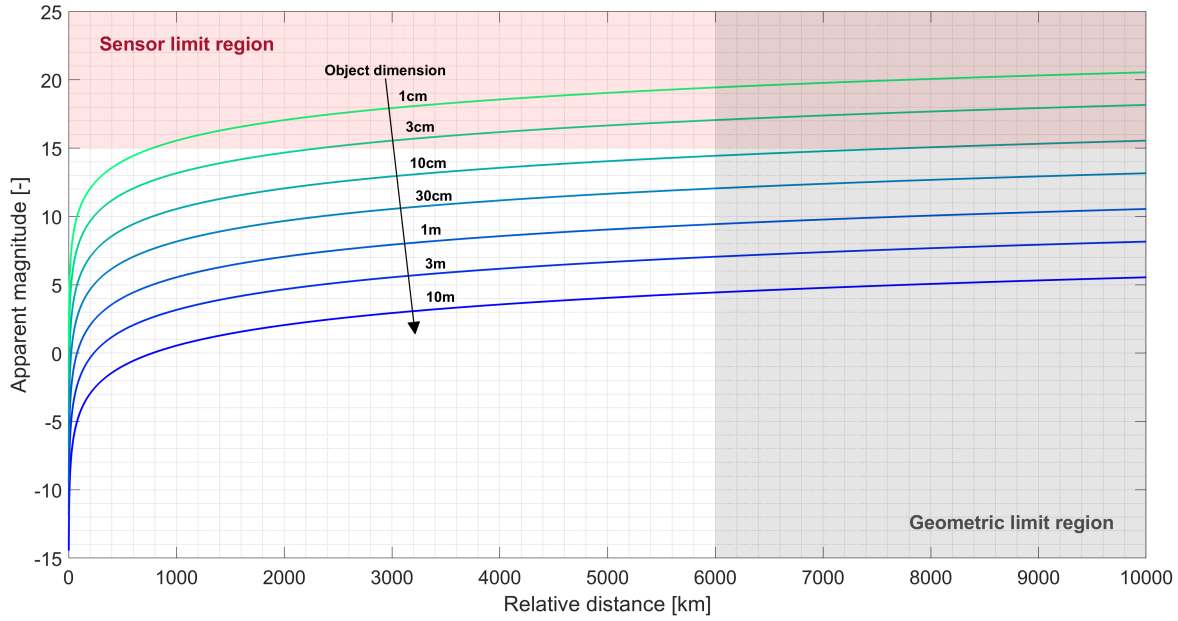

Figure 3.2: Apparent magnitude with relative distance for different target dimensions

[1]The Space Track information can be retrieved free of charge on the official website *www.space-track.org*

[2]6000 km is the maximum geometric visibility range for objects of similar semi-major axis. Spacecrafts with higher eccentricity values may be visible from greater distances, as pictured in Figure 3.2

$$\begin{cases} M = m - 15 + 5\log_{10}(\rho) - 2.5\log_{10}(F(\varphi)) \\ M = -26.78 - 2.5\log_{10}\left(\dfrac{A\zeta F(\varphi)}{\rho^2}\right) \end{cases} \tag{3.1}$$

with $F(\varphi) = (\pi - \varphi)\cos(\varphi) + \sin(\varphi)$ and φ the phase angle[3]. m is the target intrinsic magnitude and it is a function of the cross section A (expressed in km^2) and ζ the object albedo (set at 0.2 for an Aluminum plate) [24]. Finally, ρ is the relative range between the observer and the target satellite. Both equations above allows to compute the apparent magnitude and they can be merged to obtain a relation between m and the target dimension, as shown in Equation (3.2).

$$m = -8.854 - 2.5\log_{10}(A\zeta) \tag{3.2}$$

Information regarding the satellites cross section are retrieved from a 2008 catalogue, covering up to *Norad ID* 40000 and providing the Radar Cross Section (RCS), here assumed to be identical to the effective area. All the non-available objects are estimated considering a normal distribution with mean and variance computed from the catalogue values and written in Table 3.2.

RCS mean $[m^2]$	0.956
RCS standard deviation $[m^2]$	2.291

Table 3.2: Catalogued objects RCS mean and standard deviation

Apart from the geometric constraint given by the presence of the Earth over the line of sight, space-based optical sensors have two additional requirements that must be enforced during the simulation, minimum Sun separation and target illumination. The former is generally valid for every type of sensor due to the impossibility to gather measurements when the angle between the Sun direction and the sensor axis is below a given threshold[4]. This limit is set at 30° for the selected onboard camera. On the contrary, the illumination requirement is specific to optical telescopes, as the target must reflect sunlight in order to be visible. Moon separation is not considered for the onboard sensor, though is generally defined for optical ground stations; minimum Radar Cross Section (RCS) and maximum

[3]The phase angle is defined as the angle between the direction of the observer and the direction of the Sun as seen from the target spacecraft

[4]Being the Sun the most important radio source in the Solar System, also radar sensors are subject to this limit

slant range are instead specific requirements of radar instruments. Table 3.3 provides a summary of the possible limitations for ground and space-based sensors. It is important to notice that there are other possible constraints as maximum and minimum RADEC or Azimuth and Elevation, not included in this analysis, as more related to the sensor-satellite interface rather than the specific sensor type. The camera frame is inertially defined, without any attitude information, pointing towards the expected direction of the target at the beginning of each visibility window, with a total Field of View of 30 degrees.

Limits	**Radar**	**Optical**	**Space-based optical**
Illumination	-	×	×
Sun separation	×	×	×
Moon separation	-	×	-
Min RCS	×	-	-
Max Slant range	×	-	-
Limiting magnitude	-	×	×

Table 3.3: Possible limitations for ground-based and space-based optical and radar sensors.

The visibility of targets with respect to the sensor is computed through *SOPAC* (Space Object PAss Calculator) a python library developed by *Politecnico di Milano* as a core of the SENSIT software suite to compute all the possible observation opportunities on the defined sensor network [9, 26]. The library makes use of NAIF's SPICE Toolkit to perform computations related to the simulation geometry. The sensor is characterized by the limits defined above and set to *tracking* mode, according to the chosen camera frame, as summarized in Table 3.4. The output of SOPAC analysis is a list of windows, for each target, with the starting and ending epoch of visibility. The library takes as input the satellites kernels generated from the provided TLEs with the estimated values of brightness (given by Equation (3.2)) and propagated using the *SGP4* simplified perturbations model, allowing to have a sufficiently accurate simulation over the analyzed time window. Moreover, SGP4 computations are much more efficient than a dedicated propagator and the total computational time is kept under two hours. The algorithm employs the bisection method to identify the exact epochs of visibility based on the defined limits, depending on the sensor type. Furthermore, specific forbidden region can be specified to account for areas of the celestial sphere that are not observable or physical mounting limitations.

Sensor type	Optical
Sensor mode	Tracking
Min Sun separation $[deg]$	30
Limiting magnitude	15

Table 3.4: Optical sensor limits

3.2. Statistical Analysis

The statistical analysis requires the identification of different parameters deemed significant to infer on the visibility of an orbiting object. The selected parameters are as follows:

- Visibility windows: total number of windows identified by SOPAC, for each target
- Visibility time: total time in which the object is actually visible
- Uniformity index: parameter identifying the uniformity of observations along the asset orbit
- Non-visible objects: number of targets not visible in the whole time window
- Maximum visibility range
- Revisit time: minimum, maximum and mean time between two consecutive visibility windows

These are then compared to the mere number of objects, their main keplerian elements, the type of sensor limits or compared with each other, to seek for possible cross-correlations.

Visibility windows

The visibility in terms of total number of windows is here analyzed. In Figure 3.3 the first correlation is presented, considering only the geometrical limit, without illumination, magnitude and Sun separation requirements. Three main orbit parameters are identified as potentially significant: semi-major axis, inclination and right ascension of the ascending node (RAAN from now on). Eccentricity and argument of perigee are not represented. Indeed, the filter provided by STK enforces a maximum difference between the perigee and apogee of target and observer and the information about the eccentricity is already embedded in the semi-major axis. The argument of perigee does not have any influence

on the visibility.

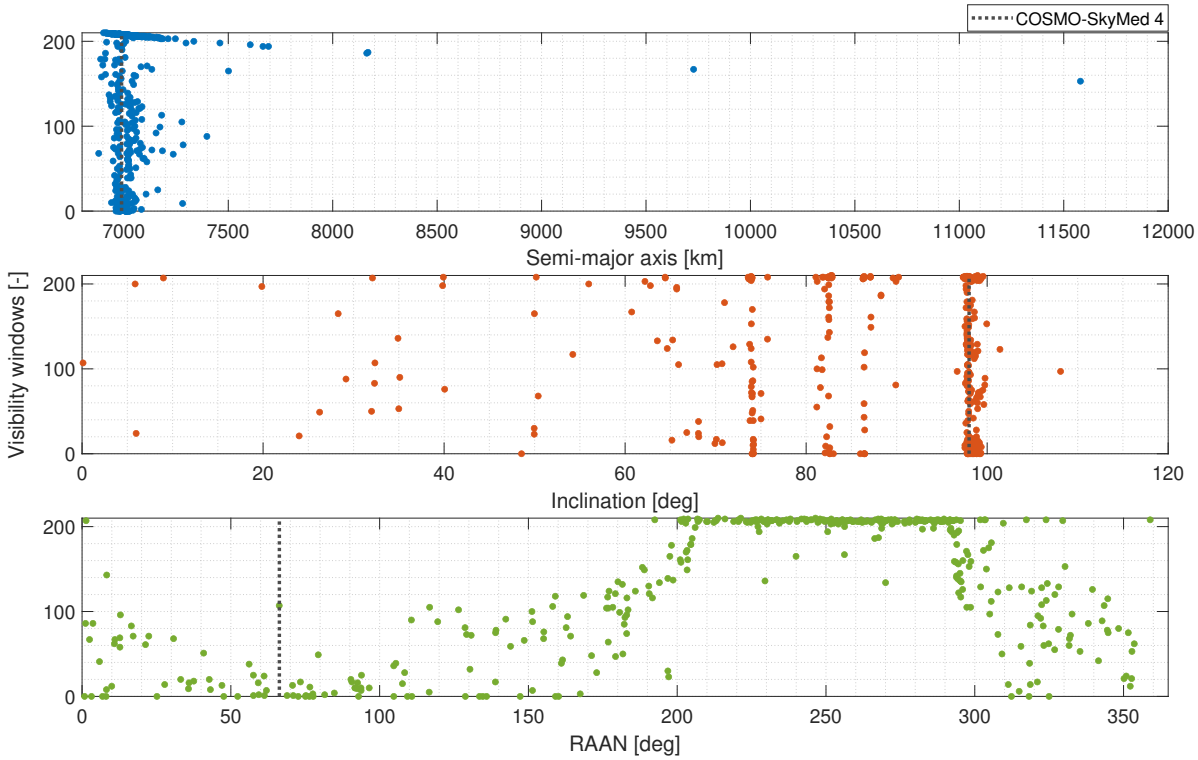

Figure 3.3: Total visibility windows as function of semi-major axis, inclination and RAAN. Only the geometric constraint is applied

The first consideration comes from the maximum value of the visibility windows, at about 200. This is actually expected as the total number of orbits (with a period of about 90/100 minutes) in the considered time window is around 120. As shown in the revisit time graphs, the average time between two windows is rarely less than half a orbit, resulting in a theoretical maximum number just over 200. Moreover, it tends to decrease with increasing semi-major axis, probably due to the higher orbit period (and thus a higher revisit time). The inclination plot does not show any correlation but still highlights that satellites operate in specific orbits and in particular the Sun-synchronous (typically called SSO) are the most populated. Finally, an important correlation is clearly visible in the third graph, where objects with RAAN between 200 and 300 degrees are almost constant at 200 visibility windows. The reason may lie in the difference with respect to COSMO-SkyMed which is approximately 180 degrees apart; this means that the encounters are mostly "head-on", with velocity vectors having opposite orientations. This feature will be further analyzed in the next sections.

The Figure 3.4 reports the percentage of objects with at least the reported number of

visibility windows, for different sensor limits. The blue bar refers to the complete sensor simulation, with illumination, sun separation and limiting magnitude. The red bar contains only the illumination requirement, to verify the impact of the specific sensor characteristics described in Section 3.1 on the number of windows. Finally, the green bar refers to the pure geometrical limitation, allowing to determine the effects of the Earth shadow and thus effects of mounting an optical sensor instead of a radar.

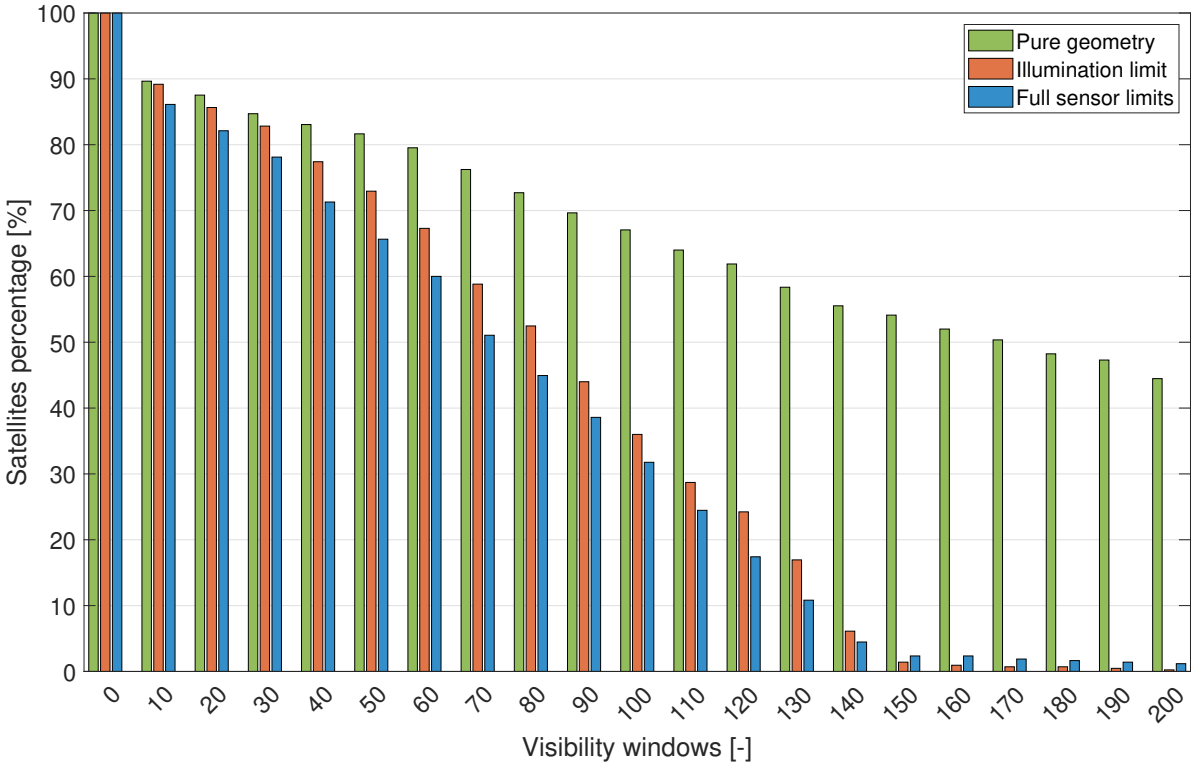

Figure 3.4: Total visibility windows for three different sensor limits: pure geometry, only illumination and full sensor limits

As expected, without limits the number of visibility windows is much closer to the theoretical limit, with about 40% of the objects having more than 200 windows. On the contrary, the blue and red bars are relatively similar with very few percentages above 140, suggesting that the main hindrance to the number of windows is given by the illumination condition, while the limiting magnitude may affect only particularly small objects.

Visibility time

Figure 3.5 shows the total visibility time in hours with respect to semi-major axis, inclination and RAAN. Again only the geometrical limit is enforced to better highlight potential correlations, thus similar remarks to Figure 3.3 can be made. The time is sensibly higher

for the two satellites with $a > 9500$ km, due to the longer period of geometrical visibility, though the sample is too limited for a significant correlation. The RAAN presents two peaks at around 60° and 250°, as expected. The former is more scattered, highlighting that only certain objects are effectively visible for longer periods of time. Indeed, satellites with similar RAAN and similar periods end up chasing each other constantly, leading to a visibility time strongly dependent on the initial relative position.

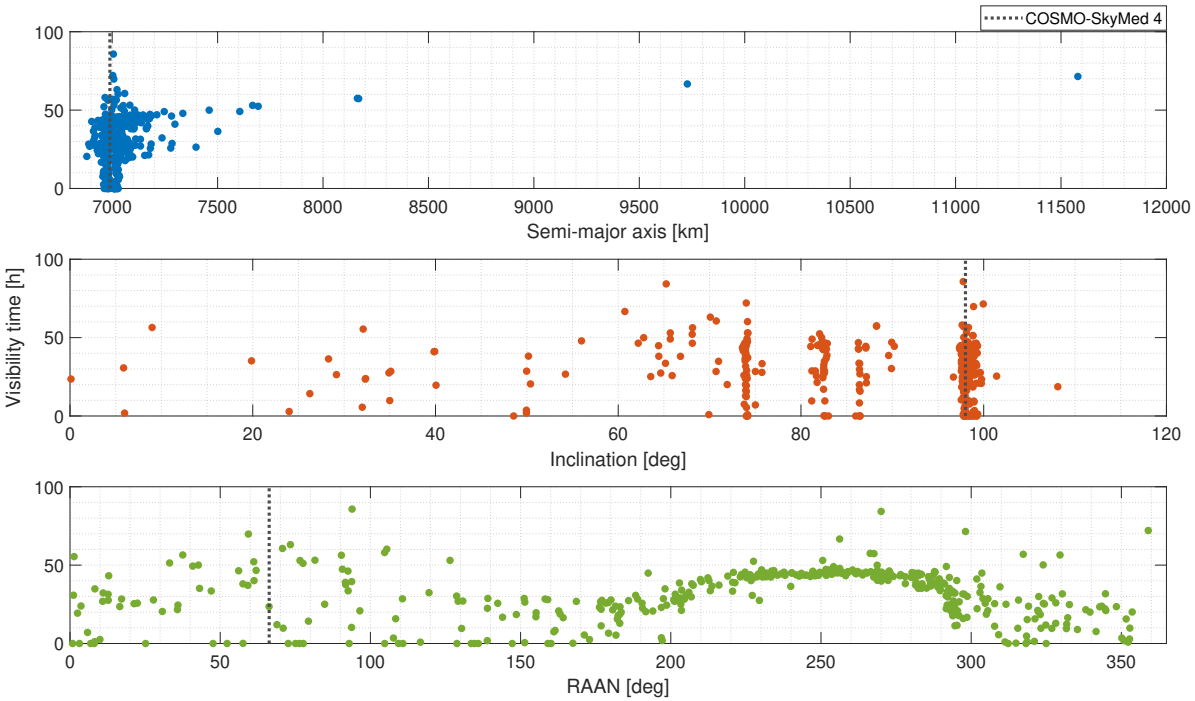

Figure 3.5: Total visibility time, expressed in hours as function of semi-major axis, inclination and RAAN. Only the geometric constraint is applied

The visibility time is then analyzed with the three sensor limits, as done above. Figure 3.6 indicates that both the blue and the red bars are limited to relatively low total times (below 25 hours), while the absence of sensor limitations allows to greatly increase it up to 50 hours.

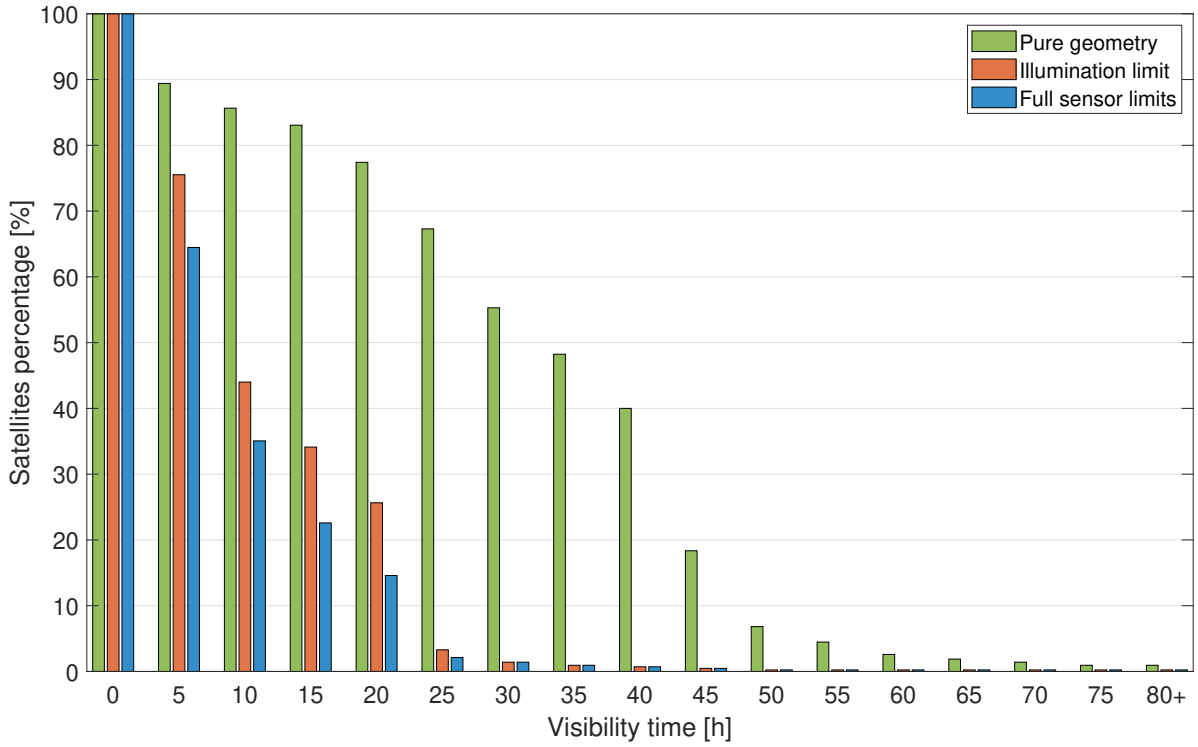

Figure 3.6: Total visibility time (in hours) for three different sensor limits: pure geometry, only illumination and full sensor limits

Uniformity index

The first Figure 3.7 allows to correlate both the number of windows and the uniformity index, with respect to the RAAN, the keplerian parameter with the highest influence on visibility, as illustrated above. The uniformity index is computed dividing the asset orbit in 36 sections (each covering 10° in true anomaly) and counting how many contains at least one potential observation. The index is normalized over the number of sectors to have a value between 0 and 1, resulting in the simple relation $U = n/36$, where n is the number of visible sections. Therefore, it is an indication of the quality of the observations that can be performed for the specific target, as more uniformly distributed measurements provide more accurate result and higher scheduling flexibility. The graph shows a high uniformity index for practically all the object between 200 and 300 degrees of RAAN, enhancing the results above. Again, only geometrical limits are enforced.

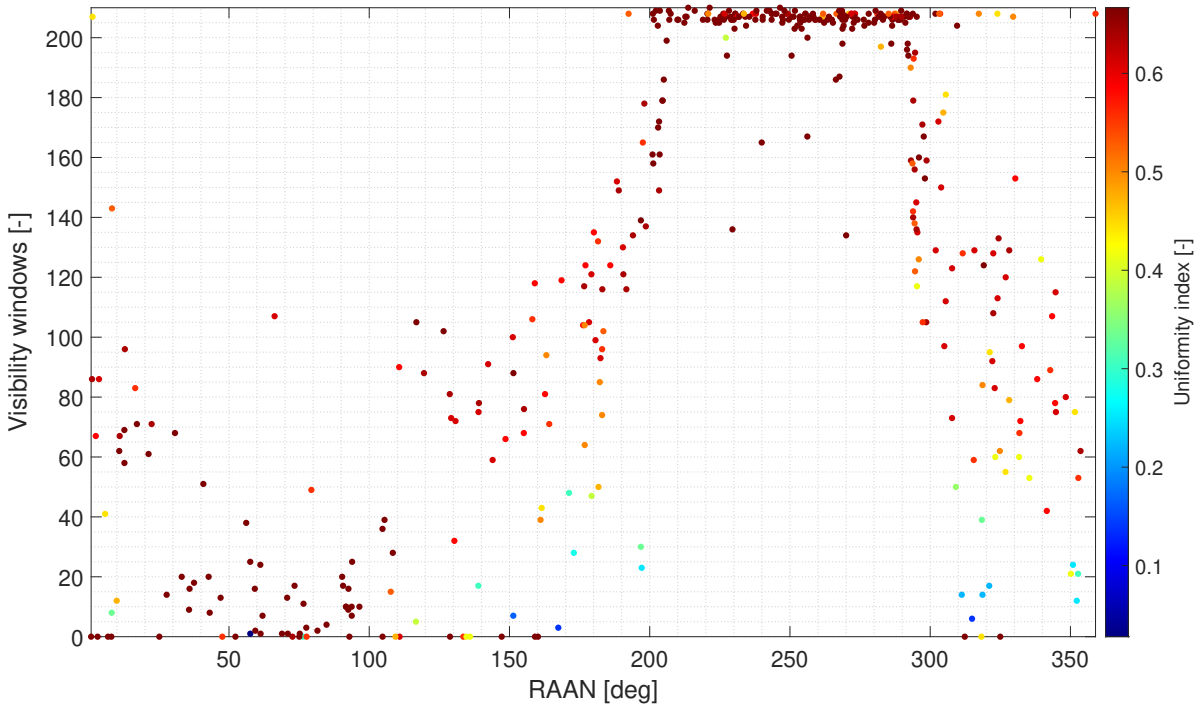

Figure 3.7: Total visibility windows and RAAN as function of the uniformity index. Only the geometric constraint is applied

It is important to notice that the objects with similar RAAN to COSMO are characterized by a lower value of visibility windows, but not necessarily of uniformity. Once again, the same relation is sought with the total visibility time, highlighting very high uniformity when RAAN is around 60 and 250 degrees.

Finally, the distribution of the uniformity index with the three sensor limits is reported in Figure 3.9. When the illumination requirement is enforced, observation uniformity is strongly reduced due to some region of the target orbit being not illuminated; the index worsen with the addition of specific sensor limits caused by a too high relative range with particularly small objects.

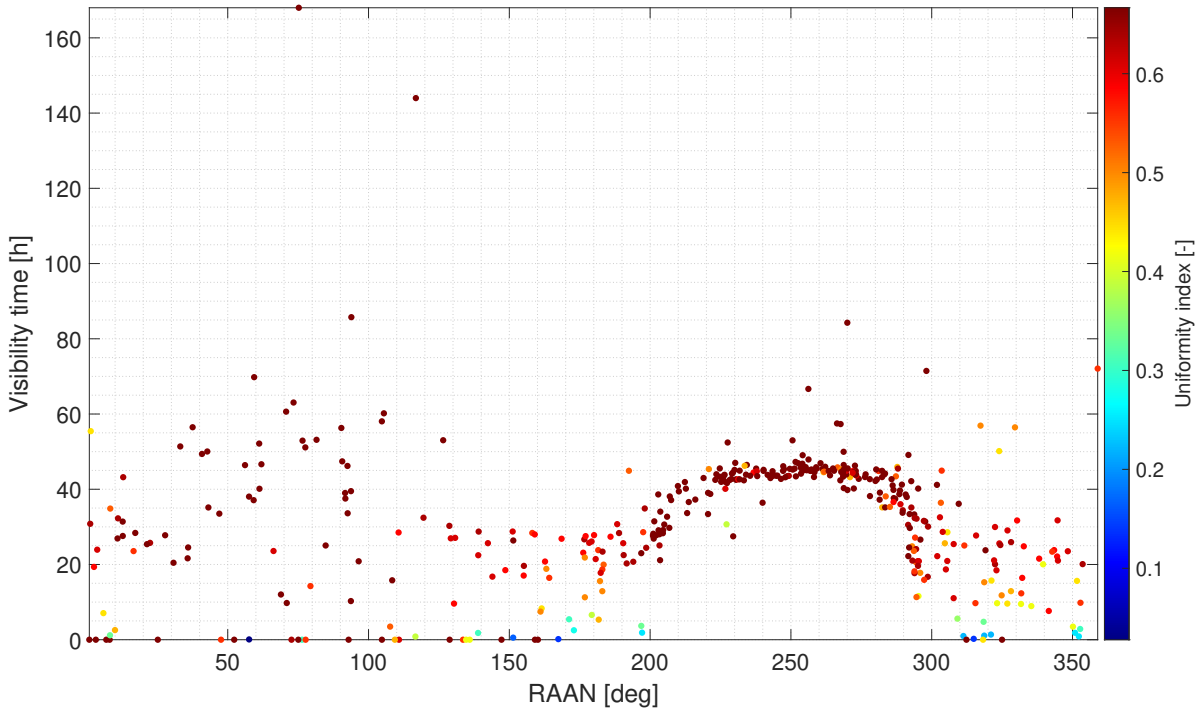

Figure 3.8: Total visibility time expressed in hours and RAAN as function of the uniformity index. Only the geometric constraint is applied

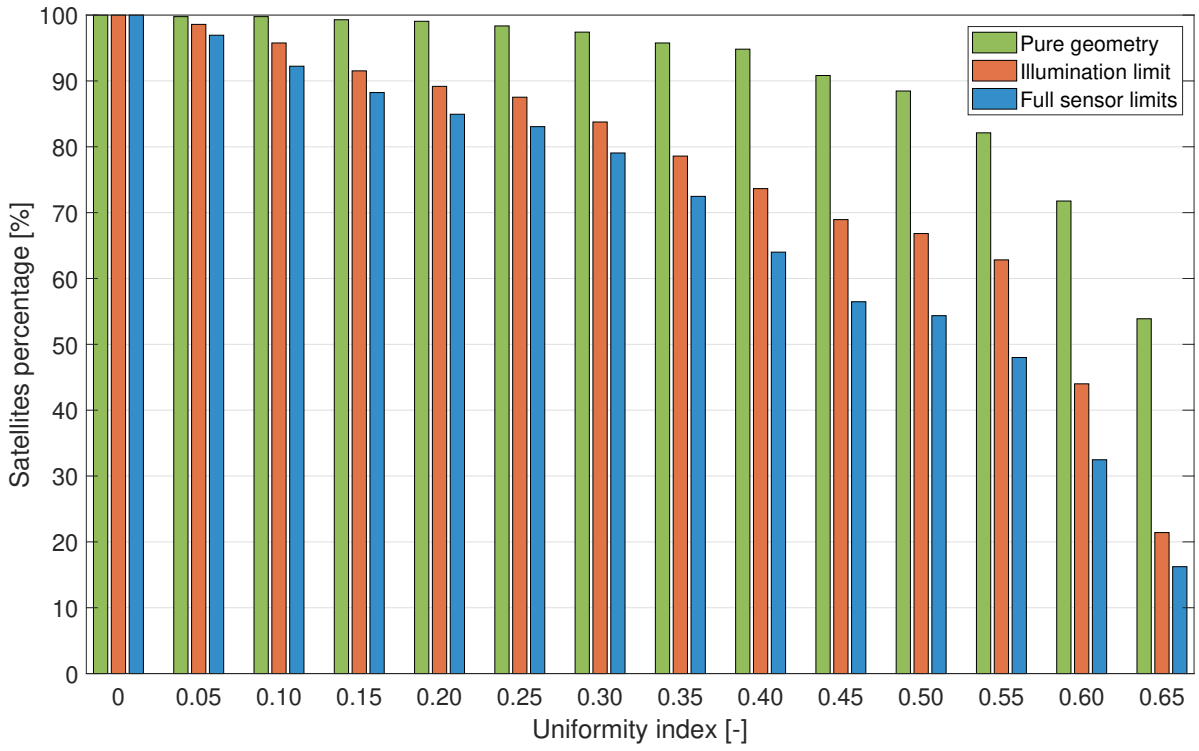

Figure 3.9: Uniformity index for three different sensor limits: pure geometry, only illumination and full sensor limits

Sun-synchronous orbit

A Sun-synchronous orbit (SSO) is one the most used orbits for Earth science missions. It is a near polar orbit where the nodal precession rate is matched to the Earth's mean orbital rate around the Sun. The resulting effect is a fixed orbit geometry with respect to the Sun, with approximately the same lighting condition along the ground track, such that the satellite passes over any given point of the Earth's surface at about the same local mean solar time [2]. Most of these satellites lie between 95 and 100 degrees of inclination, in Low Earth Orbit; from Figures 3.3 and 3.5 above, it is clear that they are the majority of objects for the considered catalogue. Therefore, it is important to seek for correlations with this particular region of space, being COSMO-SkyMed 4 part of this population.

The first Figure 3.10 shows the classic visibility windows, time and uniformity index as function of RAAN, the only keplerian parameter that truly differentiate SSO orbits.

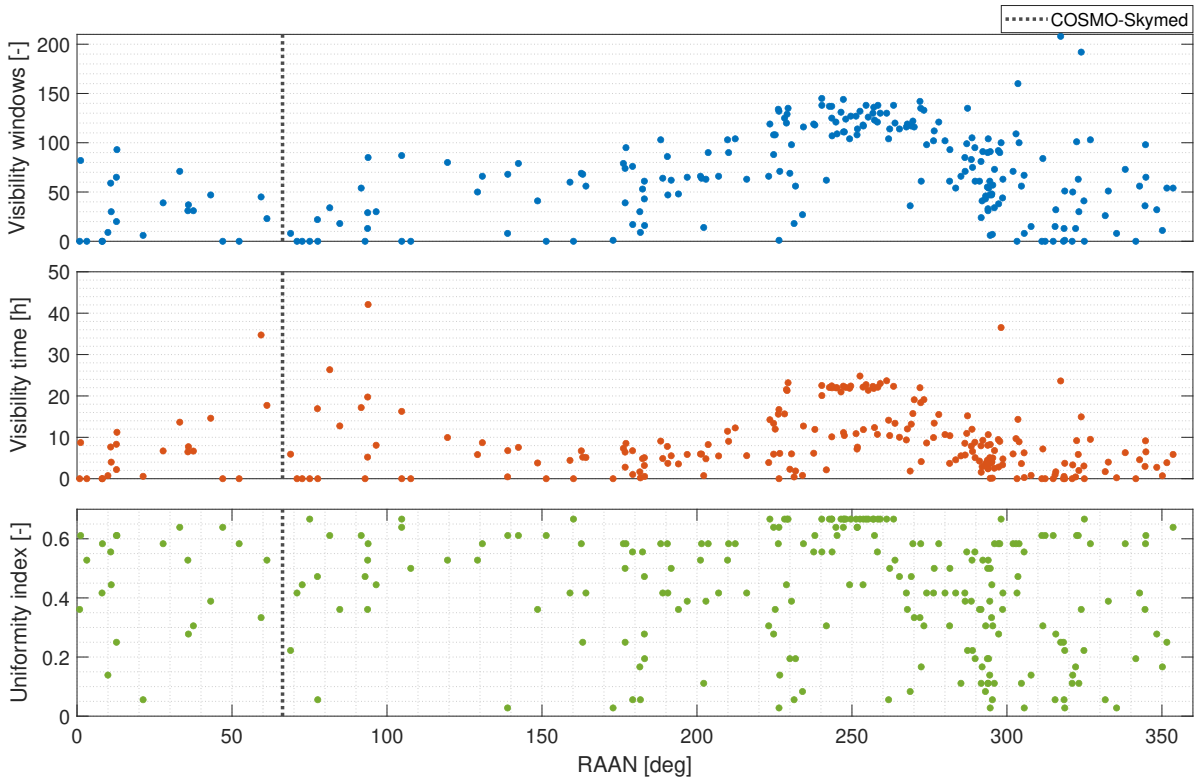

Figure 3.10: Total visibility windows, time and uniformity index as function of RAAN for objects in SSO. Only the geometric constraint is applied

Compared to the results of the complete catalogue, no significant difference is evident, with points following a similar trend to the one of Figures 3.3 and 3.5. Hence, an additional graph is shown in Figure 3.11, with the uniformity index distribution with respect to

non-SSO objects. Although very similar, there are slightly less Sun-synchronous satellites with high index values.

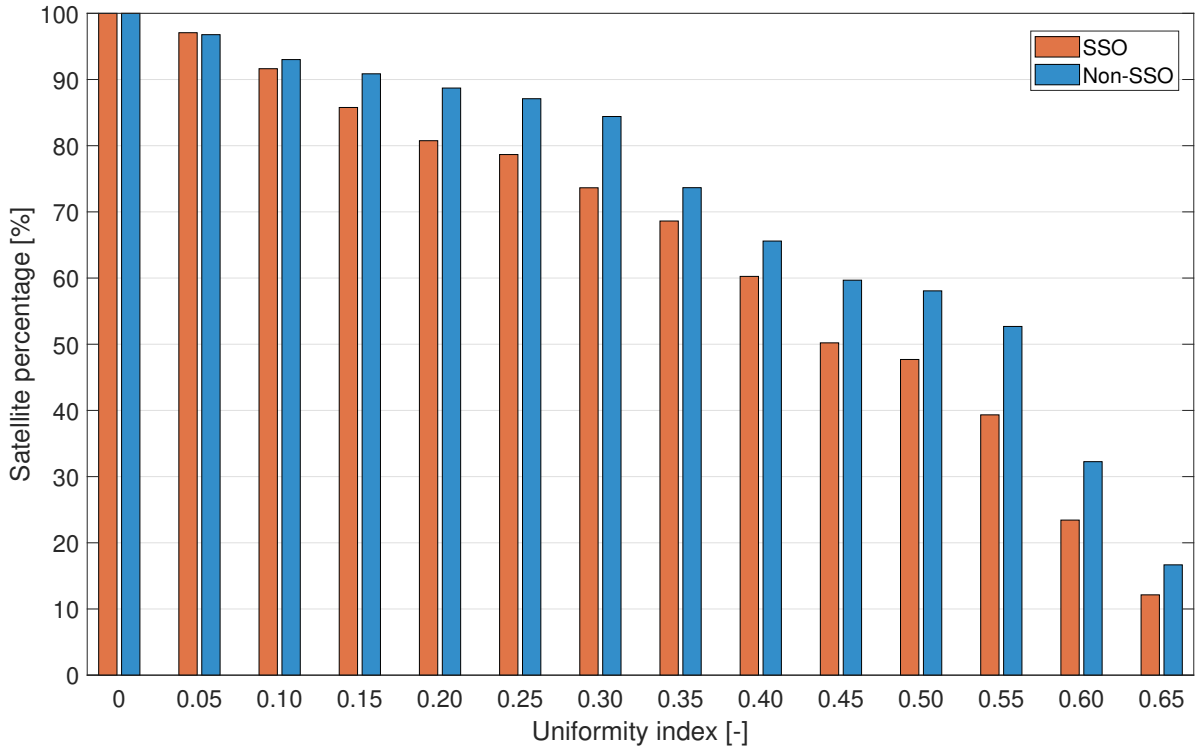

Figure 3.11: Distribution of uniformity index for SSO and non-SSO objects

Non-visible objects

From the figures above one thing is immediately glaring: some objects are never visible, even when no limits are considered. This deserves its own separate analysis, presented in Figure 3.12, where RAAN and inclination are plotted as function of the sensor limit considered. Here, the green diamonds indicate those objects not visible due to geometrical limitations; these satellites can't be seen independently of the type of sensor adopted. The red squares instead, refers to objects that are not visible due to Earth shadow, so objects that only optical sensors cannot see, regardless of the actual camera performance. Finally, the blue dots relates to those satellites not visible by the specific sensor used, that is, not visible due to the limiting magnitude being too low to actually see the satellite at any distance[5].

An important consideration comes once again from the distribution with respect to RAAN. Between 200 and 300 degrees all objects are actually visible, especially from

[5]Referring to Figure 3.2 this is true for all the objects smaller than 1 cm approximately.

a geometrical point of view, proving the importance of this orbital parameter in defining visibility performance. Concerning inclination, on the contrary, there seems to be no clear correlation, apart from the lack of objects with inclination below 50 degrees; however, this could simply result from a lower number of objects orbiting closer to the equator in the considered catalogue.

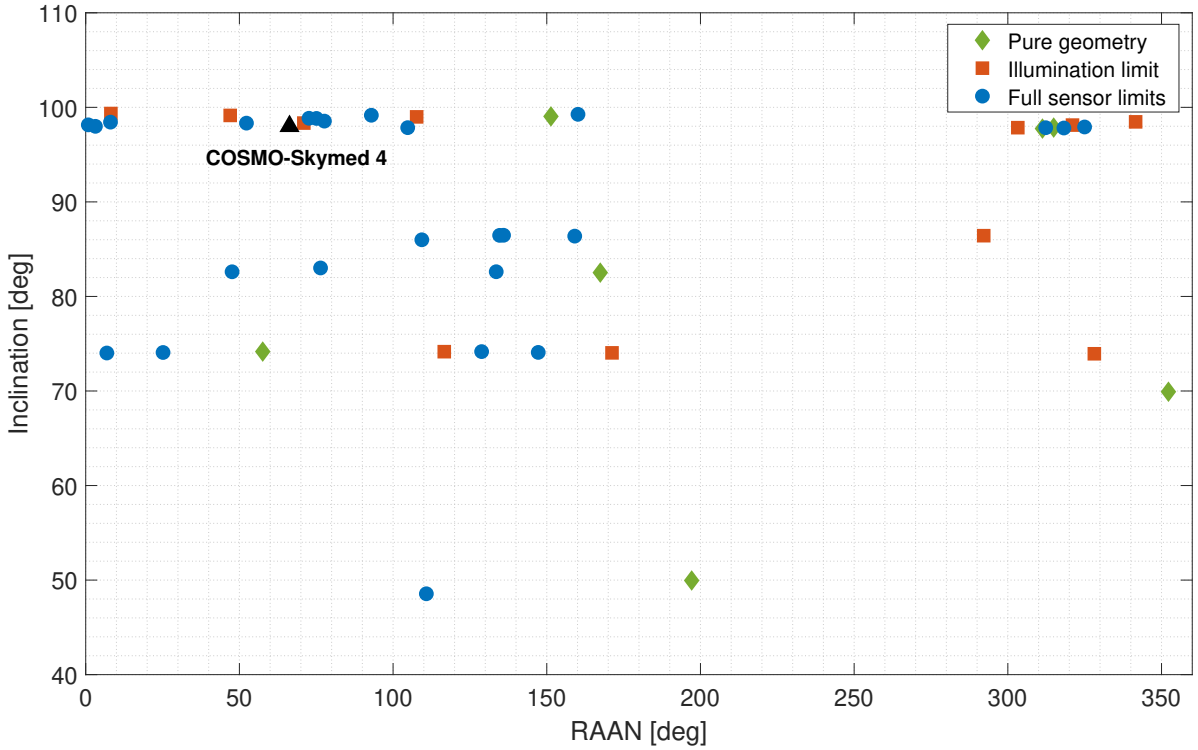

Figure 3.12: RAAN and inclination for non-visible objects with three limits: pure geometry, only illumination and full sensor limits

Out of 425 objects, 25 are never visible, 7 are visible only with radar sensors, while 11 can be seen by selecting a different and more powerful optical sensor.

Maximum visibility range

The maximum visibility range is important to determine the effectiveness of optical sensors with respect to radars. The latter are highly limited, especially for onboard low-power instruments, though they can measure directly the relative distance with high accuracy. Figure 3.13 shows the maximum range for the classic three sensor limits already analyzed before. As expected in this case, the illumination requirement is not particularly relevant and the reduction in the maximum range is determined mainly by the sensor limiting magnitude. For the case at study, even with the chosen camera, the range is still closer

to the geometrical limit, despite some smaller objects that can be seen only when closer than 5000 km. Nevertheless, an onboard radar would be limited to the lower part of the figure, especially with smaller Radar Cross Section targets [29]. Moreover, the geometrical maximum range is never lower than 6000 km (and possibly higher for high eccentricity orbits), thus an optical sensor allows to better optimize the visibility windows, with more time available for the measurement campaign.

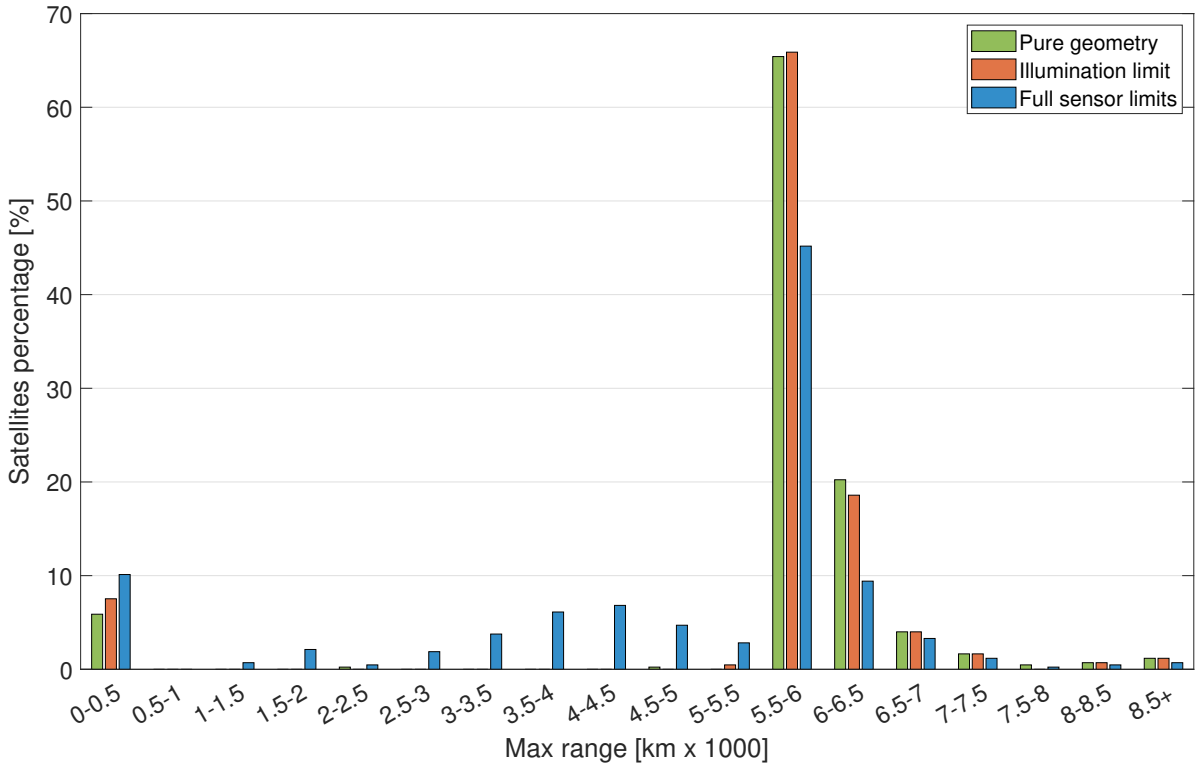

Figure 3.13: Maximum range with three limits: pure geometry, only illumination and full sensor limits

Revisit time

The last correlation analyzed concerns the time between two consecutive passages. As already mentioned above, the scheduling of observation is extremely important when dealing with multiple targets. Therefore, a faster revisit allows to pile up more measurements in less time and thus account additional time to the observation of other possible targets. The first graph, in Figure 3.14, highlights the minimum and maximum revisit time in logarithmic scale as function of RAAN, when only geometry is considered. The former is characterized by an interesting behaviour, which will be further analyzed later, in which objects with RAAN between 200 and 300 degrees have almost constant minimum revisit time, but sensibly higher than objects with RAAN between 0 and 100 degrees, where the

dots are more uniformly distributed in the given range. Similar considerations can be made on the maximum revisit time. Once again, objects with RAAN around 250 degrees seems to be confined in the lower part, with almost no dots above 3000 seconds.

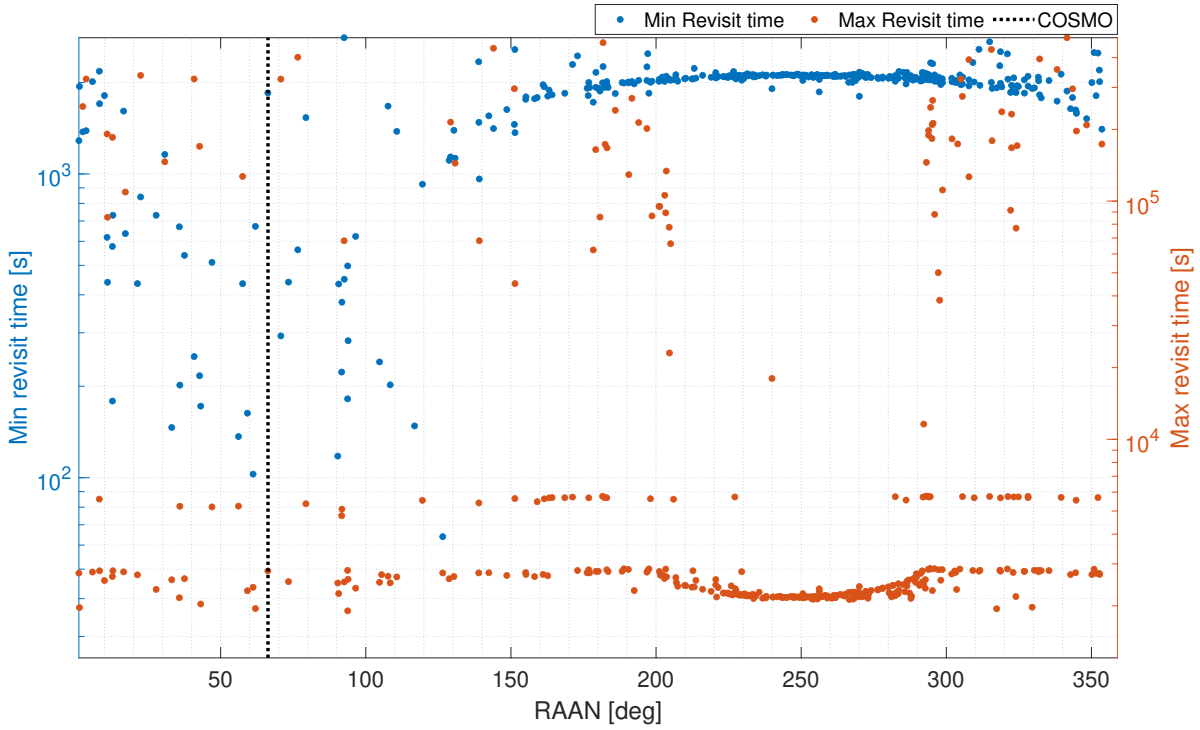

Figure 3.14: Maximum and minimum revisit time in logarithmic scale. Only the geometric constraint is applied

To better understand this behaviour, Figure 3.15 shows a magnification of the minimum and maximum revisit time between 0 and 3000 seconds. The correlation with RAAN is now clearly visible; the two values tend to coincide at about 250 degrees and 2100 seconds, while the blue dots are much closer to zero when RAAN is around the COSMO vertical line. On the contrary, the maximum time reaches a systematic minimum at 250 degrees, whereas for other RAAN it is more sparse, with values reaching more than 10^5 seconds, more than 1 day without observations.

These results are pictured in Figure 3.16, where the minimum revisit time is represented as function of RAAN and inclination, with a colorbar referred to the maximum time, in a scale between 2000 and 3000 seconds. As expected, the behaviour described before is completely independent on the inclination values, with the lowest maximum revisit again centered at 250 degrees RAAN.

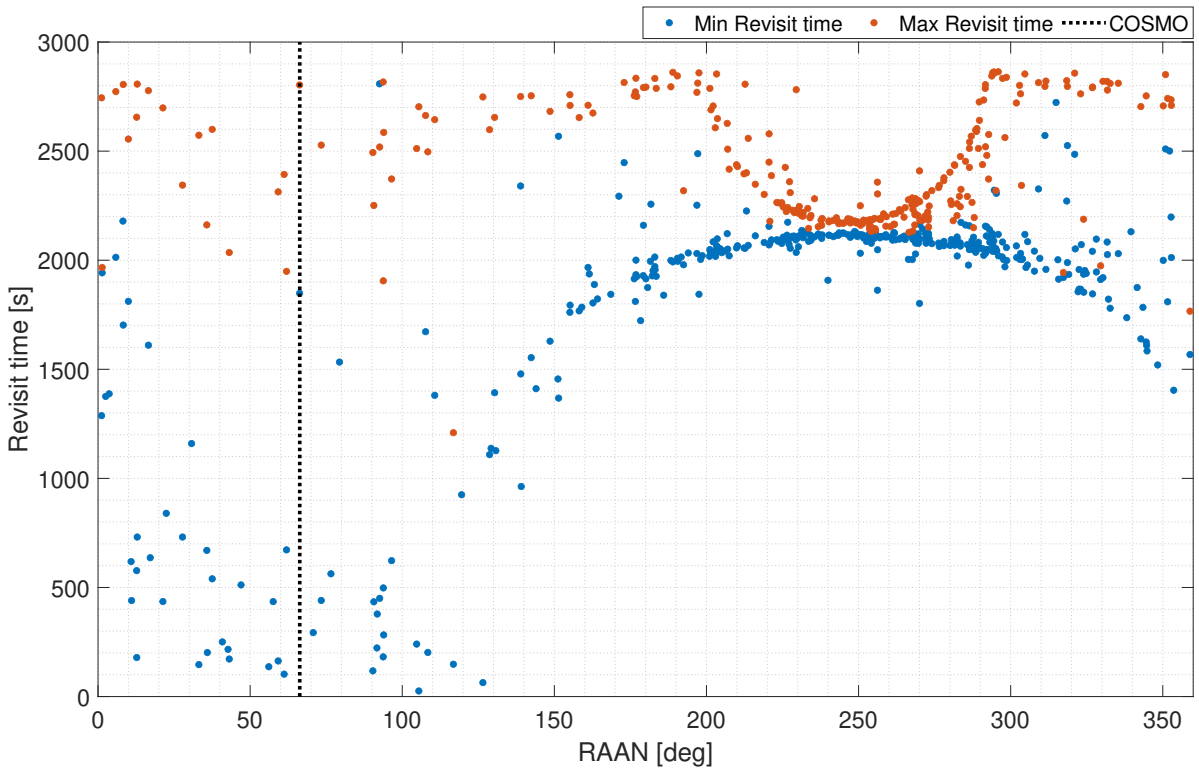

Figure 3.15: Maximum and minimum revisit time zoomed in. Only the geometric constraint is applied

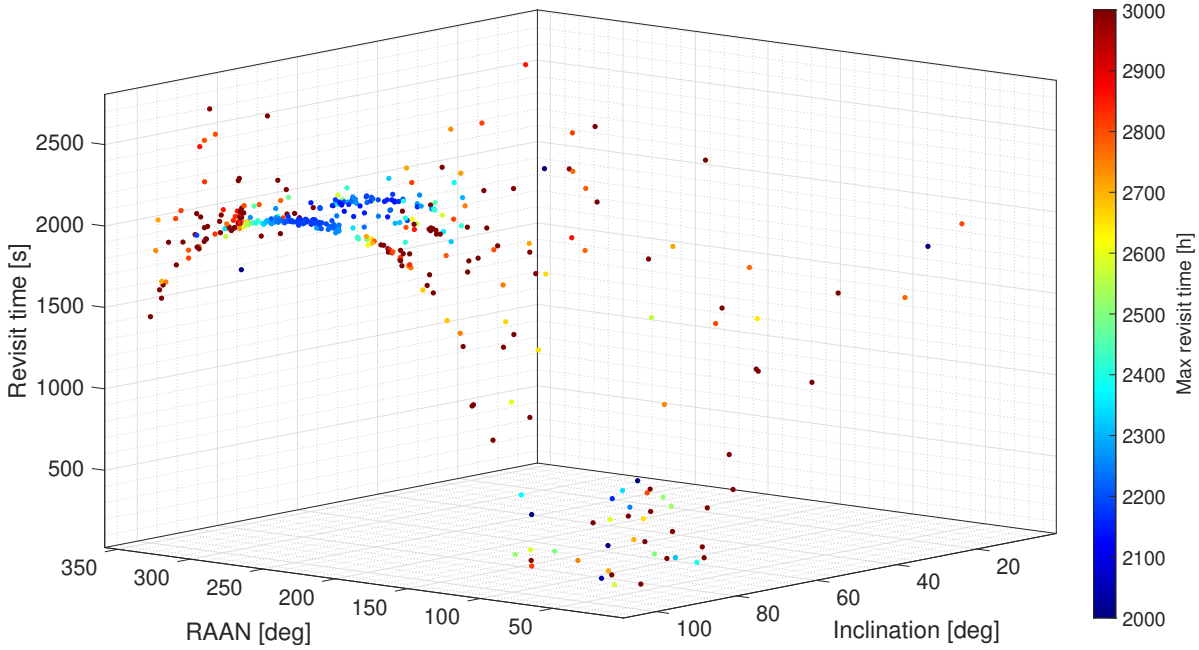

Figure 3.16: Minimum and maximum revisit time as function of RAAN and inclination. Only the geometric constraint is applied

Eventually, the mean revisit time distribution is pictured in Figure 3.17 for the three cases of pure geometry, only illumination and full sensor limits. In the first case, the majority of objects (about 60%) has an average of 2000-2500 seconds, with a 10% lower and the remaining distributed between 2500 and 7500 seconds. Since the selected catalogue contains mainly LEO objects, they are characterized by a period around 95-100 minutes, so below 6000 seconds; hence, it makes sense that the mean revisit time is centered at slightly before half a orbit, when only the geometrical constraint is considered. If the optical sensor limits are fully enforced, the time is shifted on the right part of the figure more or less uniformly between 2500 and 6000 seconds, with a peak at more than 7000. The result is similar when only the target illumination is required, suggesting that this last constraint is responsible for lack of visibility when the target is in the shadow cone, leading to an increase in mean time.

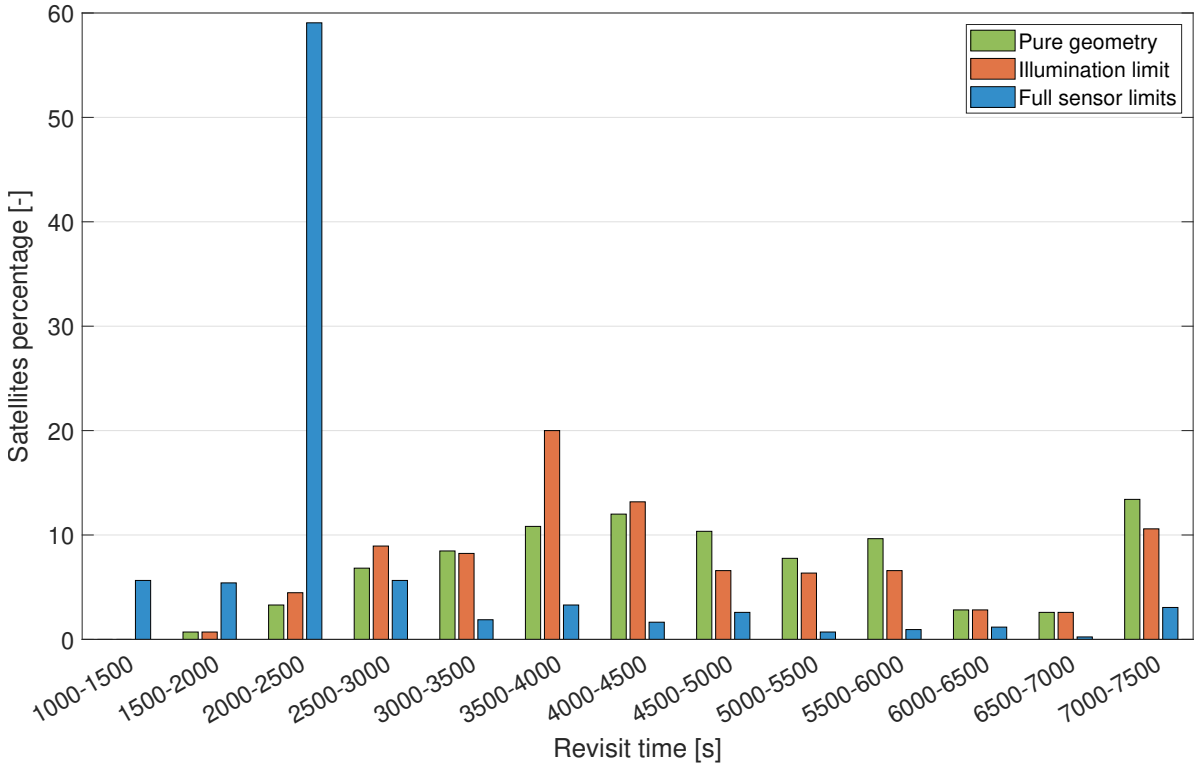

Figure 3.17: Mean revisit time with pure geometry, only illumination and full sensor limits

3.3. Overview

The results of the statistical analysis are here summarized in order to get an insight on the performance of the sensor used against the catalogue of potentially hazardous satellites. Both the visibility windows and the visibility time are strongly reduced by the

illumination requirement, while the limiting magnitude plays an important role only for extremely small objects, reducing the effective maximum range, but not the number of windows.

Concerning the keplerian parameters, no remarkable relations have been identified for inclination and argument of perigee. Greater semi-major axis may grant a lower number of windows and higher visibility time, yet a larger sample is required for a more significative inference. Right ascension of the ascending node is the only element showing interesting behaviour for the analyzed parameters, especially for values between 200 and 300 degrees:

- Higher number of visibility windows, close to the theoretical maximum
- Higher visibility time
- Higher uniformity index, at more than 0.6
- No unseen objects in the considered time window
- Higher minimum revisit time, confined around 2000 seconds
- Lower maximum revisit time, between 2000 and 3000 seconds

For the specific objects in Sun-Synchronous orbits, no significant trend is identified with respect to the general case, though there are fewer satellites with uniformity index above 0.55.

In the analyzed scenario, the influence of Sun separation seems to be negligible and limited to very few windows, likely due to the considered time window near the Autumn equinox and the asset orbit almost perpendicular to the Sun direction. In Figure 3.18 is highlighted the distribution of the angular distance between Sun-sensor and sensor-target vectors at the beginning of each visibility window for each satellite. According to the inertial definition of the camera frame, if the value is greater than the required 30°, the satellite is visible over the entire field of view. Only a limited number of potential observation opportunities are hindered by this specific limitation.

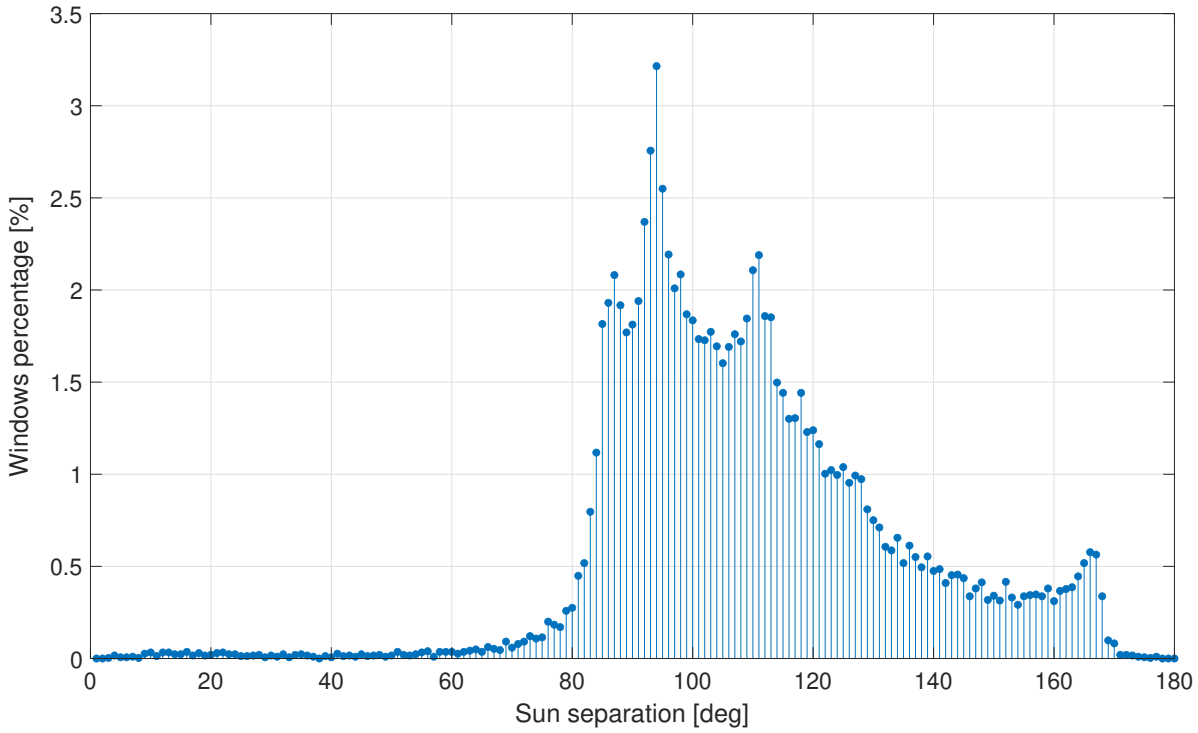

Figure 3.18: Distribution of Sun separation at the beginning of each window for all the catalogued satellites.

Finally, it is important to linger on the maximum values of the uniformity index, never above 0.67. Regardless of the type of sensor, the limits considered and the target under consideration, the observations cover at most about two-thirds of the asset's orbit. The reason probably lies in the very nature of satellites relative motion in the specific simulated scenario; that said, it is possible that a longer time window could lead to an increase in this index.

4 | Methodology

In this chapter the methodology adopted for the second part of the simulation is presented, while the results of the relative orbit determination and conjunction analysis are shown in *Chapter* 5. Firstly, the minima research is described in Section 4.1, in order to identify the targets with a close conjunction, determined by a minimum distance below 5 km. Consequently, the reference trajectory propagation and selected filtering technique are shown and compared to a ground-based analysis, developed to validate the onboard computation. The orbit determination process described here is typically called *refined* (so, *ROD*), as the input of the filter is the output of an already performed *initial* OD (or *IOD*), where the state and covariance at epoch t_0 are computed without any a priori information, using only the available measurements. As in Figure 4.1, the result of an IOD is in general not sufficiently accurate to analyze a conjunction, and ROD is thus needed to increase estimation accuracy, compute probability of collision and asses the need to perform a collision avoidance manoeuvre.

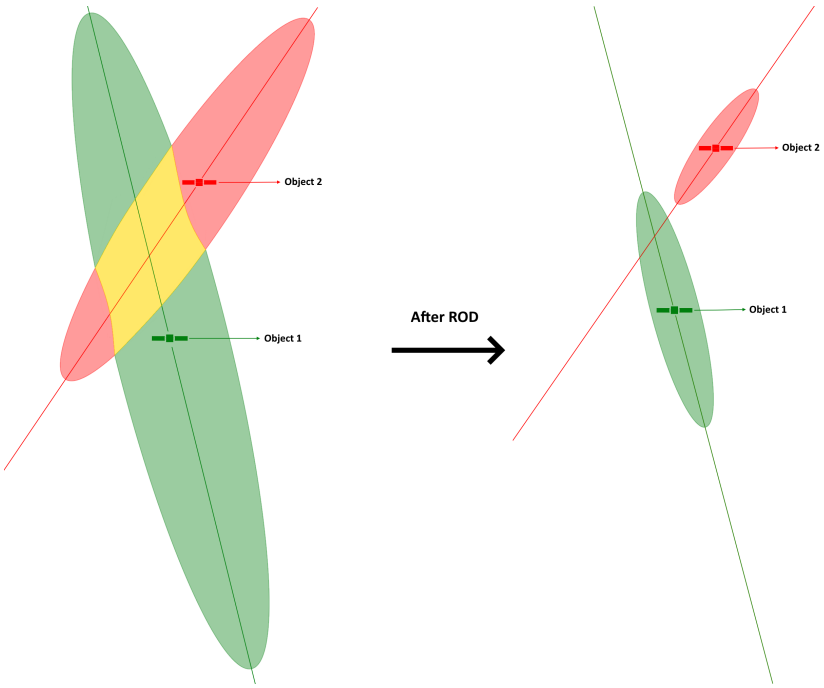

Figure 4.1: Conjunction event, example of IOD (left) and ROD (right) results comparison

4.1. Simulation time and minima research

The conjunction events are searched in the 8 days after the statistical analysis, from the 8^{th} to the 16^{th} September 2022. As specified in *Chapter 3*, the SOPAC library makes use of SGP4 to propagate objects trajectories and TLEs must be provided. However, these are typically accurate up to a 7-day computation and thus they require frequent update for a realistic analysis. For this reason, the minima research is performed by updating the TLEs every two days, such that at least one set is retrieved for each satellite and the propagation is kept under a week. Moreover, due to the high relative velocities, the distance must be refined through a minimization process to find the effective TCA. During a conjunction, the relative radial velocity reaches zero at the corresponding minimum, thus a root finding can be adopted to validate the result of the relative range minimization, with the corresponding expressions in Equation (4.1). The algorithm is implemented directly in Python, exploiting *scipy* libraries *minimize* and *root scalar*.

$$\begin{cases} \rho(t) = \|\boldsymbol{r}_2 - \boldsymbol{r}_1\| \\ \Delta v_r(t) = \dfrac{(\boldsymbol{r}_2 - \boldsymbol{r}_1) \cdot (\boldsymbol{v}_2 - \boldsymbol{v}_1)}{\rho} \end{cases} \tag{4.1}$$

Overall, in the analyzed time window, six conjunctions are identified and summarized in Table 4.1. The closest encounter occurs during the first sub-window with a Falcon 1 upper stage launched in 2009, with a minimum distance of less than 1 km. Once the objects requiring a conjunction analysis are identified, measurements can be properly simulated as described in the next section.

Object	**NORAD ID**	**Launch date**	**Time window**	**TCA**	**Distance** $[km]$
Elektron 1	00746	01-1964	08/09 - 10/09	09/09 13:29	2.75
Falcon 1 (r/b)	35579	07-2009	08/09 - 10/09	09/09 20:05	0.88
Fengyun 1C (deb)	31540	05-1999	10/09 - 12/09	10/09 03:51	2.85
Cosmos 1408 (deb)	50457	09-1982	12/09 - 14/09	13/09 04:41	4.69
Fengyun 1C (deb)	29866	05-1999	14/09 - 16/09	14/09 01:13	4.21
Cosmos 2252 (deb)	33804	06-1993	14/09 - 16/09	14/09 06:45	4.89

Table 4.1: Identified nominal conjunction events. Acronyms *r/b* and *deb* refers respectively to *rocket body* and *debris*.

4.1.1. Measurement simulation

Observations are taken for each object since the TLE epoch up to the day before the conjunction, so that time can be set aside for computation and scheduling of a potential collision avoidance manoeuvre. The optical sensor provides right ascension and declination every 60 seconds, obtained through SPICE's *recrad*[1], to which is summed a Gaussian noise of zero mean and variance given by the sensor accuracy squared. For a ground-based telescope, this can be as low as 1/2 arcseconds, or 0.00028°; considering the lower performance of an onboard optical camera in terms of sensor dimensions and computational power, along with possible mounting errors, the angular accuracy is set at 0.01 degrees for both measurements.

Hence, Equation (4.2) presents the model upon which the simulation of real observations is predicated.

$$\begin{cases} \alpha = \alpha^* + \eta_\alpha, \quad \text{with} \quad \eta_\alpha \sim (0, 0.01^2) \\ \delta = \delta^* + \eta_\delta, \quad \text{with} \quad \eta_\delta \sim (0, 0.01^2) \end{cases} \tag{4.2}$$

with α^* and δ^* the nominal values and η_i the error Gaussian distributions. No cross-correlations are considered and the observation error matrix is diagonal, as given by Equation 4.3.

$$R = \begin{bmatrix} 0.01^2 & 0 \\ 0 & 0.01^2 \end{bmatrix} \tag{4.3}$$

4.2. Nominal trajectory computation

Once the dangerous targets are identified and measurements are correctly simulated, the main variables are exported to *MATLAB®* for the OD and conjunction analysis. The adopted filtering technique has already been described in *Chapter* 2 and it is based on the linear minimum variance Least Squares, analytically solved with a single iteration to reduce computational time; therefore, it is firstly necessary to compute the reference trajectory with respect to which the deviations obtained with the filtering process are calculated. It is important that the reference is close enough to the real motion as too large errors may lead to biased outputs, especially when considering a linear navigation problem. The most significant perturbation for a LEO object results from the fact the Earth is not perfectly spherical. The main contribution to the non-sphericity gravity field comes from Earth oblateness, that is, the difference in radius between the equator and the

[1] *recrad* allows to convert rectangular positional coordinates in right ascension, declination and range, as defined in Section 2.1.1. The latter is clearly discarded as not obtainable with an optical sensor.

poles. This perturbation is often called *J2* and a propagator including this effect alone greatly improve the accuracy of the OD with respect to a simple keplerian motion [20]. As shown in Figure 4.2, for a 600 km orbit, the other relevant perturbations are still due to non-spherical effects (*J3, J4* and *J5*); Lunar and Solar gravity fields, Solar Radiation Pressure (SRP) and drag all have a significant smaller impact.

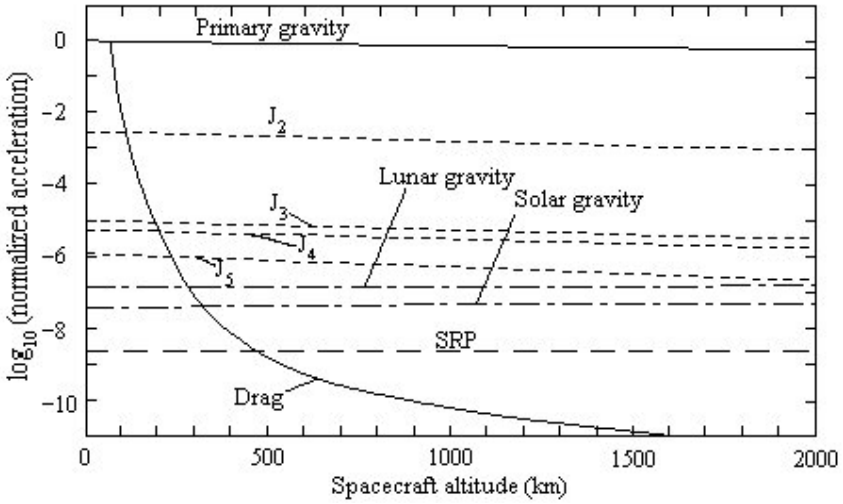

Figure 4.2: Comparison of different disturbing accelerations in LEO [22]

The components of the J2 acceleration can be expressed directly in ECI reference frame, as in Equation (4.4).

$$\begin{cases} f_x = -\dfrac{\mu x}{r^3} J_2 \dfrac{3}{2} \left(\dfrac{R_E}{r}\right)^2 \left(5\dfrac{z^2}{r^2} - 1\right) \\ f_y = -\dfrac{\mu y}{r^3} J_2 \dfrac{3}{2} \left(\dfrac{R_E}{r}\right)^2 \left(5\dfrac{z^2}{r^2} - 1\right) \\ f_z = -\dfrac{\mu z}{r^3} J_2 \dfrac{3}{2} \left(3 - 5\dfrac{z^2}{r^2}\right) \end{cases} \tag{4.4}$$

In particular, matrix $\tilde{H}$ is calculated using the relative position, which is strongly influenced by the adopted model; indeed, considering a simple J2 propagation is often not sufficient as the relative state error becomes non-negligible in longer simulations, as highlighted in Figure 4.3 for the first conjunction event, involving Elektron 1 satellite. However, a high fidelity propagator is also much more computationally demanding, which is particularly relevant for onboard calculations. Hence, the best compromise is found by propagating directly from the TLEs using SGP4. This solution grants lower computational time and sufficient accuracy for the considered time window [30, 35]; a more

comprehensive description of satellite dynamics is provided in Appendix B. The relative motion is thus given by the difference between primary and secondary states and the consequent relative measurements can be computed also for the nominal trajectories.

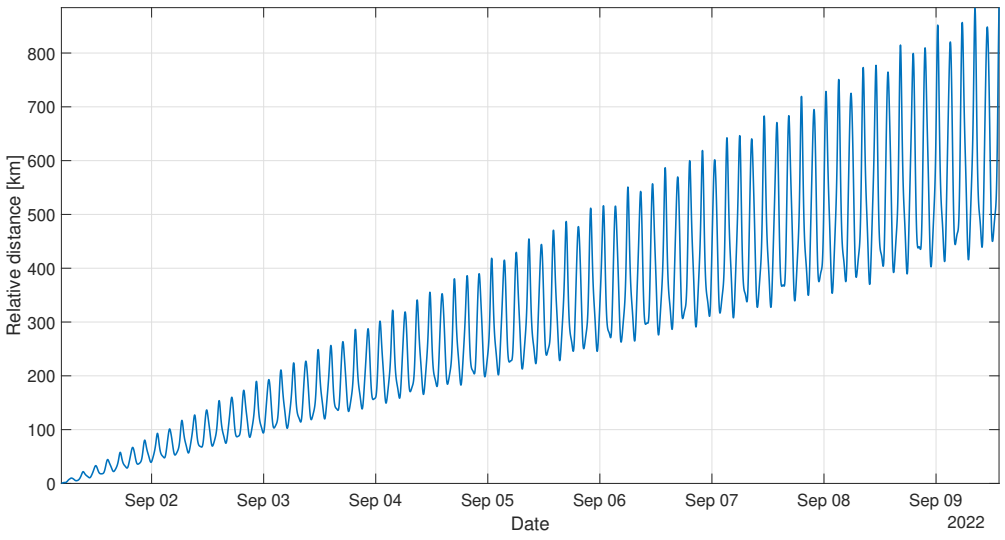

Figure 4.3: Relative position error between SGP4 and J2 propagations for COSMO-SkyMed 4 and Elektron 1 satellites

Considering the selected filtering method, it is necessary to derive as well the State Transition Matrix for each observation, for both satellites: the primary STM is indeed required for the consider covariance analysis, as shown in the next section. STM also requires certain accuracy to correctly map the state at TCA to the observational epoch. Nonetheless, it is much less sensitive to simplified dynamical models and only J2 perturbation can be included without excessively diminishing the estimation accuracy, while keeping a low computational cost. The STM is computed with the variational approach described in Section 2.1.3 and the expression of the jacobian matrix is obtained through symbolic manipulator, to integrate a more accurate, analytical equation.

The B-plane is defined with the reference states at the nominal TCA. This is also the main drawback of the solution presented in this thesis: it is not possible to determine the real epoch of conjunction as typically done with a sequential filter. Indeed, the Least Square presented in the next section compute the expected target state at the reference TCA, which must be known with a sufficiently high accuracy.

4.3. Onboard relative orbit determination

The relative nominal trajectory described above allows to compute the relative measurements and the corresponding deviations with respect to the real ones, imported from Python. The main idea behind the proposed method is based on the property of the STM to map the state at each observational instant, to the state at TCA. In this way, orbit determination can be made directly at the time of conjunction, without the need to propagate the results, which would cause an increase in the estimation error and computational time. The strongest assumption concerns the perfect knowledge of the state of the asset at each measurement epoch and equal to the reference trajectory. This allows to make an important consideration: the relative state deviations are equal to the target absolute state deviations. As a direct consequence, it is possible to map the measurements and relative positions directly with the target state transition matrix, greatly simplifying the computation. The concept can be visualized in Figure 4.4.

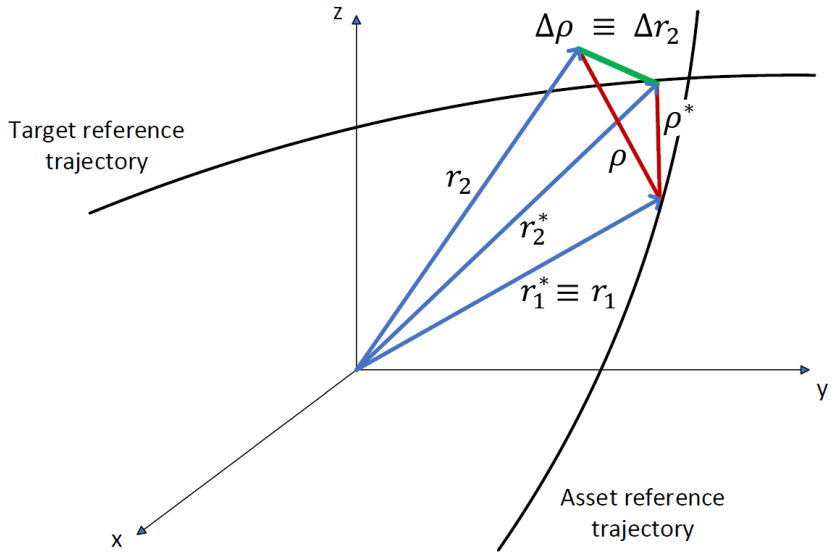

Figure 4.4: Relative and absolute state deviations at TCA, identified respectively by ρ and r_i. Subscripts 1 and 2 refer to primary and secondary objects, while the *star* apex refers to the reference absolute and relative position vectors.

Defining $\boldsymbol{s}$ the relative state, and recalling Equation (2.6):

$$\delta \boldsymbol{y}_i = \tilde{H}_i(\boldsymbol{s}_i^*)\delta \boldsymbol{s}_i + \boldsymbol{\epsilon}_i, \quad \text{with} \quad i = 1, ..., l \tag{4.5}$$

where the vector $\boldsymbol{s}^*$ refers to the quantity evaluated on the nominal trajectory. As de-

scribed in Chapter 2, the measurements are then related to the deviation at a specified epoch (the conjunction epoch), as shown in Equation (4.6).

$$\delta \boldsymbol{y} = \tilde{H} \Phi_t(t_{TCA}, t) \delta \boldsymbol{s}_{TCA} + \boldsymbol{\epsilon} \tag{4.6}$$

Φ_t is the target STM, computed as described in the previous section whilst, based on the assumption of perfectly known asset motion, $\delta \boldsymbol{s}_{TCA}$ can be substituted by $\delta \boldsymbol{x}_{TCA}$, the target absolute state deviation.

The implementation requires the linearization of the observational model along the nominal motion; Equation (4.7) shows the expression of right ascension and declination for a general space-based sensor in an inertial reference frame [21].

$$\begin{cases} \alpha = \tan^{-1}\left(\dfrac{y_t - y}{x_t - x}\right) \\ \delta = \tan^{-1}\left(\dfrac{z_t - z}{\sqrt{(x_t - x)^2 + (y_t - y)^2}}\right) \end{cases} \tag{4.7}$$

where (x, y, z) refer to the components of the asset spacecraft, while (x_t, y_t, z_t) to the considered target. Calling (s_1, s_2, s_3) the component of the relative position vector in the same inertial frame , it is possible to derive the above equations and compute the matrix $\tilde{H}$, as expressed in Equation (4.8).

$$\tilde{H} = \left[\frac{\partial G}{\partial \boldsymbol{X}}\right]_i^* = \begin{bmatrix} \frac{\partial \alpha}{\partial s_1} & \frac{\partial \alpha}{\partial s_2} & \frac{\partial \alpha}{\partial s_3} & 0 & 0 & 0 \\ \frac{\partial \delta}{\partial s_1} & \frac{\partial \delta}{\partial s_2} & \frac{\partial \delta}{\partial s_3} & 0 & 0 & 0 \end{bmatrix} = \begin{bmatrix} -\frac{s_2}{s_{xy}^2} & \frac{s_1}{s_{xy}^2} & 0 & 0 & 0 & 0 \\ -\frac{s_1 s_3}{s_{xy} s^2} & -\frac{s_2 s_3}{s_{xy} s^2} & \frac{s_{xy}}{s^2} & 0 & 0 & 0 \end{bmatrix} \tag{4.8}$$

where $s_{xy}^2 = s_1^2 + s_2^2$ and $s^2 = s_1^2 + s_2^2 + s_3^2$.

$\tilde{H}$ is function directly of the relative position and thus it is identical for both the primary and the secondary objects.

Overall, the product between $\tilde{H}$ and the STM is the matrix H that maps each measurement to the target state at the conjunction. The asset spacecraft can be tracked by ground-based stations to provide accurate orbit determination at any desired epoch. However, its motion is still affected by uncertainties, which must be included in the Least Square result. Therefore, the idea is to exploit the concept of consider covariance analysis to obtain a greater target covariance that embeds the primary spacecraft uncertainty.

4.3.1. Application of the consider covariance analysis

The theoretical concepts and the resulting algorithm of the CCA have been already introduced in Chapter 2. For the specific case at study, the consider parameter is the primary spacecraft state deviation at the time of closest approach, with its a priori value set to zero[2]. Similarly, the matrix $\bar{P}_{cc}$ is the a priori covariance, expressed in terms of standard deviations in the UVW reference frame in Equation (4.9); the considered values are especially small as the primary spacecraft motion is assumed to be constantly updated by accurate ground sensors.

$$\begin{cases} \sigma_r = [10, 30, 10] \ \ [m] \\ \sigma_v = [0.5, 2, 0.2] \ \ [m/s] \end{cases} \tag{4.9}$$

To properly exploit the CCA it is necessary to compute matrix H also for the asset satellite, as the product between $\tilde{H}$ (equal for both objects) and the primary STM, computed with a simple J2 effect. The end results are made explicit in Equation (4.10) for the target state deviation and covariance at TCA.

$$\begin{cases} \delta\hat{\boldsymbol{x}}_{CCA} = \delta\hat{\boldsymbol{x}} \\ P_{x_{CCA}} = P_x + S_{xc}\bar{P}_{cc}S_{xc} \end{cases} \tag{4.10}$$

with S_{xc} as defined in Algorithm 2.2, where $H_x = \tilde{H}\Phi_x$ for the target and $H_c = \tilde{H}\Phi_c$ for the asset. If the a priori primary state deviation is set to zero, the neglected uncertainties influence only the covariance, which is given by the summation of two semi-definite matrices. Hence, the output of the CCA is a greater target covariance, with unchanged deviation from the reference trajectory.

With the estimated target state and covariance at the minimum distance epoch, it is now possible to analyze the conjunction in the B-plane, in terms of probability of collision.

[2]This is equal to saying that the expected value of the a priori state, given by a ground-based IOD, is the nominal one. The results shown are still valid for the generic case of $\bar{\boldsymbol{c}} \neq 0$

4.3.2. Conjunction analysis

Firstly, the absolute target state is computed by adding to the nominal value the result of the OD filter, as reported in Equation (4.11).

$$\hat{\boldsymbol{x}} = \boldsymbol{x}^* + \delta\hat{\boldsymbol{x}} \tag{4.11}$$

The B-plane is defined from the reference trajectory according to Equation (2.53). The positional components of the primary and secondary covariances and the relative state are projected onto the newly defined bi-dimensional frame, in order to apply the simplified equation for the probability of collision (see Equation (2.61)). From Section 2.2.2 it is necessary to compute the combined covariance C as the summation of the two objects covariances, already projected onto the B-plane, as seen from Equations (4.12) and (4.13). As already mentioned, the primary covariance at TCA is not estimated directly onboard and is provided by a ground-based OD, performed with a UKF and described in the next section.

$$C = P_{x_{CCA_{b,2D}}} + P_{cc_{b,2D}} \tag{4.12}$$

Here P_{cc} is the asset covariance. The subscript $b, 2D$ refers to the quantity expressed in B-plane coordinates; defining $R_{b,2D}$ the bi-dimensional rotation matrix, it is possible to project both the covariances and the state, as follow:

$$\begin{cases} \hat{\boldsymbol{x}}_{b,2D} = R_{b,2D}\hat{\boldsymbol{x}} \\ P_{i_{b,2D}} = R_{b,2D} P_i R_{b,2D}^T \end{cases} \tag{4.13}$$

Finally, a hard-body radius of ten meters is considered to be sufficiently conservative to compute the approximated collision probability truncated to the third order, as shown in Equation (2.61)[3].

4.4. Ground-based analysis

A ground-based ROD and conjunction analysis is needed only for validation purposes, so the results can be compared with the onboard counterpart to verify performance, differences and drawbacks of both solutions. For this reason, SOPAC is not used for passages computation and a simple geometrical constraint is enforced; the filter is initialized with

[3]Remembering that the hard-body radius is the summation of the approximated spherical satellites radii.

the covariance of Equation (4.9) and state equal to the reference.

The implemented ground stations, two radars (*S3TSR* and *MFDR*) and one optical (*Cassini*), are part of the EU SST sensor network (EU Space Surveillance and Tracking) and located in Spain and Italy [10]. Both S3TSR (Spanish Space Surveillance and Tracking Radar) and MFDR (Multi-Frequency Radar Doppler) are monostatic sensors for tracking and ranging of LEO objects; Cassini is a 152 cm telescope located in Italy for satellites up to MEO and GEO orbits [13, 32]. The main characteristics are available in Table 4.2 and for visibility computation, a minimum elevation of 20 degrees is considered.

	S3TSR	**MFDR**	**Cassini**
Latitude	$37°09'59"N$	$39°38'30"N$	$44°15'33"N$
Longitude	$5°35'28"W$	$9°38'27"E$	$11°20'04"E$
Altitude $[km]$	0.142	0.259	0.780
Range accuracy $[m]$	30	50	-
Angular accuracy	0.5°	1°	2"

Table 4.2: Ground-based sensor network performance and characteristics

Real measurements are thus simulated by propagating with SGP4, to have comparable results with the space-based analysis. The orbit determination algorithm is based on the sequential filter UKF, providing absolute state and covariance at each observation epoch; this allows to have a real-time estimation which can be propagated to the computed TCA. In particular, since both objects are tracked and processed, it is possible to compute the best estimate of the conjunction epoch, which is generally slightly different than the nominal one.

Both the filter and the consequent state and covariance propagation are based on the Unscented Transform, with the following parameters derived from [11]:

- $10^{-4} \leq \alpha \geq 1$
- $\beta = 2$
- $k = 0$

where α is set at 10^{-2} and β is generally two if a normal distribution of sigma points is considered.

Finally, similarly to the space-based analysis, the dynamical model must be accurate

enough to provide smaller covariance and avoid possible divergent behaviour. However, since the reality simulation is based on SGP4, implementing a high fidelity orbit propagator may lead to a wrong minimum distance and conjunction epoch, due to neglected perturbations in SGP4 itself, possibly invalidating the comparison with the onboard analysis. Therefore, the model has been tuned to produce similar results to the reference, though a deviation is inevitable and higher accuracy is certainly achievable in a real case scenario (at the expense of an even higher computational cost). The propagator consisted of a degree-two, order-two geopotential model with Sun and Moon gravitational effects, Solar Radiation Pressure and drag. For the asset spacecraft the mass is set at 1000 kg, with five squared meters of effective area for both SRP and drag, while the respective coefficients are equal to 1 and 2.2. The conjunction analysis is performed for the two objects with the lowest minimum distance, where the propagation model is based on the same perturbations with area and mass modified accordingly, keeping the same coefficients: 2.7 m^2 and 3 m^2 for cross section, 300 kg and 500 kg for mass.

The dynamics inaccuracies require the addition of process noise as described in Section 2.1.5. In general, process noise is defined at each filter step, though a constant value is used in the algorithm as more accurate solutions are beyond the purpose of this research, as detailed in Equation (4.14). Moreover, due to model and SGP4 discrepancies, both the error and covariance are not further propagated to the TCA as it would inevitably produce larger deviations; hence, the results of the OD should actually be slightly worse when compared to the Least Square solution. The primary spacecraft uncertainty at TCA is considered equal to the value of the last measurement epoch.

$$Q = \left[(2)^2, (2)^2, (2)^2, (0.01)^2, (0.01)^2, (0.01)^2\right] [m^2, m^2/s^2] \tag{4.14}$$

5 | Simulation results

The results of the relative orbit determination and conjunction analysis are presented in this Chapter for the two closest conjunction events, involving *Elektron 1* and *Falcon 1* rocket body. In Section 5.1 the results are shown in terms of covariance and error with respect to the nominal trajectory, and compared to the ones obtained from a more accurate ground-based analysis in Seciton 5.2 and 5.3.

5.1. Onboard analysis

The objective of the refined relative orbit determination implemented and described in the previous chapter is to more accurately determine the position of a target satellite at the time of closest approach, with the smallest possible error with respect to the reference trajectory and the smallest covariance matrix. Indeed, the output of an IOD would be a non-negligible probability of collision, requiring further observations to actually determine the possible hazard posed by the considered target object. Therefore, the expected results from the proposed method would be a strong uncertainty reduction and a probability closer to zero, with the filtered minimum distance much greater than the computed covariance.

5.1.1. Elektron 1 conjunction

Elektron 1 was part of the first multiple satellite program developed by the Soviet Union since 1964. The main objective of the four satellites was the study of lower and upper *Van Allen* radiation belts and their orbit was thus highly eccentric. The spacecraft has a mass of about 329 kilograms, with a diameter of 3.25 meters and was launched on January 30, 1964, with an initial orbit between 406 km and 7110 km and inclination of 61 degrees. Of the four satellites, only Elektron 1 and Elektron 3 are still in orbit to date [28]; their main structure is pictured in Figure 5.1.

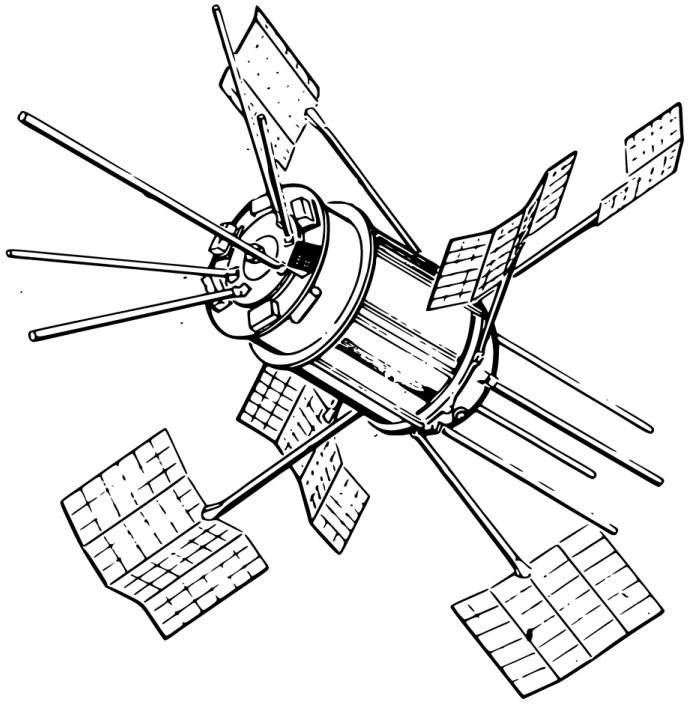

Figure 5.1: Elektron 1 satellite. *Credits: Wikipedia Commons*

From the statistical analysis of *Chapter* 3, the most important orbit parameter is the longitude of the ascending node, or RAAN. Since the satellite is no more operative, its orbit is constantly drifting and the results shown are referred to the first ten days of September 2022. From the TLE of the 2^{nd} of September, Elektron 1 RAAN was about 256 degrees, right in the middle of the high visibility range analyzed before. Indeed, with 122 available windows, a total visibility time of 47 hours and 0.67 uniformity index, it is one the most visible objects of the considered catalogue. Moreover, given the large radar cross section of 2.7 squared meters, the specific sensor does not influence the visibility; removing the illumination requirement, instead, the number of windows and the total time increase to 167 and 67 hours. Furthermore, given the RAAN value, the geometric revisit time oscillates between 1800 and 2400 seconds, with the maximum reaching 5800 when optical sensor limits are enforced; still, this performance greatly simplify object measurements scheduling, resulting in 786 available observations.

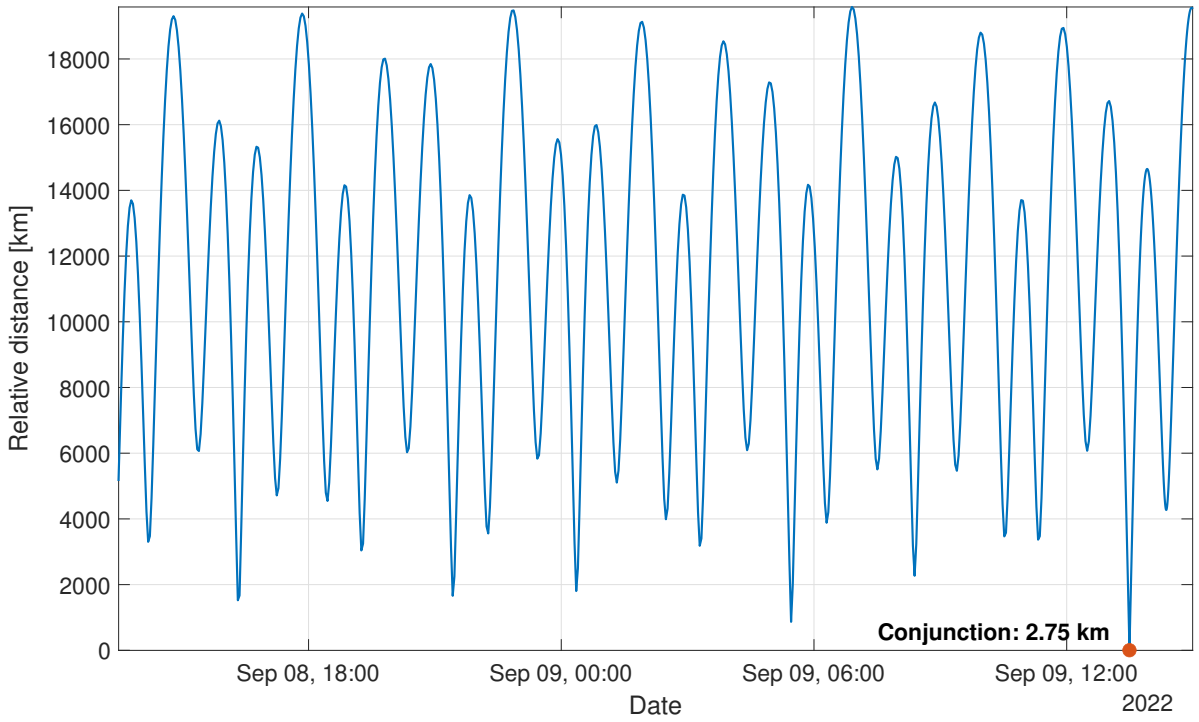

Figure 5.2: Relative distance between COSMO-Skymed 4 and Elektron 1 between a day earlier and an orbit after the conjunction event

Figure 5.2 shows the relative distance with respect to the asset spacecraft over the considered time window, up to a period after the conjunction epoch. The resulting orbit at TCA is thus displayed in Figure 5.3. For the Least Square filter, the a priori state is set equal to the reference, while the covariance is expressed in Equation (5.1).

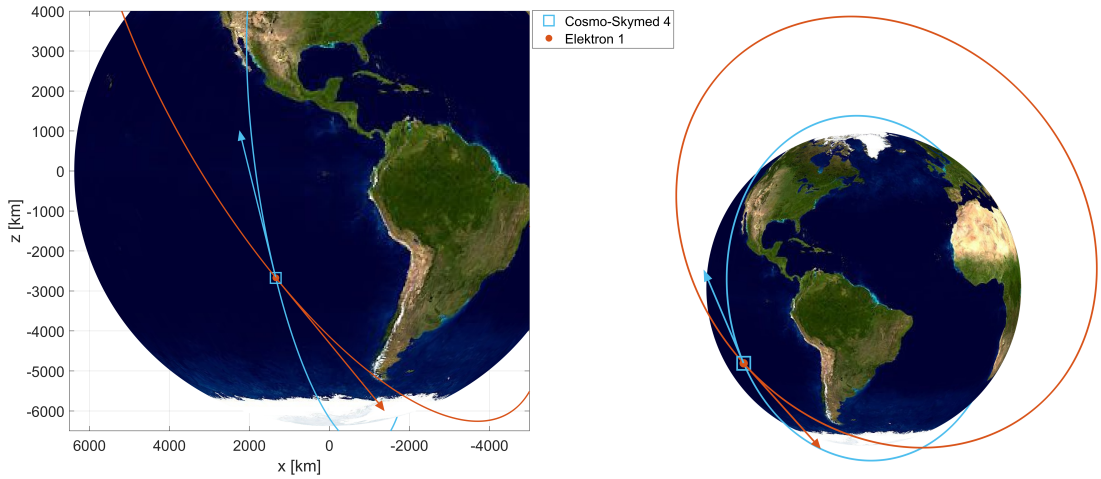

Figure 5.3: COSMO-Skymed 4 and Elektron 1 orbits during the conjunction event. The arrows represent the two objects velocity vectors.

$$\begin{cases} \sigma_r = [1, 3, 1] \ \ [km] \\ \sigma_v = [0.005, 0.02, 0.002] \ \ [km/s] \end{cases} \tag{5.1}$$

The results are evaluated in terms of norm of the error with respect to the reference and square root of the trace of the covariance matrix. The former is not affected by the consider covariance analysis and, for Elektron 1, it is equal to 40 meters, with an estimated distance from COSMO of 2.748 kilometers. The target positional covariance trace is 270 meters, to which 39 m are summed to take into account primary uncertainties, as shown in Equation (4.12). The combined covariance is thus obtained summing the result the UKF output described below, with a final value of $C = 88$ m, already in B-plane coordinates. The conjunction is then plotted on the B-plane as in Figure 5.4. Considering the miss distance of 2.75 km and the computed covariance, the probability of collision is actually zero, and no collision avoidance manoeuvre is deemed necessary. Still, the output uncertainty is not particularly small, suggesting that a more accurate STM model or additional iterations may be required if the expected minimum distance between the two objects was smaller.

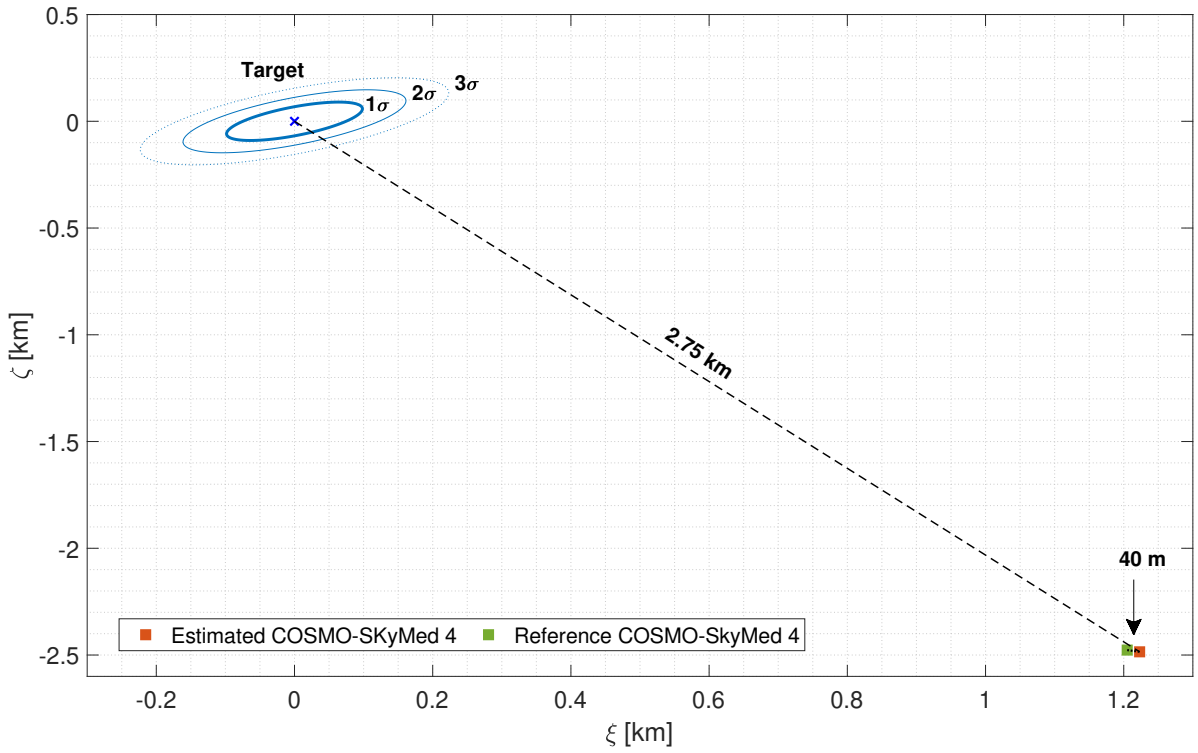

Figure 5.4: COSMO-SkyMed 4 and Elektron 1 projected onto the B-plane at the conjunction epoch. The combined covariance is centered at the target.

These results refer to the processing of the whole measurement batch, up to one day before the conjunction. However, it is still possible to consider only a smaller set of observations, for instance, to allocate more time to mission related tasks or to optimize scheduling of multiple objects tracking. Hence, the square root of the LSQ covariance trace is plotted in Figure 5.5 for an increasing number of target passages, starting from only two visibility windows, or 22 measurements; the filter performance are still more than satisfactory, with the curve reaching the final value of 270 m after approximately 40 passages.

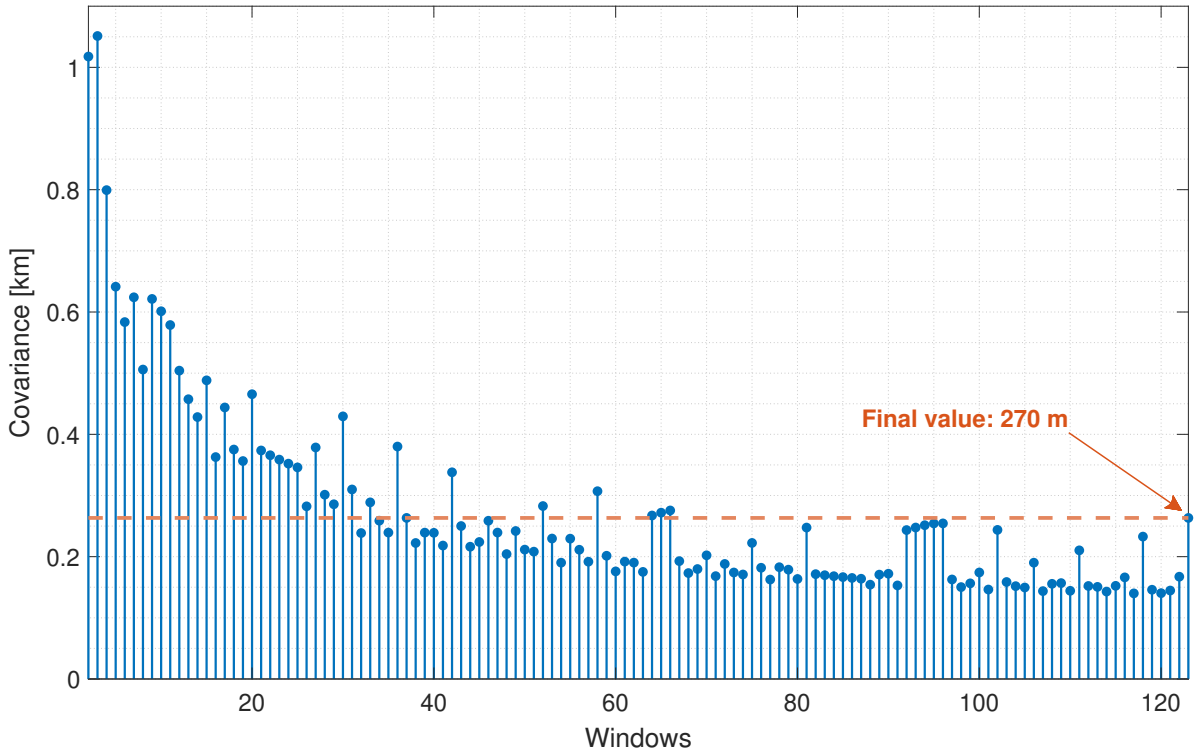

Figure 5.5: Elektron 1 covariance trend with increasing number of passages

5.1.2. Falcon 1 conjunction

Falcon 1 was the first fully private liquid-fueled launch vehicle developed by *SpaceX* and operated from 2006 and 2009, capable of carrying up to 470 kilograms in low Earth orbit. All flights were launched form *Omelek Island* in Kwajalein Atoll, a near equatorial launch site, where orbit inclinations as low as 9 degrees can be achieved. Being a two-stage rocket, the second stage did not reentered the atmosphere and the rocket body from the last launch in July 2009 still orbits in a quasi-equatorial orbit at around 650 km of altitude [7]. The full vehicle, with its upper stage, is sketched in Figure 5.6.

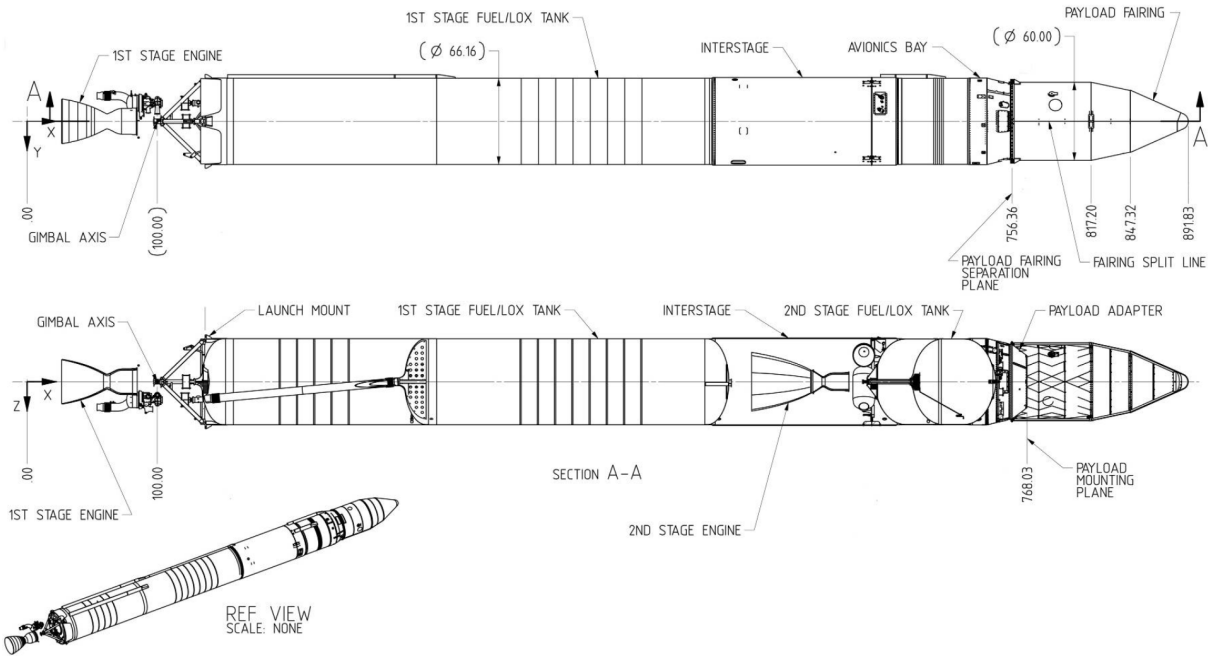

Figure 5.6: Falcon 1 small-lift launch vehicle. *Credits: SpaceX*

The debris is quite large, with a radar cross section of more than four squared meters and a highly different orbit with respect to Elektron 1. At the observations epoch, RAAN and inclination are about 329 and 9 degrees respectively, while eccentricity is closer to zero. Considering the statistical analysis, the object is characterized by a higher number of windows at 165, and visibility time of only 16 hours, increasing to 22 without the specific sensor limits and 56 when no limits at all are considered; given the high RCS, the value is probably increased by a greater phase angle, responsible for a reduction of the apparent magnitude. Due to the relative orbit inclination, the uniformity index is particularly low at 0.25 (though it reaches 0.5 without limits). As a consequence, much less observations can be processed, but still a more than sufficient number of 284. Though the RAAN is outside the 200-300 degrees range, the revisit time is still almost constant just below 2000 seconds, with the maximum increasing at 5500 when sensor limits are enforced.

Similarly, the relative distance and the orbit at the conjunction epoch are shown in Figures 5.7 and 5.8.

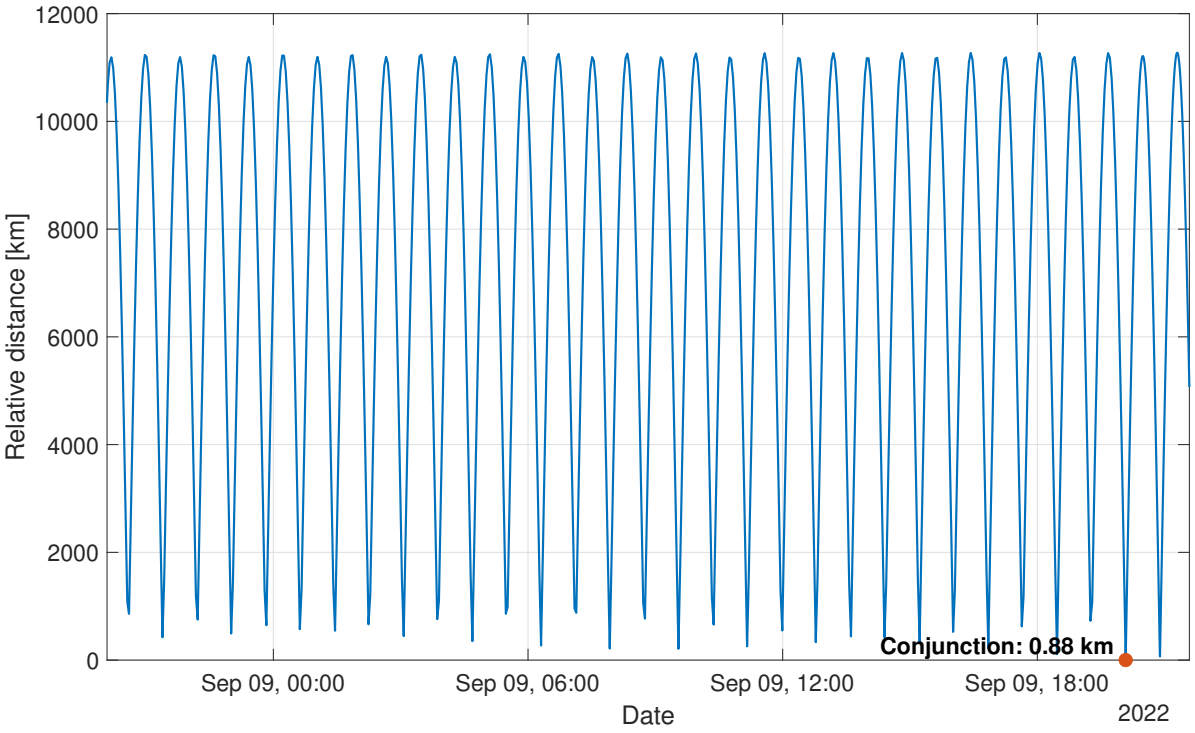

Figure 5.7: Relative distance between COSMO-Skymed 4 and Falcon 1 r/b, between a day earlier and an orbit after the conjunction event

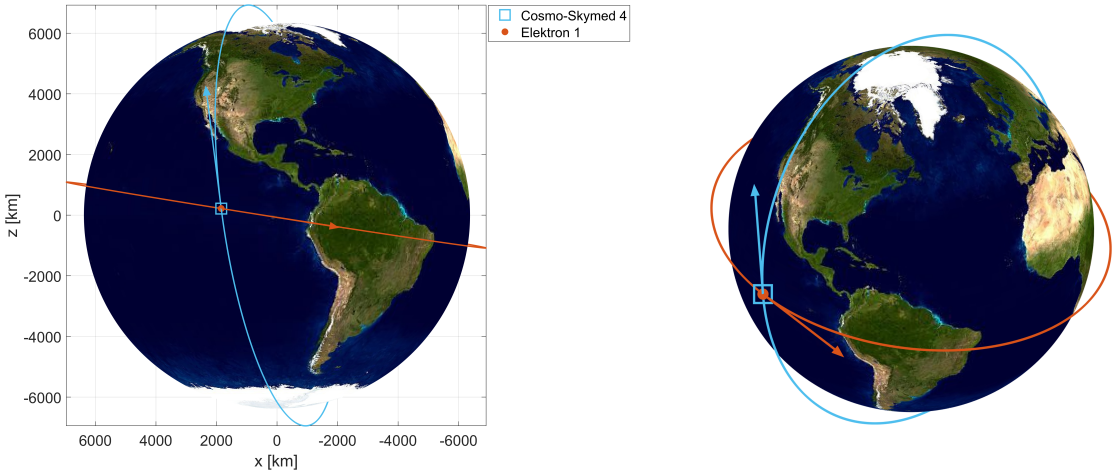

Figure 5.8: COSMO-SkyMed 4 and Falcon 1 orbits during the conjunction event. The arrows represent the two objects velocity vectors.

Considering the same a priori information as the Elektron 1 results, the error norm at the nominal TCA is only 23 meters, with a combined covariance of 131 m (already projected), of which 76 m are derived from the Least Squares and 120 m from the CCA. Given a miss distance of 871 meters, the probability of collision is once again effectively equal to

zero. The primary OD results are actually the same given the similar time window of the simulation. The estimated distance is now much closer to the expected value, despite the poorer target visibility. Therefore, the results difference can be explained mainly by the different orbits; given its higher eccentricity, Elektron 1 is much more affected by third body perturbations, solar radiation pressure and drag[1]. On the contrary, Falcon 1 lies in a circular orbit at 650 km, where these effects are much smaller, if not negligible, for the considered time windows. The results in B-plane coordinates are thus shown in Figure 5.9.

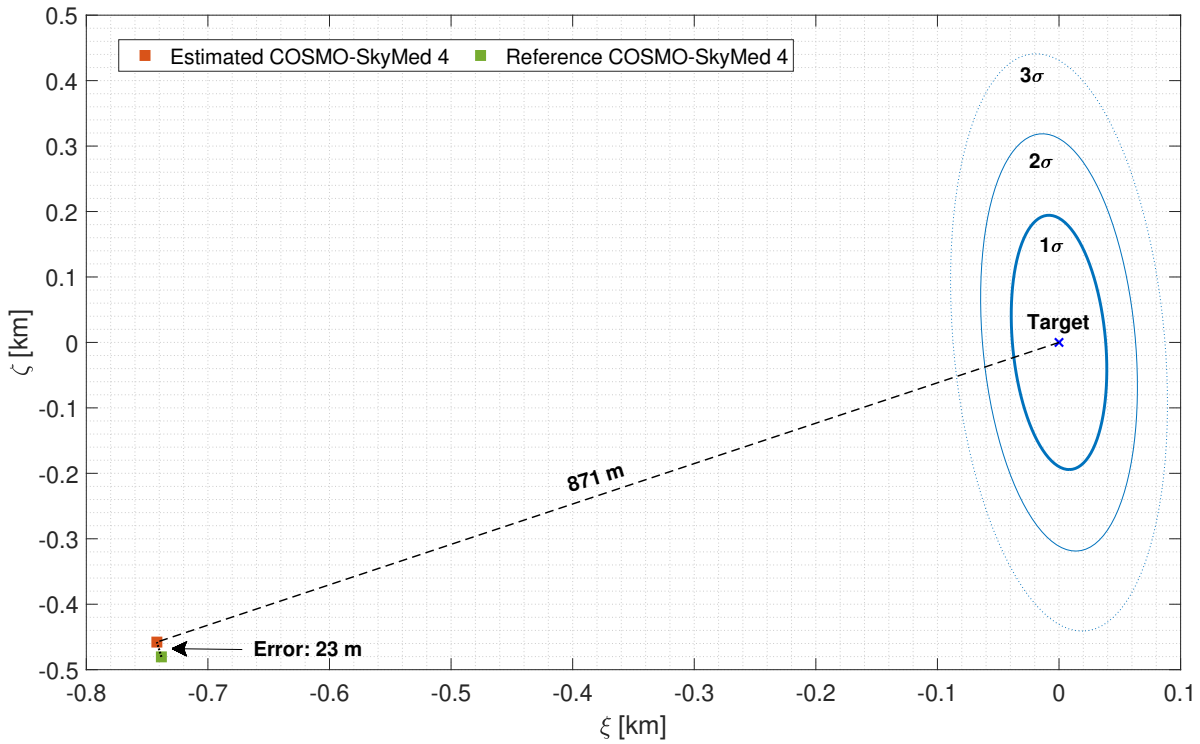

Figure 5.9: COSMO-SkyMed 4 and Falcon 1 projected onto the B-plane at the conjunction epoch. The combined covariance is centered at the target.

Similar to the previous event, the covariance trend is reported in Figure 5.10 as function of the number of visibility windows, starting from the second passage, with only 8 measurements. Due to an overall shorter window duration, the covariance reaches the final value of 76 meters after more than 100 passages, though only 20 are actually needed to match the performance obtained with the Elektron 1 conjunction.

[1]The perigee is in fact at only 400 km and the atmospheric perturbation is no longer negligible.

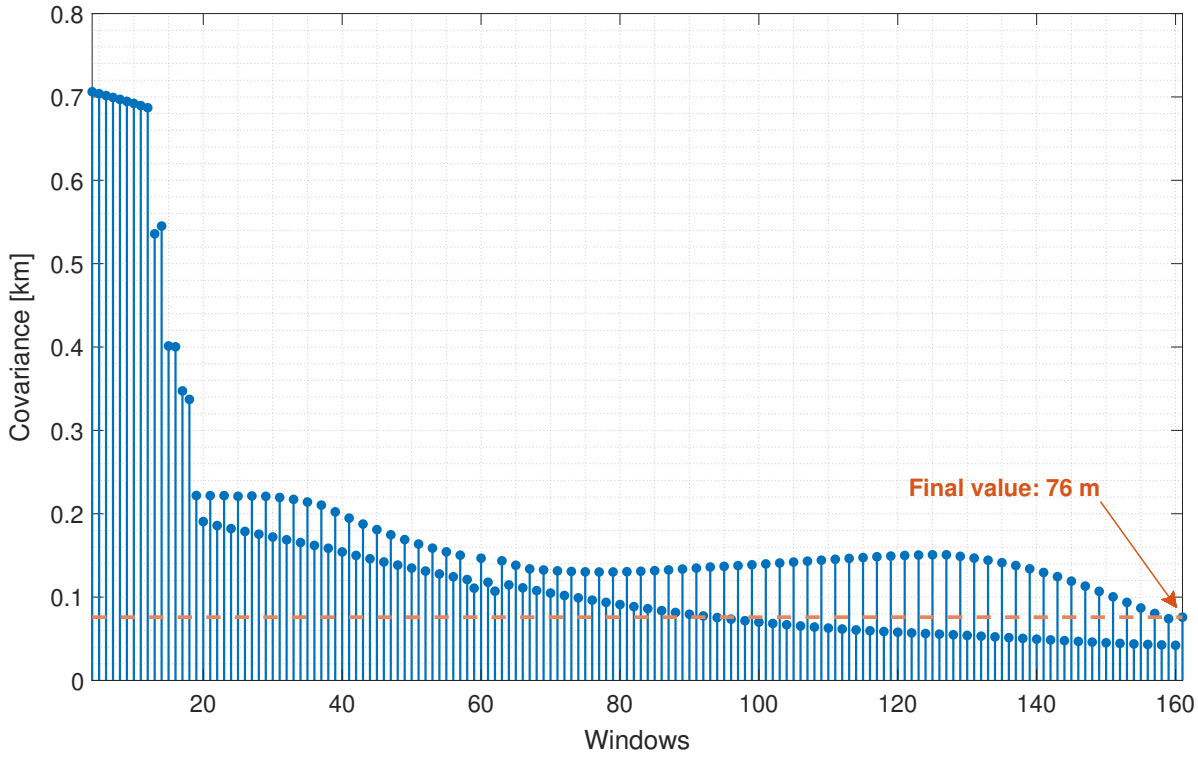

Figure 5.10: Falcon 1 covariance trend with increasing number of passages

5.2. Ground-based analysis

The validation of the onboard OD and conjunction analysis is performed against a ground-based simulation, performed for both targets, with an Unscented Kalman Filter. The measurement campaign of each sensor is identified by a simple geometrical limit, enforced by computing the elevation with respect to the minimum value of 20 degrees, as in Figure 5.11 for COSMO-SkyMed satellite and the three stations. However, Falcon 1 cannot be observed for the considered ground stations due to the low orbit inclination of only 9 degrees; therefore, a fourth sensor located in French Guyana and identical to *S3TSR* is considered, for this specific case only.

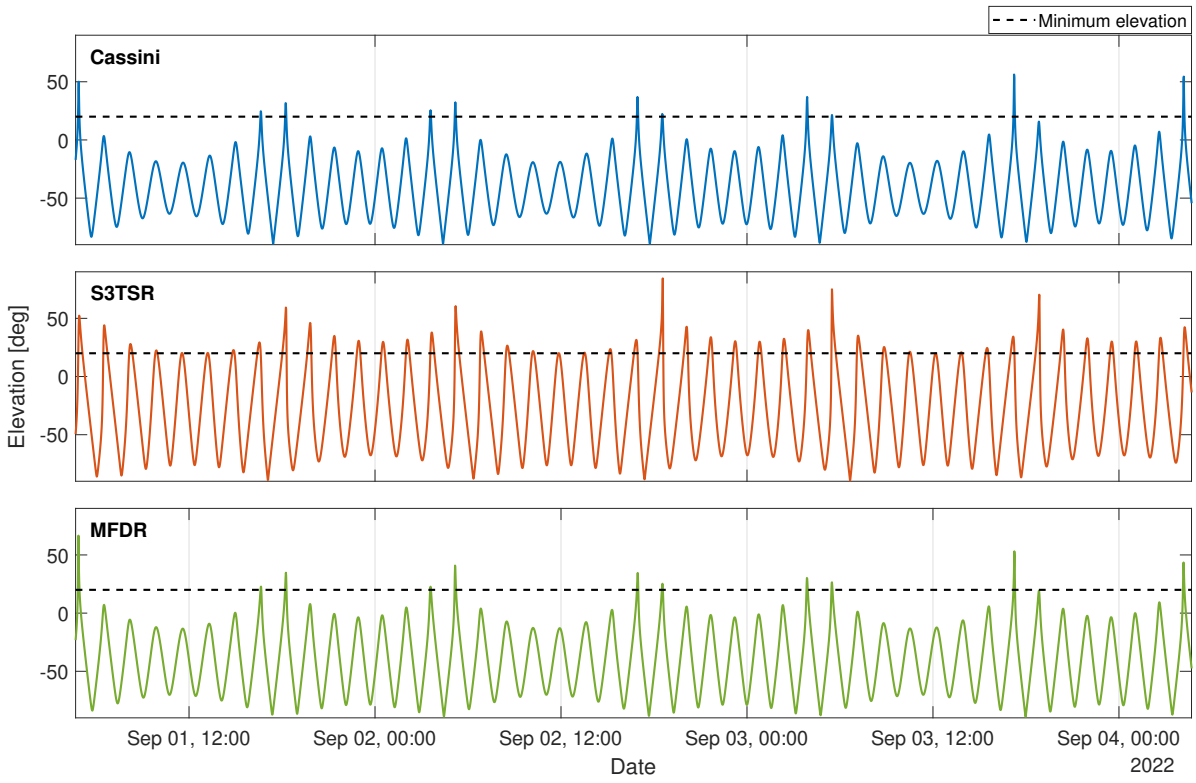

Figure 5.11: Elevation of COSMO-SkyMed 4 with respect to Cassini (above), S3TSR (middle) and MFDR (below) for the first four days of simulation. The minimum elevation line is set at 20 degrees for all the sensors.

Measurements are taken up to the last available before the nominal TCA as the sequential filter allows to process observations in real-time, potentially providing a constant update on the conjunction event. However, since the last measurement, it is generally required to propagate state and covariance up to the TCA, resulting in a greater final error and larger covariance for longer propagations. The asset spacecraft is characterized by very accurate a priori information, with the state equal to the reference and covariance as described in Equation (4.9). Thus, as in Figure 5.12, both the positional error and the trace have already reached steady state behaviour, at around 23 and 33 meters respectively, with a total of 211 measurements. It is worth noting that the error is lower than the 3σ line proving the validity of the chosen process noise and dynamical model.

Elektron 1 elevation for the three stations is thus reported in Figure 5.13. Thanks to a longer orbit period, the satellite visibility is higher, granting more measurements and potentially greater estimation accuracy. Similarly, Falcon 1 is highlighted in Figure 5.14, with the difference that *S3TSR* sensor is now located much nearer to the equator, allowing to have visibility from at least one station.

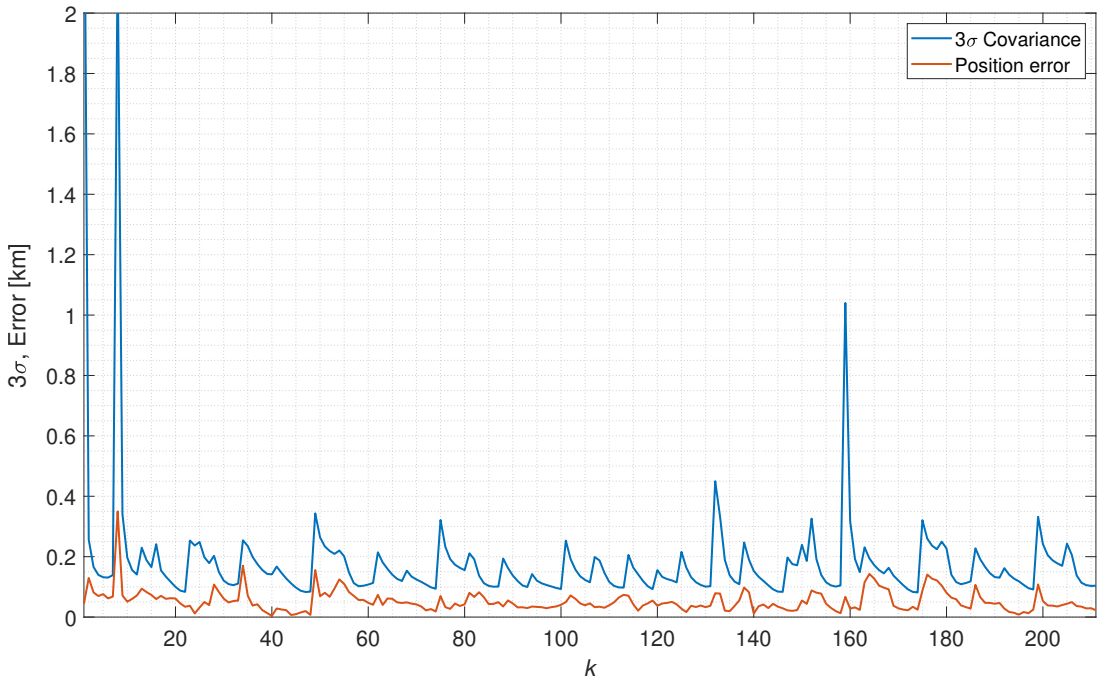

Figure 5.12: Covariance and error for COSMO-SkyMed 4 function of the processed measurements. The former is expressed in terms of 3σ, where σ is the square root of the trace of the positional component only.

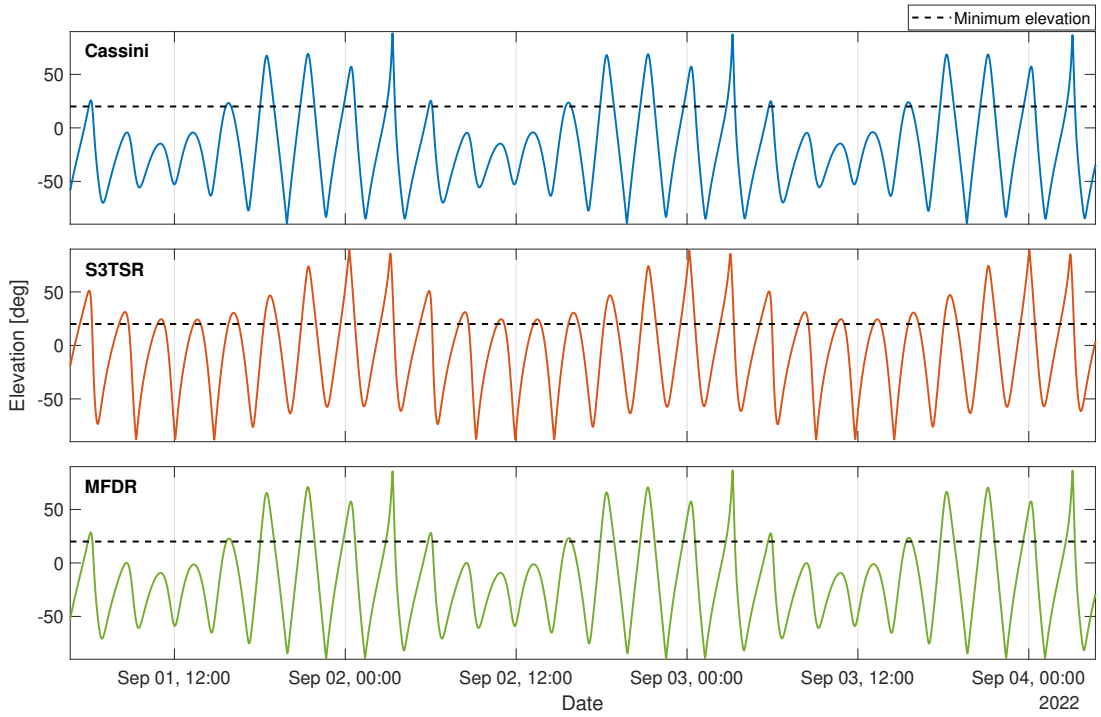

Figure 5.13: Elevation of Elektron 1 with respect to Cassini (above), S3TSR (middle) and MFDR (below). The minimum elevation line is set at 20 degrees for all the sensors.

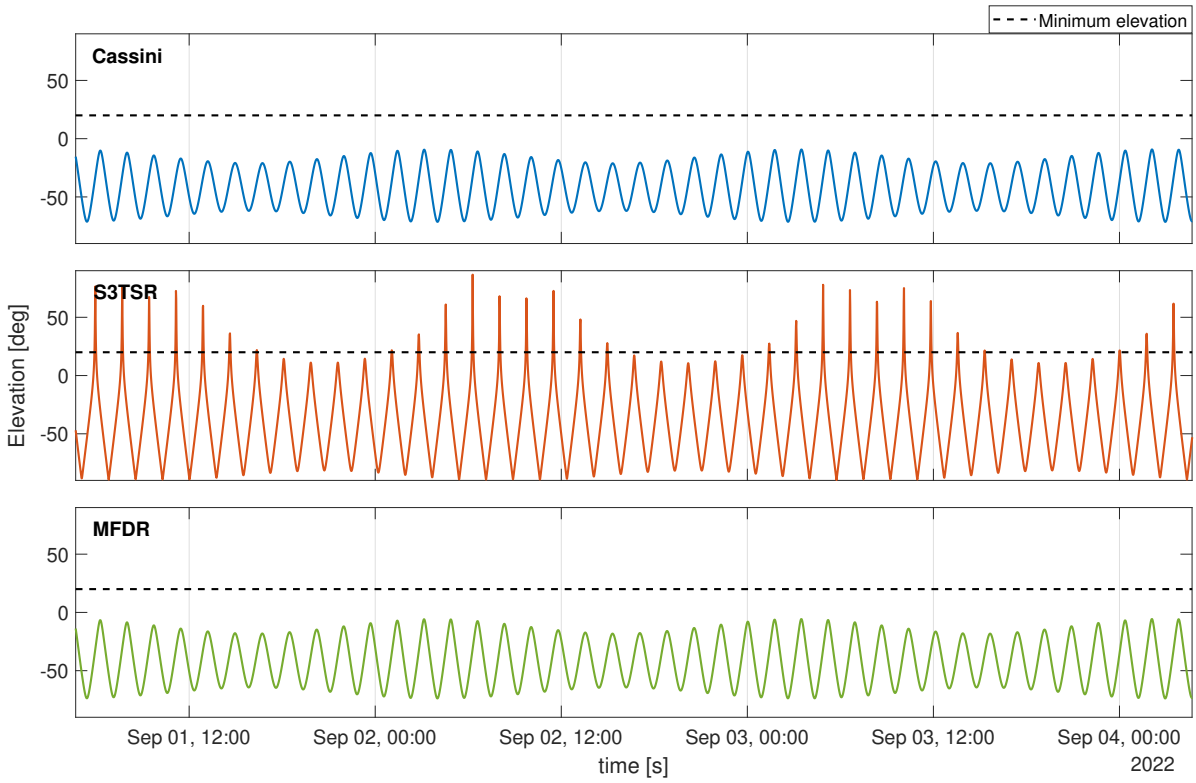

Figure 5.14: Elevation of Falcon 1 with respect to Cassini (above), S3TSR (middle) and MFDR (below). The minimum elevation line is set at 20 degrees for all the sensors.

The trends of the square root of the covariance trace and positional error norm for Elektron 1 and Falcon 1 are presented in Figures 5.15 and 5.16. As expected by the elevation graph, the former is characterized by a large number of 2356 measurements, which results in generally better performance. The covariance trace square root is only 27 meters, with an error of 22 m, despite the worse a priori information with respect to the asset spacecraft. On the contrary, Falcon 1 results are overall worse, notwithstanding the 438 available observations coming from a single station. The final value of the trace square root and positional error are approximately 110 and 120 meters respectively, though they lie in correspondence of a spike; looking at the general trend, the result is more similar to COSMO-SkyMed, with the covariance around 33 meters.

In principle, it is possible to improve the results adopting ground stations more spread in latitude and longitude, allowing to fill the visibility gaps and thus to obtain a smoother estimate process.

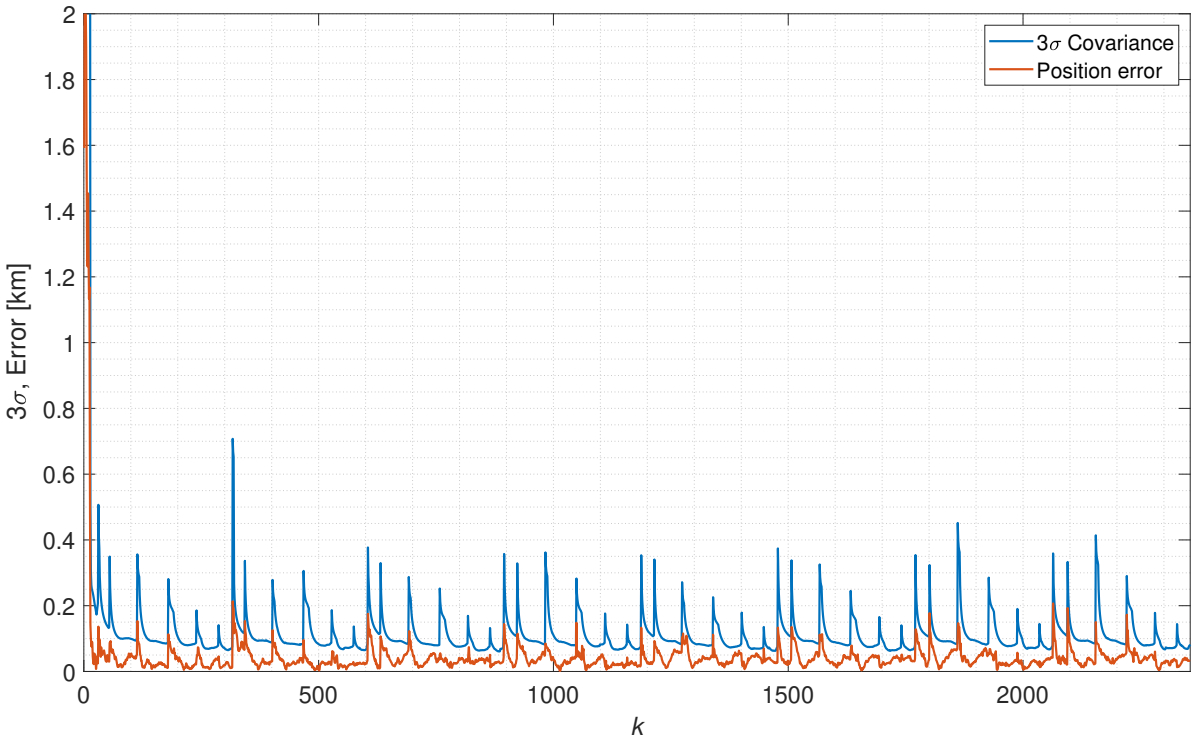

Figure 5.15: Covariance and error for Elektron 1 satellite function of the processed measurements. The former is expressed in terms of 3σ.

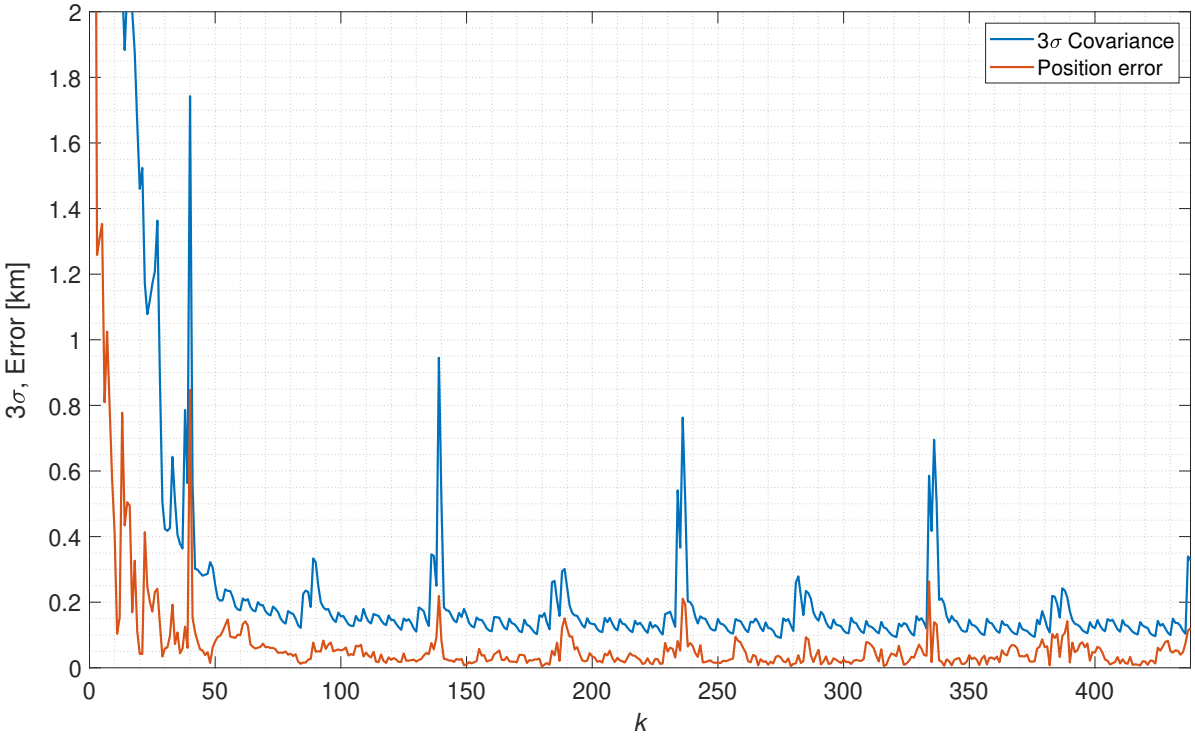

Figure 5.16: Covariance and error for Falcon 1 r/b function of the processed measurements. The former is expressed in terms of 3σ.

5.3. Overview and comparison

The proposed filter technique provides very good results especially for low eccentricity LEO objects, where the effects of perturbations are mainly due to non-spherical gravity field. The ground-based results are in general better in terms of covariance, thanks to higher sensor accuracy and filter performance, with the added possibility to determine the exact conjunction epoch[2]. However, this advantage comes at the cost of a more complex algorithm, with higher computational cost and reduced flexibility. The possibility to directly estimate state and covariance at TCA allows to have a much faster code, where the nominal trajectory propagation is performed only once thanks to the single iteration solution of the Least Squares. Moreover, the space-based sensor is definitely more flexible, capable of seeing objects of very different orbits with an overall better target visibility with respect to the multiple ground stations required, in particular for observation of low orbit inclination objects. Finally, even though the UKF results are better, they must be further propagated to the conjunction epoch in order to compute the probability of collision, which leads to greater error and covariance. For particularly long propagations, the result may be actually worse than the onboard Least Square. On the other hand, the latter needs a sufficiently accurate reference trajectory to provide consistent results, and the proposed SGP4 solution is not well suited for very long time windows, as the error grows by approximately 1-3 km per day. Moreover, also the STM computed at each observational epoch requires to consider orbital perturbations, although for the case at study the J2 effect alone provides a sufficiently accurate solution. Overall, the onboard analysis results are summarized in Table 5.1 for both objects. Computational times are in the order of a few seconds for the onboard analysis, increasing to approximately half an hour for the ground-based UKF, requiring the implementation of high precision orbit propagator producing similar results to SGP4. It is possible to greatly reduce the required time by adopting a simpler model based on J2 only at the cost of lower accuracy with respect to the space-based analysis.

[2]More correctly, the *best estimate* of the conjunction epoch, as the exact TCA is never fully known

	Elektron 1	**Falcon 1**
Object spherical radius $[m]$	0.91	1.19
Observations	786	284
Positional Error $[m]$	40	23
LSQ covariance trace (positional) $[m]$	270	76.2
CCA covariance trace (positional) $[m]$	39	120
Minimum distance $[km]$	2.748	0.871
RAAN $[deg]$	256	329
Visibility windows (with limits)	122	165
Visibility time (with limits) $[h]$	47	16
Uniformity index (with limits)	0.67	0.25
Mean revisit time (with limits) $[min]$	59.6	55.5

Table 5.1: Onboard results for Elektron 1 and Falcon 1 r/b

6 | Conclusions and future developments

This work provided a statistical analysis of an onboard optical sensor with respect to a catalogue of potentially dangerous targets, focusing on the possible observation opportunities as part of an autonomous, space-based conjunction analysis. It was possible to determine various parameters deemed relevant to draw appropriate conclusions regarding the objects observability, with progressively increasing the specific limitations of the adopted sensor. The base limit refers to pure geometrical visibility and the target is considered observable if the line of sight is above the Earth horizon; the second limit imposed is the sun illumination of the object, as only passive targets have been considered[1]. This requirement is the first differentiation between optical and radar sensors. The last limit is specific to the simulated scenario: an optical camera, with given limiting magnitude of 15 and minimum Sun separation of 30 degrees. Target visibility did worsen, but only for smaller objects, in particular with an equivalent sphere radius lower than 10 cm or phase angle close to 180°; on the contrary, Sun separation did not have significant impact on the visibility, probably due to the specific asset orbit and Sun-Earth relative position.

Different orbital parameters have been considered and the main correlation regarded the longitude of the ascending node, with the highest visibility for satellites with RAAN ranging between 200 and 300 degrees, a sensible value considering that the asset is about 70 degrees. When dealing with space-based observations, an important parameter is found in the measurement uniformity along the observer orbit; for the considered scenario, a maximum index of 0.67 was computed, independently of targets orbit; this value is easily reached for satellites with RAAN around 250 degrees, also when limitations are applied. The last important parameter characterized by relevant correlations is the revisit time between two observations. In this case, some objects have a maximum value higher than one day, while the minimum is generally limited to approximately 3000 seconds. Nonetheless, when RAAN is between 200° and 300° both the revisit times tends to become

[1]There is in fact the possibility to have an active source of light on the observed satellite to take measurements also when in Earth shadow.

constant at around 2000/2500 seconds. This behaviour was found to be independent on the specific orbit inclination.

Even when only the geometric constraint is enforced, about 5% of the 425 considered objects are never visible in the simulation time window. This is an important factor in evaluating the performance of a space-based sensor for observation of potentially hazardous targets. Despite this, satellites with RAAN between 200 and 300 degrees are always visible.

Thanks to the first part of the simulation, it was then possible to determine any close encounter occurring in the week after the scenario time window. Six different conjunctions were found, with one below 1 km. Relative orbit determination and consequent conjunction analysis was thus performed for the two closest approaches, involving Elektron 1 decommissioned satellite and Falcon 1 rocket body. The single iteration Least Squares filter, adopted for the onboard computation, provided very good results for both objects, with limited positional errors and covariances, even when only a smaller set of measurements was considered. On the other hand, Elektron 1 was characterized by slightly worse values, probably due to lower accuracy of the J2-propagated STM when dealing with a low perigee and high eccentricity target orbit.

The results have been compared to a canonical analysis based on three different ground stations and Unscented Kalman Filter, modeled with a high precision orbit propagator. Although a sequential algorithm cannot compute state and covariance estimates directly at the TCA, the provided results were slightly closer to the nominal motion, at the expense of a much higher computational cost.

Overall, the proposed filtering method allowed to compute accurate state estimation in a fraction of time with respect to a typical ground-based analysis. Moreover, a space-based sensor is characterized by a greater target visibility, mainly thanks to its higher altitude and faster revisit time with respect to a ground station, whose performance are strongly influenced by the specific object orbit.

Future developments

This research is only a first step towards a more generalized autonomous collision avoidance system, capable of performing relative orbit determination and conjunction analysis with higher accuracy also for orbits characterized by stronger perturbative effects. Yet, a more accurate scenario should be based on real measurements in order to better understand the effects of the chosen model on the estimation accuracy. Another important addition to this research would come from the implementation of observations schedul-

ing, allowing to expand the statistical analysis with a more realistic sensor simulation; this can be further improved by adding satellite attitude dynamics and the required slew manoeuvres needed to correctly point the target objects. Finally, through additional optimization, the proposed linearized OD method could be dropped in favour of a more accurate non-linear sequential filter used to directly solve relative navigation without any ground support for asset motion estimation. Combined with an initial orbit determination process, the end result is a satellite capable of identifying and tracking any potential threat and autonomously determine the need to perform collision avoidance.

Bibliography

[1] ASI. Sistema duale per l'osservazione della terra. URL `https://www.asi.it/scienze-della-terra/cosmo-skymed/`.

[2] R. J. Boain. Ab-cs of sun-synchronous orbit mission design. 2004.

[3] F. K. Chan et al. *Spacecraft collision probability*. Aerospace Press El Segundo, CA, 2008.

[4] A. De Vittori, M. F. Palermo, P. D. Lizia, and R. Armellin. Low-thrust collision avoidance maneuver optimization. *Journal of Guidance, Control, and Dynamics*, 45 (10):1815–1829, 2022.

[5] R. Deakin. Satellite orbits. *School of Mathematical & Geospatial Sciences, RMIT University*, 2007.

[6] E. Doornbos, M. Förster, B. Fritsche, T. van Helleputte, J. van den IJssel, G. Koppenwallner, H. Lühr, D. Rees, P. Visser, and M. Kern. Air density models derived from multi-satellite drag observations. In *Proceedings of ESAs Second Swarm International Science Meeting. Potsdam*, volume 24, 2009.

[7] L. Dreyer. Latest developments on spacex's falcon 1 and falcon 9 launch vehicles and dragon spacecraft. In *2009 IEEE Aerospace conference*, pages 1–15. IEEE, 2009.

[8] ESA. *ESA's Space Environment Report*. Techincal Report, ESA, 2022.

[9] N. Faraco, G. Purpura, P. Di Lizia, M. Massari, M. Peroni, A. Panico, A. Cecchini, F. Del Prete, et al. Snos: automatic optimal observations scheduling for sensor networks. In *9th European Conference for Aerospace Sciences (EUCASS 2022)*, pages 1–11, 2022.

[10] P. Faucher, R. Peldszus, and A. Gravier. Operational space surveillance and tracking in europe. *Journal of Space Safety Engineering*, 7(3):420–425, 2020.

[11] E. Gamper, C. Kebschull, and E. Stoll. Statistical orbit determination using the ensemble kalman filter. *Acta Astronaut*, pages 22–24, 2018.

[12] I. Gomez, I. A. Gómez, and S. Vildarraz. Architectural description of the spanish space surveillance and tracking system. In *Proc. 7th European Conf. Space Debris*, pages 18–21, 2017.

[13] R. Gomez, P. Besso, G. Pinna, M. Alessandrini, J. Salmerón, and M. A. R. Prada. Initial operations of the breakthrough spanish space surveillance and tracking radar (s3tsr) in the european context. In *Proceedings of the 1st ESA NEO and Debris Detection Conference, Darmstadt, Germany*, pages 22–24, 2019.

[14] H. Harper. The method of least squares and some alternatives. part i, ii, ii, iv, v, vi. *International Satistical Review*, 42:147–174, 1974.

[15] F. R. Hoots and R. L. Roehrich. Models for propagation of norad element sets. Technical report, Aerospace Defense Command Peterson AFB CO Office of Astrodynamics, 1980.

[16] E. S. Ince, F. Barthelmes, S. Reißland, K. Elger, C. Förste, F. Flechtner, and H. Schuh. Icgem–15 years of successful collection and distribution of global gravitational models, associated services, and future plans. *Earth system science data*, 11(2):647–674, 2019.

[17] A. Jean-Sébastien, G. Gabriella, et al. Angles-only relative orbit determination during the avanti experiment. In *26th International Symposium on Space Flight Dynamics (ISSFD)*, pages 1–8, 2017.

[18] S. J. Julier and J. K. Uhlmann. Unscented filtering and nonlinear estimation. *Proceedings of the IEEE*, 92(3):401–422, 2004.

[19] D. J. Kessler and B. G. Cour-Palais. Collision frequency of artificial satellites: The creation of a debris belt. *Journal of Geophysical Research: Space Physics*, 83(A6): 2637–2646, 1978.

[20] B. J. Kuiack. *Spacecraft Formation Guidance and Control on J2-Perturbed Eccentric Orbits*. PhD thesis, Carleton University, 2018.

[21] Z. Li, Y. Wang, and W. Zheng. Space-based optical observations on space debris via multipoint of view. *International Journal of Aerospace Engineering*, 2020:1–12, 2020.

[22] J. V. Llop. *Spacecraft flight in the atmosphere*. PhD thesis, Cranfield University, 2014.

[23] V. Morand, C. Yanez, J. D. Perez, C. Fernandez, S. Roussel, X. Pucel, and V. Vidal.

Bas3e: A framework to conceive, design, and validate present and future sst architectures. In *Proceedings of the 1st NASA International Orbital Debris Conference*, page 10, 2019.

[24] A. Morselli. *High order methods for Space Situational Awareness*. PhD thesis, Politecnico di Milano, 2014.

[25] NAIF. An overview of reference frames and coordinate systems in the spice context, 2022. URL `https://naif.jpl.nasa.gov/pub/naif/toolkit_docs/Tutorials/pdf/individual_docs/17_frames_and_coordinate_systems.pdf`.

[26] G. Purpura, A. De Vittori, R. Cipollone, P. Di Lizia, M. Massari, C. Colombo, A. Di Cecco, L. Salotti, et al. Sensit: A software suite for observation scheduling and performance assessment of sst sensor networks. In *INTERNATIONAL ASTRONAUTICAL CONGRESS: IAC PROCEEDINGS*, pages 1–13, 2021.

[27] B. Schutz, B. Tapley, and G. H. Born. *Statistical orbit determination*. Elsevier, 2004.

[28] A. A. Siddiqi. *Challenge to Apollo: the Soviet Union and the space race, 1945-1974*, volume 4408. US National Aeronautics & Space Administration, 2000.

[29] K. Tomiyasu. Conceptual performance of a satellite borne, wide swath synthetic aperture radar. *IEEE Transactions on Geoscience and Remote Sensing*, (2):108–116, 1981.

[30] D. A. Vallado and P. J. Cefola. Two-line element sets-practice and use. In *63rd International Astronautical Congress, Naples, Italy*, pages 1–14, 2012.

[31] G. B. Valsecchi, A. Milani, G. F. Gronchi, and S. R. Chesley. Resonant returns to close approaches: Analytical theory. *Astronomy & Astrophysics*, 408(3):1179–1196, 2003.

[32] E. Vellutini, G. Bianchi, C. Pardini, L. Anselmo, T. Pisanu, P. Di Lizia, F. Piergentili, F. Monaci, M. Reali, W. Villadei, et al. Monitoring the final orbital decay and the re-entry of tiangong-1 with the italian sst ground sensor network. *Journal of Space Safety Engineering*, 7(4):487–501, 2020.

[33] G. Welch, G. Bishop, et al. An introduction to the kalman filter. 1995.

[34] D. H. Won, S. Sung, and Y. J. Lee. Ukf based vision aided navigation system with low grade imu. In *ICCAS 2010*, pages 2435–2438. IEEE, 2010.

[35] J. Yang, C. Han, P. Li, and K. Ding. Reliability analysis of sgp4 using goce satellite. In *AIAA/AAS Astrodynamics Specialist Conference*, page 4281, 2014.

A | Unscented Transform

Let's consider an initial statistics at time t_0 correctly represented by mean and covariance. For nonlinear dynamics, uncertainty propagation would result in biased and incorrect samples distribution if a linear map is adopted; the error is larger for long term propagation. Therefore, the idea of the Unscented Transformation (or UT) is to choose a set of points, called *sigma points* and directly propagate them through the nonlinear function as exemplified in Figure A.1; the statistics of the transformed points is then computed to estimate the resulting mean and covariance.

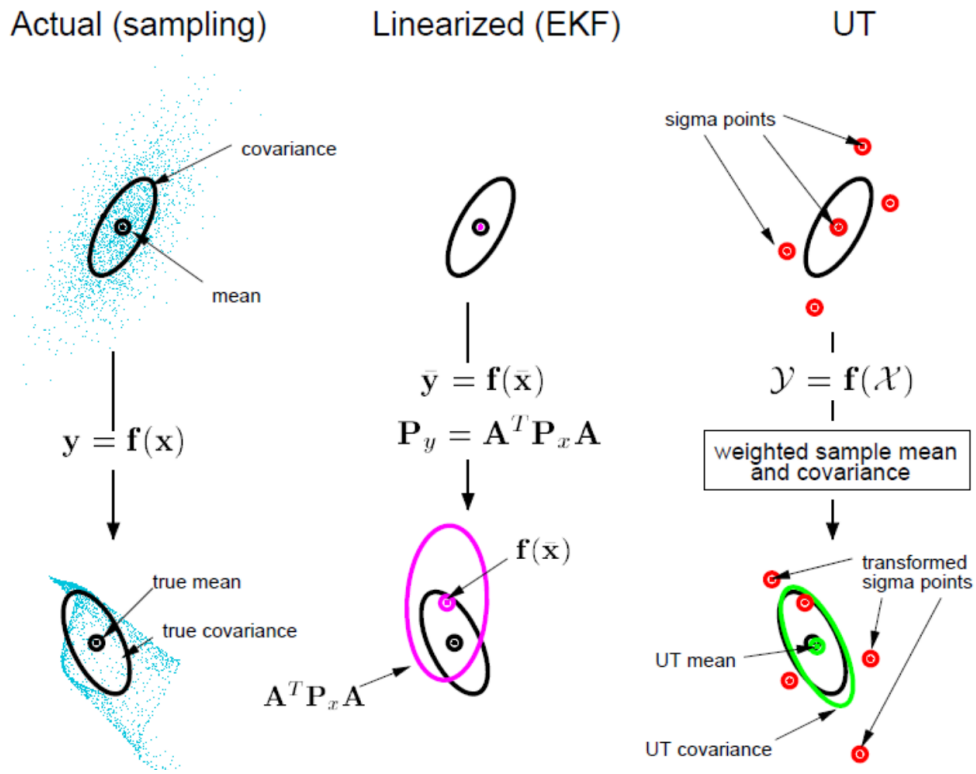

Figure A.1: Comparison between the true uncertainty propagation on the left, linearized method based on the STM in the middle and Unscented Transformation principle on the right [34]

Contrary to a particle filter, the sigma points are not selected at random, rather they are

deterministically chosen in order to exhibit specific properties and result in a high-order information about the distribution that can be captured with very few samples, through which the pdf is properly parameterized. The choice of the points is not unique and they can be conveniently weighted as long as they correctly represent the initial statistics [18].

Given the non linear transformation, with the initial mean $\hat{\boldsymbol{x}}$ and covariance P_x:

$$\boldsymbol{y} = g(\boldsymbol{x}) \tag{A.1}$$

The general formulation of the sigma points can be expressed as:

$$\begin{cases} \chi_0 = \hat{\boldsymbol{x}} \\ \chi_i = \hat{\boldsymbol{x}} + \left(\sqrt{(n+\lambda)P_x}\right)_i, \quad \text{with} \quad i = 1, ..., n \\ \chi_i = \hat{\boldsymbol{x}} - \left(\sqrt{(n+\lambda)P_x}\right)_i, \quad \text{with} \quad i = n+1, ..., 2n \end{cases} \tag{A.2}$$

λ is a scaling parameter, defined in Equation (A.3).

$$\lambda = \alpha^2(n+k) - n \tag{A.3}$$

With α determining the points spreading and typically defined between 10^{-4} and 1, while k usually depends on the state vector dimension n and set equal to zero for an OD problem. Hence, the weights can be computed as in Equation (A.4), where β is generally equal to 2 for a Gaussian distribution [11].

$$\begin{cases} W_0^{(m)} = \dfrac{\lambda}{n+\lambda} \\ W_0^{(c)} = \dfrac{\lambda}{n+\lambda} + (1 - \alpha^2 + \beta) \\ W_i^{(m)} = W_i^c = \dfrac{1}{2(n+\lambda)}, \quad \text{with} \quad i = n+1, ..., 2n \end{cases} \tag{A.4}$$

superscripts (m) and (c) indicate affiliation to the mean and covariance, respectively.

Each sigma point is then propagated through the nonlinear function defined above.

$$\boldsymbol{Y}_i = g(\chi_i), \quad i = 0, ..., 2n \tag{A.5}$$

Finally, in Equation (A.6) the weighted sample mean and covariance is computed.

$$\begin{cases} \hat{\boldsymbol{y}} = \sum_{i=0}^{2n} W_i^m \boldsymbol{Y}_i \\ P_y = \sum_{i=0}^{2n} \left[\boldsymbol{Y}_i - \hat{\boldsymbol{y}}\right] \left[\boldsymbol{Y}_i - \hat{\boldsymbol{y}}\right]^T \end{cases} \tag{A.6}$$

B | Perturbed Orbital Motion

The first mathematical description of the orbital motion of two objects was done by Isaac Newton, from the analysis of the work of Kepler and his famous three law of planetary motion. The deduced Law of Gravitation states that the mutual force of gravitational attraction between two point masses is:

$$F = \frac{G_u M_1 M_2}{r^2} \tag{B.1}$$

with G_u the Universal Constant of Gravitation equal to 6.67×10^{-11} $\mathrm{Nm^2/kg^2}$, r the distance between masses M_1 and M_2. This equation is the basis of the Two-Body Problem, the building block of any mathematical description of orbital mechanics.

The strongest assumption of this model is the approximation of the planet as a point mass, which is gravitationally equivalent to considering a perfectly spherical body with uniform mass distribution. This is clearly not true, but still sufficiently close to reality to provide accurate results for shorter propagations. From Equation (B.1) it is easily shown that the equations of motion are:

$$\ddot{\boldsymbol{r}} = -\frac{\mu \boldsymbol{r}}{r^3} \tag{B.2}$$

For an artificial satellite, the mass can be considered negligible with respect to the Earth and μ is the standard gravitational parameter, computed as the product $G_u M$ and equal to 398600 $\mathrm{km^3/s^2}$ for the Earth. The resulting trajectory is a simple geometrical figure, ellipse, parabola or hyperbola, depending on the initial conditions. However, this is an idealization of a true satellite orbit, obtained assuming that only the planet gravitational force exists.

When lower propagation errors are required, the simple two-body problem hypothesis must be dropped in favour of more accurate modeling of the forces acting on a orbiting object. Nevertheless, dynamics is still Newtonian and the acceleration is given by the ratio between the force and the mass.

$$\ddot{\boldsymbol{r}} = \frac{\boldsymbol{F}}{m} \tag{B.3}$$

The force is thus computed summing all the contributions, coming from the Earth gravity field, the influence of other celestial objects, Solar and Earth radiation pressure, ocean tides, drag and relativity (implemented as a correction factor) [27].

In general, these effects can be divided into gravitational and non-gravitational, with the most important contributions briefly described in the following sections.

B.1. Gravitational Perturbations

Earth gravity model

Given the two masses M_1 and M_2, the gravitational potential can be expressed as:

$$U = \frac{G_u M_1 M_2}{r} \tag{B.4}$$

The resulting force acting on M_2 is simply derived as the gradient of U.

$$\boldsymbol{F} = \nabla U = -\frac{G_u M_1 M_2 \boldsymbol{r}}{r^3} \tag{B.5}$$

with $\boldsymbol{r}$ the position vector of M_2 with respect to M_1. If the body mass distribution is not uniform, the potential is expressed as the integral over the entire object volume, as shown in Equation (B.6).

$$U = M_2 \int\int\int \frac{G_u \gamma dx dy dz}{\rho} \tag{B.6}$$

γ is the mass density associated to an infinitesimal element of mass dm, $dxdydz$ is the infinitesimal volume and ρ the distance between M_2 and dm.

Taking $M_2 = 1$ for convenience and integrating over the mass of M_1:

$$U = \int_M \frac{G_u M}{\rho} \tag{B.7}$$

This expression shows that a constant density sphere is gravitationally equivalent to a point mass. It is possible to expand Equation (B.7) into an infinite series of spherical harmonics with the terms related to the mass distribution collected into coefficients.

$$U = \frac{\mu}{r} + -\frac{\mu^*}{r}\sum_{l=1}^{\infty}\left(\frac{a_e}{r}\right)^l P_l \sin\phi J_l + \frac{\mu^*}{r}\sum_{l=1}^{\infty}\sum_{m=1}^{l}\left(\frac{a_e}{r}\right)^l P_{lm}\sin\phi\left[C_{lm}\cos m\lambda + S_{ml}\sin m\lambda\right] \tag{B.8}$$

The position of M_2 is now expressed in spherical coordinates (r, ϕ, λ), ϕ the geocentric latitude and λ the longitude. $\mu^* = G_u M^*$ and a_e are scale factors involving a reference mass and a reference distance introduced to adimensionalize the mass property coefficients C_{lm} and S_{lm} [27]; in general, M^* is the mass of the body and a_e its mean equatorial radius. P_{lm} are Legendre's Associated Functions of *degree* l and *order* m. The spherical harmonics coefficients J_l, C_{lm} and S_{lm} represent the mass properties of the body. The former is typically referred to as *zonal harmonics*, related to C_{lm} by the expression $J_l = -C_{l,0}$; C_{lm} and S_{lm} are called *sectoral* if $l = m$, *tesseral* if $l \neq m$, as visualized in Figure B.1. The Legendre functions for high degree are characterized by large numerical values with very small coefficients, hence the potential is generally formulated using normalized Legendre polynomials.

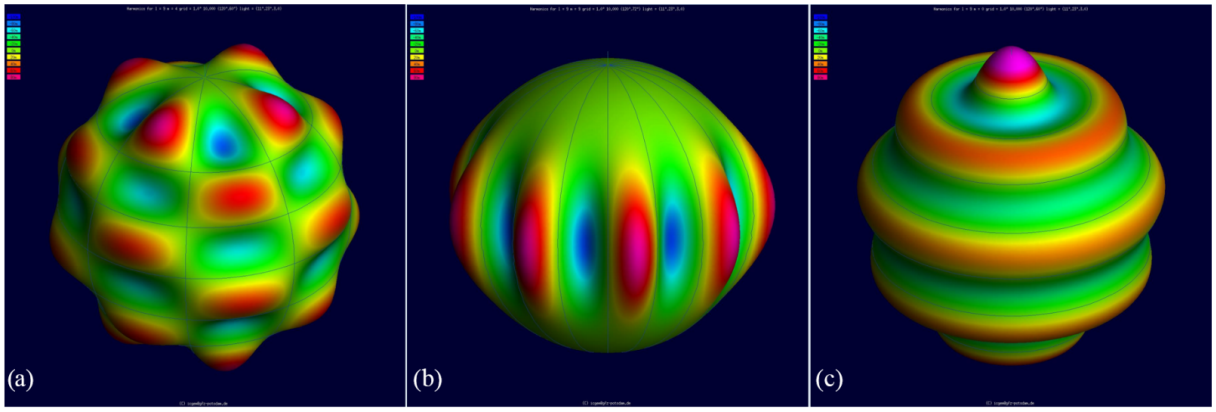

Figure B.1: Visualization of spherical harmonics: tesseral (left), sectoral (middle) and zonal (right) [16]

If the Earth is approximated as an ellipsoid of revolution of constant mass density, there is no longitudinal dependency of the mass distribution and both C_{lm} and S_{lm} are zero for all nonzero m; moreover, due to the symmetry with respect to the equator, there are no odd-degree zonal harmonics. Therefore, other than the point mass term, approximately 95% of the gravitational force is derived from the degree-two term J_2 [27].

Overall, for an artificial satellite, the acceleration due to the Earth gravity field is given by the term of Equation (B.2) for a uniform mass distribution, plus the contribution of the non-spherical terms of U for the chosen degree and order.

Third-body effects

Although in Earth orbit, a satellite is subject to the gravitational effect of any massive object in the solar system, with the main contribution coming from Sun and Moon. This is

accounted as a perturbative force added to the two-body equations of motion, as expressed in Equation (B.9).

$$\boldsymbol{f}_{3B} = \sum_{j=1}^{n_p} \mu_j \left(\frac{\boldsymbol{\Delta}_j}{\Delta_j^3} - \frac{\boldsymbol{r}_j}{r_j^3} \right) \tag{B.9}$$

n_p is the number of bodies, $\boldsymbol{\Delta}$ is the position vector of the body with respect to the satellite and $\boldsymbol{r}$ with respect to the Earth; hence, the two terms are often referred to as *direct* and *indirect* effects respectively. This equation is still based on the assumption of uniform mass distribution for any additional body and the expression would be much more complex if the full gravitational potential is considered; nevertheless, such a high accuracy is in general not needed for these kind of perturbative effects. For particular applications, it is possible to include the interaction between Earth oblateness and the third body, also called *indirect oblateness*, as the main contribution from the Earth potential model [27].

Other gravitational effects

The mass property coefficients, C_{lm} and S_{lm} are constant only if the mass distribution of the body is constant over time. However, all the celestial objects tend to deform and redistribute their mass, leading to a change in the coefficients. The Earth is also subject to this phenomenon, in the form of ocean tides and deformations due to gravitational perturbations of the Sun and Moon. The most relevant effect is a temporal change in degree two coefficients, and in particular J_2. The magnitude of ΔJ_2 is about 10^{-8}, compared to the 10^{-3} of the Earth oblateness term.

For high accuracy applications, a Newtonian dynamics is often not sufficiently accurate and additional terms must be introduced to account for relativistic effects. The main perturbation is an advance, albeit small, of the argument of perigee, of approximately 10 arcseconds per year. The resulting acceleration is thus expressed in Equation (B.10), where c is the speed of light, while β and γ are parameters in the isotropic Parameterized Post-Newtoninan metric, equal to one in General Relativity [27].

$$\boldsymbol{f}_g = \frac{\mu}{c^2 r^3} \left\{ \left[2(\beta+\gamma)\frac{\mu}{r} - \gamma(\dot{\boldsymbol{r}}\cdot\dot{\boldsymbol{r}}) \right] \boldsymbol{r} + 2(1+\gamma)(\boldsymbol{r}\cdot\dot{\boldsymbol{r}})\dot{\boldsymbol{r}} \right\} \tag{B.10}$$

B.2. Non-gravitational Perturbations

Atmospheric drag

Drag can be the most important perturbative force for low altitude satellite. Contrary to the gravitational effects, it is a dissipative force acting opposite with respect to the

relative velocity between the spacecraft and the atmosphere. The resulting acceleration is derived from aerodynamics considerations and takes the famous form:

$$\boldsymbol{f}_{Drag} = -\frac{1}{2}\rho\left(\frac{C_D A}{m}\right) V_r \boldsymbol{V}_r \tag{B.11}$$

The term in brackets is the inverse of the *ballistic coefficient* and it is an indication of the drag acting on the object with respect to its mass. In SGP4 the drag contribution is taken directly from TLEs as *BSTAR*, computed as $\frac{\rho_0 B}{2}$, with ρ_0 the reference air density equal to 0.1570 kg/(m^2 R$_{Earth}$) [15]. This allows to reduce the expression of the acceleration to:

$$f_{Drag} = \frac{\rho}{\rho_0} B^* V^2 \tag{B.12}$$

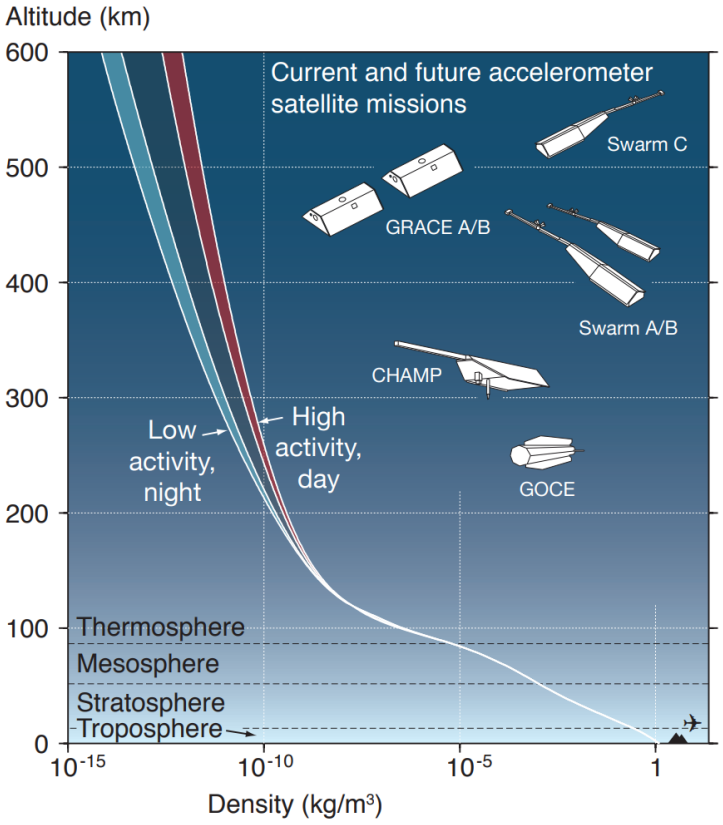

Figure B.2: Qualitative density profiles of Earth's atmosphere shown with the approximate orbital altitudes of some accelerometer's carrying satellites. Note the high variability exhibited under different environmental conditions [6]

Being a dissipative force, drag reduces the orbit energy, resulting in a semi-major axis and eccentricity decaying. When the altitude is particularly low, the higher atmospheric

density causes a strong increase in the heat flux, resulting in possible destruction of the satellite, starting from solar panels and appendages.

As highlighted in Figure B.2, even though density is known to exhibit an approximately exponential reduction with altitude, very accurate modeling is extremely difficult, due to the influence of day-night cycle, the location of the subsolar point, seasonal variations, solar and geomagnetic activities; over an orbital revolution, a satellite can experience up to an order of magnitude change in density.

Solar Radiation Pressure

SRP is the other most relevant non-gravitational perturbation, along with drag. It results from the transfer of momentum due to impact, reflection, absorption and re-emission of photons; its contribution to the equations of motion is given by the expression:

$$\boldsymbol{f}_{SRP} = -P\frac{\nu A}{m}C_R\boldsymbol{u} \tag{B.13}$$

P is the momentum flux from the Sun, A is the cross-sectional area normal to the Sun, $\boldsymbol{u}$ the unit vector from the satellite in the direction of the Sun, C_R the reflectivity coefficient (approximately equal to one) and ν the eclipse factor. The satellite is in shadow when $\nu = 0$ and in sunlight for $\nu = 1$. The value of P at about one Astronomical Unit is approximately 4.56×10^{-6} N/m^2.

Considering the reflected and emitted radiation, also the Earth is a source of this perturbation and for high accuracy requirements, the simple model given by Equation (B.13) may be inadequate [27].

Other non-gravitational perturbations

There are many possible source of perturbations of non-gravitational nature, which may affect a satellite's orbit in different and complex ways. If the spacecraft has an electric charge, then the presence of the planet magnetic field generates forces due to the high relative velocity. Furthermore, heating by the Sun and the Earth, as well as internal heat sources, produce asymmetrical thermal distribution generating a thermal force responsible of drag-like effects. There are also satellite-dependent perturbations, for instance due to brief mass expulsions, producing a thrust force extremely difficult to model due to the uncertainties regarding the time and magnitude of the phenomenon. Eventually, empirical forces can be added to take into account perturbations of unknown origin or errors due to inaccurate forces modeling.

List of Figures

List of Tables

List of Symbols

Variable	Description	SI unit
α	Right Ascension	rad
$A(t)$	State matrix	-
Az	Azimuth	rad
$\boldsymbol{\beta}$	A priori consider parameter error	-
$\boldsymbol{b}$	B-plane vector	km
C	Combined covariance matrix in B-plane	km^2
$\boldsymbol{c}$	Consider parameter	-
C_{lm}, S_{lm}	Degree l, order m spherical harmonic coefficients	-
C_D	Drag coefficient	-
C_R	Reflectivity coefficient	-
δ	Declination	rad
$\delta\boldsymbol{x}$	Reference state deviation	km, km/s
$\delta\hat{\boldsymbol{x}}$	Estimated state deviation	km, km/s
$\delta\hat{\boldsymbol{x}}^-$	A priori state deviation	km, km/s
$\delta\boldsymbol{y}$	Reference measurement deviation	-
Δv_r	Relative radial velocity	km/s
$\boldsymbol{\epsilon}$	Observation error	-
El	Elevation	rad
ζ	Object albedo	-
F	Spacecraft nonlinear dynamics	-
$\boldsymbol{f}_{3B}$	Third-body acceleration vector	km/s^2
$\boldsymbol{f}_g$	Relativity correction acceleration vector	km/s^2

Variable	Description	SI unit
$\boldsymbol{f}_{Drag}$	Atmospheric drag acceleration vector	km/s^2
$\boldsymbol{f}_{SRP}$	Solar radiation pressure acceleration vector	km/s^2
$\boldsymbol{\eta}$	A priori state error	km, km/s
G	Nonlinear measurement function	-
G_u	Universal constant of gravitation	Nm^2/kg^2
$\tilde{H}$	Linearized measurement matrix	-
J_l	Degree l zonal harmonic	-
K	Kalman gain	-
μ	Standard gravitational paramter	Nm^2/kg
M	Apparent magnitude	-
m	Intrinsic magnitude	-
ν	Eclipse factor	-
n	State dimension	-
P	Covariance matrix	km^2, km^2/s^2
P^-	A priori covariance matrix	km^2, km^2/s^2
P_{lm}	Degree l, order m Legendre function	-
P_c	Collision probability	-
ρ	Range	km
$\dot{\rho}$	Range rate	km/s
Q	Process noise	-
R	Measurement error matrix	-
$R_{n,2D}$	Rotation matrix from interial to B-plane	-
$\boldsymbol{r}$	Position vector	km
r_A	Hard-body radius	m
σ_r	Positional standard deviation	km
σ_v	Velocity standard deviation	km/s
$\boldsymbol{s}$	Relative state vector	km, km/s
T_p	Primary orbit period	s
t	Time	s

Variable	Description	SI unit
t_c	Encounter duration	s
$\boldsymbol{u}_{\xi,\eta,\zeta}$	Components of B-plane coordinate system	km
U	Gravitational potential	Nm
Φ	State Transition Matrix	-
ϕ	Flow	-
φ	Phase angle	rad
$\boldsymbol{v}$	Velocity vector	km/s
W	Measurement weight matrix	-
$W^{(m)}$	Sigma point mean weight	-
$W^{(c)}$	Sigma point covariance weight	-
χ	Sigma point	km, km/s
$\boldsymbol{X}$	State vector	km, km/s
$\boldsymbol{Y}$	Measurement vector	-
Ω	Right ascension of the ascending node	rad
$\boldsymbol{z}$	Augmented state	-

List of Acronyms

CAM	Collision Avoidance Manoeuvre
CCA	Consider Covariance Analysis
ECI	Earth Centered Inertial
FoV	Field of View
IOD	Initial Orbit Determination
LEO	Low Earth Orbit
LSQ	Least SQuares
ODE	Ordinary Differential Equation
RAAN	Right Ascension of the Ascending Node
RADEC	Right Ascension and DEClination
RCS	Radar Cross Section
ROD	Refined Orbit Determination
RSO	Resident Space Objects
SNR	Signal to Noise Ratio
SOPAC	Space Object PAss Calculator
SRP	Solar Radiation Pressure
SSO	Sun-Synchronous Orbit
STM	State Transition Matrix
TCA	Time of Closest Approach
TLE	Two-Line Element
UKF	Uscented Kalman Filter
UT	Unscented Transform

Acknowledgements

I would like to thank to my advisor Prof. Di Lizia for his unwavering support and kindness throughout these months. Your assistance in resolving any issue that arose was invaluable, and I am grateful for the confidence you placed in me with the opportunity to work on this project. Thanks also to Prof. Massari for his crucial contribution. Your insights and ideas were an excellent source of inspiration and helped me shape a constantly evolving research. Thanks to both for stimulating my interest in the subject, as well as that curiosity without which this thesis would not have been possible.

A special thanks also to Michele Maestrini and Luca Facchini for your endless patience and willingness to help. Your precious support and the knowledge you shared were essential to achieve these results.

Last but not least, I would like to express my gratitude to my family for their constant support and encouragement throughout my studies. This important milestone is also thanks to you.